CHEMICAL REVIEWS

pubs.acs.org/CR

Review

Colloidal Quantum Dots as Platforms for Quantum Information Science

Cherie R. Kagan,* Lee C. Bassett,* Christopher B. Murray,* and Sarah M. Thompson

Cite This: *Chem. Rev.* 2021, 121, 3186–3233

Read Online

ABSTRACT: Colloidal quantum dots (QDs) are nanoscale semiconductor crystals with surface ligands that enable their dispersion in solvents. Quantum confinement effects facilitate wave function engineering to sculpt the spatial distribution of charge and spin states and thus the energy and dynamics of QD optical transitions. Colloidal QDs can be integrated in devices using solution-based assembly methods to position single QDs and to create ordered QD arrays. Here, we describe the synthesis, assembly, and photophysical properties of colloidal QDs that have captured scientific imagination and have been harnessed in optical applications. We focus especially on the current understanding of their quantum coherent effects and opportunities to exploit QDs as platforms for quantum information science. Freedom in QD design to isolate and control the quantum mechanical properties of charge, spin, and light presents various approaches to create systems with robust, addressable quantum states. We consider the attributes of QDs for optically addressable qubits in emerging quantum computation, sensing, simulation, and communication technologies, e.g., as robust sources of indistinguishable, single photons that can be integrated into photonic structures to amplify, direct, and tune their emission or as hosts for isolated, coherent spin states that can be coupled to light or to other spins in QD arrays.

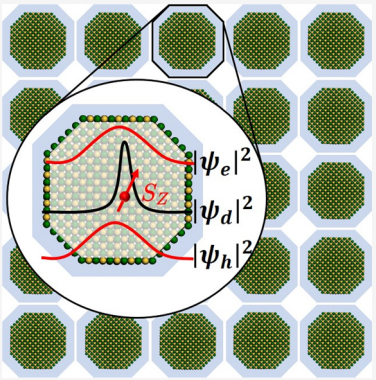

CONTENTS

Special Issue: Quantum Materials

Received: August 5, 2020
Published: December 29, 2020

https://dx.doi.org/10.1021/acs.chemrev.0c00831
Chem. Rev. 2021, 121, 3186–3233

1. INTRODUCTION

Colloidal quantum dots (QDs) are fragments of bulk semiconductor crystals with typical diameters of <100 nm. Shells of ions or organic or inorganic ligands serve to electrostatically or sterically stabilize their dispersion in solvents (Figure 1a).[1]

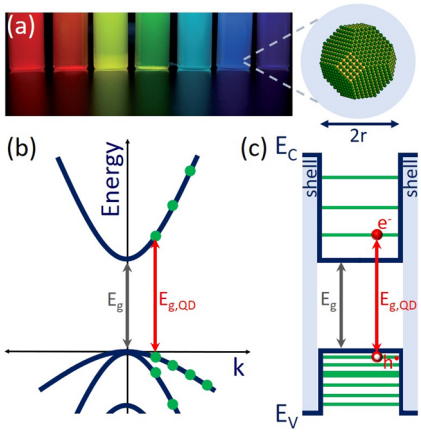

Figure 1. (a) Photograph of the photoluminescence from dispersions of colloidal CdSe QDs,[2] ranging in size from (right to left) ~2 to 6 nm, and a schematic of a colloidal QD, composed of a crystalline semiconductor core of radius r and an organic or inorganic shell (light blue). (b) Schematic of the E vs k band structure of a bulk semiconductor (dark blue lines) with a direct band gap of energy E_g and the allowed states of a colloidal QD (green circles) with its lowest-energy transition, $E_{g,QD}$. (c) Schematic of the real space, energy diagram, corresponding to the E vs k diagram in part b, of a QD of radius r, as depicted in part a, where $E_{C,V}$ show the spatial variation of the conduction and valence bands across the core and shell, in this case forming a type-I band alignment. The photograph in part a is reproduced with permission from ref 2. Copyright 2011 Elsevier.

Advances in synthesis enable the preparation of colloidal QDs tailored in size within atomic roughness, in shape, and in internal structure for a wide range of elemental, binary, ternary, and quaternary compositions. Examples include spheres, cubes, and rods of group IV allotropes of carbon and Si; III–V In-pnictides; II–VI and IV–VI Zn-, Cd-, Hg-, Pb-, and Sn-chalcogenides; I–III–VI_2 Cu_xIn_{1-x}-chalcogenides; I_2–VI Cu- and Ag-chalcogenides; I–VII Cu-halides; and metal-halide perovskites (ABX_3; X = Cl, Br, I) typically composed of Pb or Sn B-site cations and Cs or organoammonium A-site cations. These QDs generally are smaller in size than or comparable to the bulk semiconductor electron, hole, and/or exciton Bohr radii. Therefore, carriers and excitons experience strong to intermediate to weak degrees of quantum confinement. Quantum confinement effects underlie their size-dependent electronic properties, which evolve from molecular to bulk-like as the QD size increases, and give rise to their prized, size-tunable optical properties. As an example, Figure 1a shows the color of luminescence varying from blue (right) to red (left) for CdSe QDs ranging from ~2 to 6 nm in diameter.[2] The continuous tailorability and narrow dispersion in QD sample size as well as the small Franck–Condon factors in inorganic semiconductors compared to organic luminophores[3] allow precise engineering of their color and high color purity in their optical absorption and luminescence. These characteristics are being exploited in conventional applications, commercially as optical materials that serve as luminescent probes for biology[4] and to downshift blue light from light-emitting diode (LED) backlights to produce high-definition, wide color gamut displays,[5,6] and in research as absorbers and emitters in light-sensitive and light-emissive optoelectronic devices.[7]

Here, we briefly introduce the objectives of quantum information science and several key properties that are desirable in material platforms. In this context, we then review the role of quantum confinement effects in defining the electronic structure of QDs and then describe research in the colloidal QD community over the last 30 years on synthetic methods, structural characterization, and optical spectroscopy of their photophysical properties. This research sets the stage for a more recent history and a forward look at the opportunities to explore QDs as quantum optical materials. We begin with the quantum optical properties of their excitonic transitions and in subsequent sections discuss the state of the art in how quantum coherent charge and spin states can be realized through synthetic control of QD heterostructures and the introduction of intentional defects. We focus on the unique characteristics of colloidal QDs, in comparison to their bulk semiconductor analogues, that make them exciting candidate systems for quantum optical materials. With diverse functions "packaged" within individual QDs, we consider how the colloidal character of QDs can be exploited to assemble single QDs and arrays of QDs, which promises to allow their integration in optical cavities and in architectures for quantum information processing.

This review is written to introduce both the colloidal QD community to the desired materials properties for quantum information science and technology and the quantum information science community to the physics and chemistry of colloidal QDs that make them an excellent materials class and platform for study. To serve as a resource for and to bring both communities together, the review is comprehensive in presenting the fundamental physics and chemistry and well-studied and distinguishing examples from both fields and in laying out our present day understanding of the quantum optical properties of and future opportunities for colloidal QDs to address the needs of quantum information science.

2. MATERIALS FOR QUANTUM INFORMATION PROCESSING

We begin with an introduction of the different quantum information technologies to set the stage for the quantum optical properties that are required and may be realized in colloidal QDs. Quantum information processing relies on the isolation and manipulation of fundamental quantum-mechanical properties—such as charge, spin, and light—in such a way that the

https://dx.doi.org/10.1021/acs.chemrev.0c00831
Chem. Rev. 2021, 121, 3186–3233

system's dynamics encode and process information. Information can be encoded, for example, in the spatial orbital distribution of an electron, the projection of spin angular momentum for a nucleus, or the polarization axis of a photon. In analogy with classical digital computing, the configuration of these discrete quantum states maps to logical bits. It is often convenient to isolate a quantum system with two states—a qubit—as the fundamental building block. As shown in Figure 2, quantum

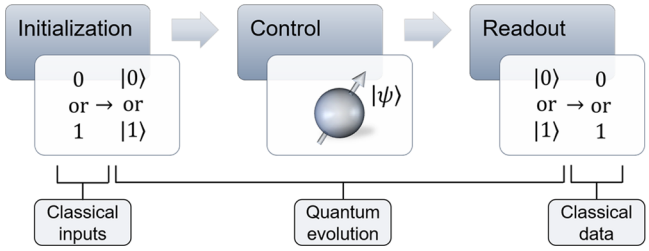

Figure 2. Essential elements of quantum information processing. Classical digital inputs are converted into well-defined quantum states, which subsequently evolve quantum mechanically through interactions with each other and with classical control fields. Measurements of the resulting quantum states yield classical output data.

information processing consists of *initialization* to set the relevant quantum states, *control* over interactions such that the system's quantum dynamics achieve the desired operation on those states, and *readout* to measure the result.[8] In contrast to classical information processing, however, quantum systems can exploit the properties of superposition, entanglement, and quantum interference in their operation. Among a host of rapidly emerging technologies, the four major areas of quantum information science are *quantum computing*, where the goal is to execute an algorithm on digitally encoded data; *quantum communication*, with an aim of securely transmitting quantum-encoded data over long distances; *quantum simulation*, where well-controlled quantum systems are used to simulate other physical phenomena; and *quantum sensing*, where quantum systems are used to detect or transduce classical or quantum signals with enhanced performance.

These different quantum-information technologies have varied, and often contradictory, requirements. Quantum computing requires the assembly of a large number of individually addressable qubits that can be entangled with each other at will and protected from unwanted interactions with the environment. Quantum sensing demands a well-controlled interaction between a quantum system and the signal of interest along with a robust detection method. Quantum communication prototypically involves the transfer of quantum information—in the form of a superposition and entangled states—between different degrees of freedom, such as spins and photons. The need to match system properties with application requirements holds even when considering different device architectures or protocols within a single application domain. A temperature sensor to be used in living cells, for example, will have markedly different requirements than a gravitational accelerometer to be used in space.

Quantum hardware takes many forms, including trapped atoms and ions,[9] superconducting circuits,[10] silicon electronics,[11] integrated photonics,[12] and quantum defects.[13] The modality used to address and control each quantum hardware platform, typically through classical electronic or optical signals, further informs the system design and relevant figures of merit. Nonetheless, we can outline general considerations. For optically addressable qubits,[14−16] the following characteristics bear particular importance:

- *Single-photon emission*: Single-photon emitters possess discrete electronic ground and excited states, connected by radiative transitions that can be triggered optically or electronically.[17] The discrete nature of the quantum states means that—ideally—one and only one photon is emitted when the excited state decays. In principle, such a two-level system can constitute a qubit; however, the coherence lifetime will be intrinsically limited by the radiative decay time. For this reason, qubits to be used for storage or manipulation of quantum information are generally encoded in long-lived ground or metastable states.[14] Nonetheless, single-photon emitters are essential components in many quantum technologies, especially for quantum communication and for quantum-information processing using linear photonic circuits. The basic properties of single-photon sources include brightness and Fock-state purity.[18] Brightness refers to the probability that the source produces a photon at the desired time, while purity measures the likelihood that a detected photon originated from the source rather than background effects. These are desired features of all quantum-photonic technologies; however, most applications have stricter demands, as discussed below.
- *Optical coherence*: Indistinguishable photons are required for all-photonic quantum devices that rely on interference and entanglement between multiple photons. Key examples include linear quantum photonic circuits[12] designed to implement quantum computations,[19,20] quantum simulations,[21] or Boson sampling.[22] These applications require large numbers of indistinguishable photons to be prepared on-demand with high brightness and purity. Indistinguishable photons are also necessary for entanglement-by-measurement of distant spin qubits coupled by photonic channels.[23] For photons to be indistinguishable, they must be emitted in identical spectral, temporal, and spatial modes. These characteristics are challenging to achieve in solid-state systems due to coupling to phonons and uncontrolled electronic fluctuations in the material.
- *Oscillator strength*: The electric dipole matrix elements for optical transitions determine the photon emission lifetime and the emitter's coupling strength to a nanophotonic device. Static and induced electric dipoles also determine the sensitivity of the optical transition frequency to electric field noise. Generally, this leads to a trade-off where systems with large oscillator strength (e.g., QDs and defect-bound excitons) are bright and couple efficiently to photonic devices but have low optical coherence. In contrast, other systems (isolated transition-metal and rare-earth dopants, especially) have lower emission rates but more stable transitions.
- *Spin coherence*: Electronic spins are exceptional and versatile qubits, especially for applications that require local processing, long-lived quantum memories, and an optical interface.[14] In contrast to charge degrees of freedom, spins are relatively insensitive to environmental noise. At the same time, they interact strongly enough with specific local fields—and with other nearby spins—to facilitate the generation and control of entangled states.

https://dx.doi.org/10.1021/acs.chemrev.0c00831
Chem. Rev. 2021, 121, 3186−3233

The coherence lifetime of an electronic spin in the solid state is determined by a combination of factors including spin−orbit coupling or spin−lattice interactions, which couple the spin to phonons and electric field noise; hyperfine interactions with proximal nuclear spins; and magnetic noise typically from unpaired electronic spins in the material or trapped at interfaces. If the spin state is metastable, then its coherence is also limited by the state's lifetime.

- *Spin−photon interfaces*: For applications requiring coherent transfer of quantum information between spin states and photon states (e.g., entanglement-based quantum communication, quantum repeaters, and distributed quantum computers), all of the above properties are required, in addition to a set of spin-dependent optical transitions that can generate spin−photon entanglement. Such spin-dependent transitions typically result from intrinsic spin−orbit coupling between different orbital and spin levels that comprise the defects' ground and optically excited states. Here again, we note a trade-off, where spin−orbit coupling is required to realize an interface between spins and photons, yet its presence is often detrimental to quantum coherence.
- *Scalable fabrication:* All quantum technologies require building blocks that can be synthesized with the scalability and uniformity to enable the fabrication of increasingly sophisticated devices. Single-photon sources need to be incorporated with photonic nanostructures to enhance and direct their emission.[24] The resolution and performance of quantum sensors depend on their placement close to surfaces within sensing devices that also facilitate quantum control.[25] Coherent magnetic interactions between proximal spins are only practical for generating entanglement over separations of a few nanometers,[26] so arrays of coupled spin qubits need to be assembled with nearly atomic precision.

As we will see throughout this review, colloidal QDs can address all of these requirements. Other QD platforms, notably including III−V epitaxially self-assembled QDs[18,27,28] and lithographic QDs created from two-dimensional quantum wells,[29−31] are already widely utilized for building quantum devices. Colloidal QDs share many desirable characteristics with these complementary QD morphologies while offering greater flexibility in the choice of materials and methods for device integration. Indeed, colloidal QDs are already preeminent platforms for engineering strong, tunable optical responses for classical technologies. The time is right to develop their quantum functionality for new generations of applications in quantum information science.

3. COLLOIDAL QUANTUM DOTS

3.1. Electronic Structure of Bulk Semiconductors and QDs

Bulk semiconductors are characterized by their energy diagrams composed of an energy gap (Eg), ranging from 0.1 eV to as large as 6 eV, separating conduction and valence bands. The energy bands result as the degeneracy of atomic orbitals from $\sim 10^{22}$ atoms/cm^3 is broken, but are closely spaced, forming a continuum. The electronic band structure describes the dispersion relationship between the energy (E) of allowed conduction and valence band states and the crystal momentum (k), i.e., the direction of carrier motion in the crystal (Figure 1b, blue curves). The band structure of bulk semiconductors is continuous, given the large number of atoms and therefore closely spaced energy levels; is practically parabolic, with curvature near the band extrema that depends inversely on the carrier effective mass (m^*) following the effective mass approximation; and varies with the composition and crystal structure of the semiconductor, defining the band energies, widths, and effective mass for different k. The density of surface states is small in comparison to the density of band states due to the small ratio of atoms at the surface relative to those in the bulk.

As the dimensions of semiconductors are reduced to <100 nm, as found in quantum wells and wires and in QDs, the topic of this review, the electronic structure is altered from that of the parent bulk material by quantum confinement effects.[32] For strongly confined QDs, the QD radius is small compared to the electron and hole Bohr radii $a_{e,h} = \frac{\hbar^2 \varepsilon_\infty}{m^*_{e,h} e^2}$ and the exciton Bohr radius $a_{ex} = \frac{\hbar^2 \varepsilon_\infty}{e^2}\left(\frac{1}{m^*_e} + \frac{1}{m^*_h}\right)$, where ε_∞ is the static dielectric constant of the semiconductor, $\hbar$ is the reduced Planck's constant, and e is the unit charge. The electrons and holes can be treated independently by the particle-in-a-box model, where the box is composed of the parent semiconductor and treated by the effective mass approximation.[33] The bulk semiconductor composition and crystal structure determine ε_∞, m^*_e, and m^*_h, and the size and shape of the QD define the geometry of the box. Since the size of the box is finite and equal to the product of the number of unit cells N and their lattice constant a, the allowed values of k are restricted and equal to $\frac{m\pi}{Na}$, where m is an integer (Figure 1b, green circles). An equivalent solution is found using the Hückel molecular orbital theory.[34] The discrete eigenvalues for QDs lie on the bulk $E(k)$.

For spherical QDs of radius $r = \frac{Na}{2}$, these states are atomic-like and are labeled by the radial and orbital angular quantum numbers n = 1, 2, 3, ... and L = 0, 1, 2, ..., written as S, P, D, respectively, to give n_hL_h and n_eL_e for hole and electron states in the valence and conduction bands. The lowest-energy states are $1S_h$ and $1S_e$, where S refers to the symmetry of the envelope wave functions and h and e index the hole and electron.[34] For bands with substructure, commonly semiconductor valence bands originating from atomic p orbitals, the hole index can further be replaced by the total angular momentum quantum number $F = J + L$, where J is the Bloch-function angular momentum describing the substructure of 4-fold degenerate light and heavy hole bands with $j = {}^3/_2$ and the 2-fold degenerate spin−orbit split-off band with $j = {}^1/_2$, to give nL_F (e.g., the lowest-energy hole state is $1S_{3/2}$).[35−37] To be general to different semiconductor QDs, in this review, we describe the lowest-energy conduction and highest-energy valence states by $1S_e$ and $1S_h$.

The energies and separation between the lowest-conduction and highest-valence band states increase with decreasing QD size, giving rise to the size-dependent band gap $E_{g,QD}(r) = E_{g,bulk} + \frac{\hbar^2\pi^2}{2r^2}\left[\frac{1}{m^*_e} + \frac{1}{m^*_h}\right]$, where the second term is the confinement energy.[38] In larger QDs, the Coulomb interaction between electrons and holes becomes significant and a correction of $-\frac{1.8e^2}{\varepsilon_\infty r}$ is added, which acts to reduce the effective QD band gap. The band gap tunability achievable with QD size, from the smallest ~1 nm QDs to QDs ~2−3× larger than the exciton Bohr radius for a given semiconductor composition, depends on m^*_e and m^*_h, and is easily visualized

https://dx.doi.org/10.1021/acs.chemrev.0c00831
Chem. Rev. 2021, 121, 3186−3233

by the curvature of the band structure E vs k.[39] The energies of these allowed k-states are represented in the QD energy diagram and capture the complexity of the underlying semiconductor band structure, for example, the p-like character of the valence band substructure in the example depicted in Figure 1c. Interestingly, recently explored metal-halide perovskite QDs have s-like valence bands and p-like conduction bands, so that the complex, sub-band structure is found not in the valence band but in the conduction band.[40]

QDs have a large surface-to-volume ratio, and thus, the chemistry of the surface can influence the electronic structure of the QD. The surface of the QD presents different crystal facets and dangling bonds that can create non-stoichiometry and defect complexes, which in turn introduce shallow and deep electronic trap states within the band gap.[7,40] Shallow states can serve as electronic dopants, altering the carrier concentration. Deep states are efficient non-radiative recombination−generation (R−G) centers and notoriously limit the quantum yield (QY) of luminescence. The bright luminescence seen in QDs came first serendipitously and then from years of research culminating in the rational design of "shells" that surround the QD core and passivate surface electronic states.[41,42] These shells are composed of organic ligands that strongly bind QD surface atoms and, in more recent years, typically larger band gap semiconductors that create type-I heterojunctions (Figure 1c).[43−45] Ligands at the QD surface can also create dipoles that shift the absolute energies of the conduction and valence band states, which are particularly important in the design of some QD heterojunction devices.[46]

3.2. QD Synthesis, Purification, and Exchange

The past 30 years have seen dramatic improvements in the synthesis and fabrication of QDs. Three main classes of QDs are found in the current literature and are actively pursued by largely separate communities for a range of applications, including quantum information science. The demands of quantum information science applications will push the miniaturization, precision, chemical and structural purity, and spatial localization of QDs to their chemical and physical limits.

Lithographic QDs: Top-down lithographic processing has been used to create structures where an externally addressable electrostatic gate provides a tunable confining potential for carriers.[31,47,48] Lithographic, or "gated", QDs offer a high degree of control and a ready path to integration with existing nanofabricated electronic systems. Lithographic QDs were among the first platforms explored as architectures for scalable quantum computing,[29] and they remain the focus of active research.[30] However, the patterning of multiple electrodes needed to create the electrostatic confining potential limits the size of the QD to several times the most aggressive minimum lithographic feature size. Therefore, these structures exhibit their most exciting properties at temperatures well below 1 K. The fabrication processes that offer the highest-resolution structures are often serial, direct-write methods such as e-beam lithography, and thus limit the number of QDs that can be prepared.

Strained-Layer Epitaxial Quantum Dots (SLE-QDs): Top-down molecular beam epitaxy (MBE) or metal−organic chemical vapor deposition (MOCVD) can be combined with bottom-up, strained-layer epitaxy to yield QDs. In these SLE-QDs, heteroepitaxy of repeated layers of wide and narrow band gap semiconductors (e.g., InAs/GaAs or PbTe/PbSe) is used to create compressive strain in the lattice of the narrow band gap material, inducing the formation of islands or hillocks rather than a continuous thin film.[49] These islands can, in turn, be covered by an epitaxial layer of the wider band gap semiconductor, resulting in a three-dimensionally confined inclusion of the narrow band gap material. Although the initially narrow gap islands are largely randomly positioned laterally, once the growth transitions from 2D to 3D, the area immediately surrounding each island is depleted of new material as diffusion and addition to existing islands is favored.[50,51] Under optimized conditions, the statistical competition for material results in the growth of an ensemble of islands having similar dimensions and interisland spacing. As multiple layers of these SLE-QDs are grown by successively alternating the deposition of materials of differing lattice constant, the strain fields of the newly buried dots induce strain in the subsequent layers. This strain enables a self-assembled or self-organized growth mode to develop in which the positions of the embedded and added QDs become correlated both vertically and laterally.[52] These strain fields can be engineered by exploiting lithography.[53,54] These SLE-QDs can be grown with dimensions far smaller than those of lithographically fabricated QDs, and they exhibit complex quantum behavior even at room temperature. As the SLE-QDs are embedded in a semiconducting matrix, they offer a straightforward path to optoelectronic device integration. The self-assembled growth process is essentially a planar process repeated multiple times, but it provides the advantage of parallel QD production in each layer. However, SLE-QD systems are constrained by the inherent polydispersity in QD size and QD position afforded by the thermodynamics and kinetics of the growth. Further purification or narrowing of the QD size distribution is not practical.

Colloidal QDs: The focus of this review is colloidal QDs, which are also commonly referred to as semiconductor nanocrystals (NCs). These materials are the purest expression of the bottom-up approach in which the synthesis of QDs can be coupled with advanced separation or purification procedures. QDs are grown from molecular precursors and can contain anywhere from 10^2 atoms to 10^5 atoms to more than 10^8 atoms, as the QD diameter increases from ∼1 to ∼10 to ∼100 nm. The ability to produce discrete, dispersible nanostructures blurs the lines between molecular synthesis and classic colloidal chemistry. Treating the surface of the QDs with ligands provides physical and chemical stability to the colloidal QDs and modifies the electronic structure of the semiconductor surface. These colloidal routes offer the ability to process and purify the resulting QDs to meet ever more demanding optical and electronic specifications. Although the synthesis of QDs has been studied for over three decades, recent advances hold the potential to deliver the structural and chemical uniformity, spectral tunability and purity, reproducibility, and stability needed to enable a new generation of quantum-enabled technologies. The library of QD materials now accessible has expanded to embrace materials from all major semiconductor classes, IV, III−V, II−VI, IV−VI, I−III−VI_2 I_2−VI, I−VII, and metal-halide perovskites, including many formulations that are earth-abundant and/or nontoxic for greater commercial acceptance. Here, we describe the synthetic methods used to prepare colloidal QDs.

3.2.1. Aerosol and Plasma Synthesis. One strategy for QD production builds off the tradition of aerosol chemistry, in which high-temperature evaporation of material or gas-phase cracking of molecular precursors is followed by nucleation and growth of QDs. The QDs are entrained in a gas flow and can

https://dx.doi.org/10.1021/acs.chemrev.0c00831
Chem. Rev. 2021, 121, 3186−3233

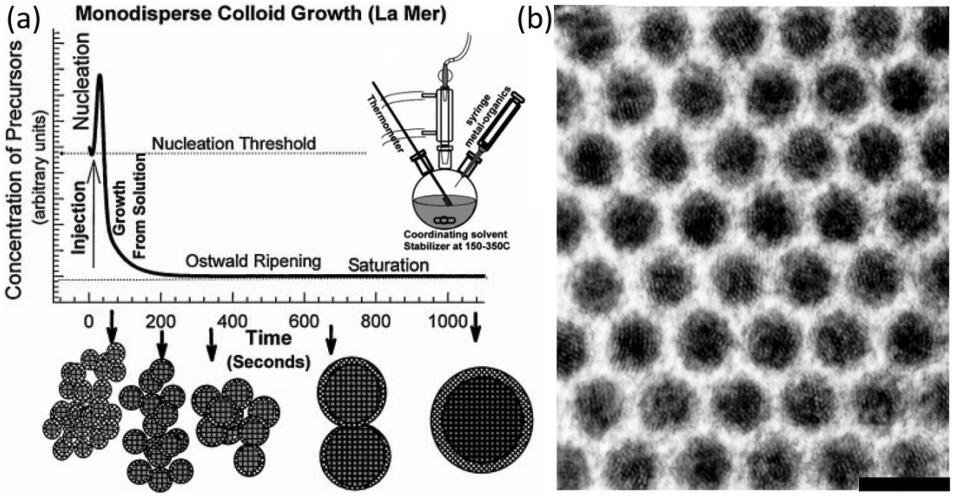

Figure 3. (a) Schematic of La Mer and Dinegar's model of monodisperse colloid synthesis, described by the concentration of precursors over time and the regimes of nucleation, growth, and ripening, and its representation to control the size and number of colloidal QDs. (inset) Reaction vessel for the growth of colloidal QDs.[65] (b) TEM image of an array of 4.8 nm CdSe QDs.[65]

either be collected on a surface or the gas flow can be bubbled through a solvent with a colloidal stabilizer to disperse the QDs. Although the number density of QDs produced in the gas phase is low, the process is continuous, and thus, appreciable, multigram scale quantities of QDs can be prepared over time.[55] An attractive attribute of the aerosol or gas-phase syntheses is that the QDs can be passed through a furnace to anneal out deleterious structural defects, to introduce dopants, or to grow a passivation layer (e.g., SiO_2 on Si). These routes allow the production of more refractory materials than lower-temperature chemical routes. Among the most successful variants of this approach are the "dusty-plasma"-based syntheses.[56,57]

3.2.2. Aqueous Arrested Precipitation. The wet-chemical synthesis of QDs builds on traditions of aqueous colloid growth reaching back to Faraday and LaMer. In the early 1980s, investigations of aqueous arrested precipitation reactions, in which sparingly soluble metal chalcogenide salts were added to water in the presence of surfactants, yielded stable colloids with optical absorption spectra that shifted to the red as the size of the particles grew larger. This observation of size-dependent optical properties launched interest in colloidal semiconductor QDs.[58−60] The introduction of micellar solutions or inverse micelle systems to spatially confine the nucleation and growth process improved particle size control,[61] but these low-temperature methods still suffered from a high degree of internal and surface disorder and exhibited spectrally broad emission and low-photoluminescence (PL) QY. Aqueous arrested precipitation techniques are still broadly practiced due to their simplicity, scalability to kg or even ton scale,[62] and applicability to a wide range of semiconducting materials.

The attachment of amphiphilic organic ligands (capping groups) to the QD surfaces post-synthesis or by injection in the later stages of synthesis to terminate QD growth enabled hybrid aqueous−organic routes. The organic ligands improved the colloidal and chemical stability and enhanced the optical properties (spectral line width and PL QY) of the QDs by passivating undercoordinated surface sites which act as non-radiative recombination centers. The phase transfer of the organically capped, ligand-stabilized colloidal QDs to higher-boiling point (>150 °C), coordinating solvents (e.g., alkylamines or alkylphosphines and alkylphosphine oxides) allowed annealing to further reduce internal and surface defects, and thus improvements in the optical properties of the QDs.[63] These improvements motivated a full non-aqueous, high-temperature (solvothermal) colloidal synthesis of QDs.

3.2.3. Solvothermal Synthesis. In the early 1990s, high-temperature, non-aqueous "solvothermal" synthetic routes were introduced to produce QDs.[64] LaMer and Dinegar's model of colloid growth teaches that monodisperse colloids can be prepared via a temporally discrete nucleation event, by creating a supersaturation of monomers that is relieved at high temperature upon the formation of nuclei (Figure 3a).[65] The term "monomer" in this context does not refer to a precise chemical entity but is used to represent the smallest hypothetical semiconductor subunit consisting of one cation and one anion. The monomer species result from the thermally induced chemical reaction of the semiconductor precursors.[66] The QDs grow like a living "inorganic polymer" from semiconductor monomer species in solution. After nucleation, the monomer concentration drops below the threshold for the formation of new nuclei but remains above the equilibrium solubility, allowing further growth on the initially formed nuclei.[67] If the nucleation stage is brief and the subsequent growth consumes more monomer than the initial nucleation, the colloid can enter a "size-focusing regime", generating a monodisperse colloidal dispersion.[68,69] The organic solvents employed in solvothermal syntheses are comprised of a mixture of surface-active (amphiphilic) species, capable of moderately and reversibly coordinating the surface of the QDs during growth, and a high-boiling-point weakly or noncoordinating solvent. The balance of coordinating strength, steric bulk, and lability of the stabilizing ligands is used to allow nucleation and slow growth of QDs at high temperature (100−350 °C) while suppressing their aggregation.

Separate from nucleation and growth, many colloidal systems also display a distinct, third stage called Ostwald ripening in which the average colloid size increases as the particle concentration decreases over time.[70] If the monomer has an appreciable concentration at the growth temperature, an equilibrium is established with the dispersed QDs between dynamic processes of deposition and dissolution/etching.

https://dx.doi.org/10.1021/acs.chemrev.0c00831
Chem. Rev. 2021, 121, 3186−3233

Ostwald ripening is driven by the high surface area, less energetically stable small particles in the ensemble, in comparison to their larger siblings. The small particles experience net etching and ultimately disappear, while the larger particles experience net deposition, resulting in growth over time. The equilibria between the monomer species and the QDs and the diffusion rates of the monomer in solution are strongly temperature-dependent. Thus, time and temperature can be adjusted to engineer the particle size and size distribution.

The first widely adopted implementation of solvothermal QD synthesis is often referred to as the "hot injection method". This is exemplified by the synthesis of II−VI QDs in which a group II metal alkyl precursor (e.g., $Cd(CH_3)_2$ or $Zn(CH_2CH_3)_2$) and a group VI precursor (e.g., bis-trimethylsilyl chalcogenides or trialkylphosphine chalcogenides) are reacted at high temperature.[1] These precursors were initially selected from systems used in MOCVD, as discussed in SLE-QD synthesis. The group II and VI precursor solutions are mixed at room temperature in a high-boiling-point, weakly coordinating solvent, in this case tri-*n*-octylphosphine (TOP), and rapidly injected into a reaction vessel containing a high-boiling-point, strongly coordinating solvent, in this case trioctylphosphine oxide (TOPO), that is heated to 200−350 °C under an inert atmosphere (Figure 3a, inset).[64,65] Although the group II and group VI precursors react slowly, if at all, at room temperature in viscous, coordinating trialkylphosphine, the injection into the hot vessel causes a temperate jump in the precursor solution that induces their rapid decomposition and the creation of monomer species *in situ*. The monomer concentration rapidly reaches supersaturation and is relieved by the nucleation process. The injection causes the vessel temperature to drop, slowing the decomposition of precursors and the formation of monomer. In less than a minute, the nucleation phase ends and the colloid enters the growth stage. After approximately 10−30 min, Ostwald ripening becomes dominant. This approach was first demonstrated to generate a series of CdE (E = S, Se, Te) QDs from a single batch reaction, isolating species with diameters ranging from 1.5 to 12 nm over a period of a few hours while maintaining size distributions of <10% stdv.[64] Figure 3b shows a TEM image of an example of CdSe QDs.[65] The size distribution is further narrowed to <5% stdv via purification and separation processes described in section 3.2.4. Alternately, the full contents of the reaction, at the scale of 250 mL in a 500 mL flask, could be isolated at one time to yield up to 3.0 g of material of a desired size.[71]

A general weakness of hot-injection methods is the complex dependence of the initial nuclei distribution on variables such as the injection rate, mixing rates, and small temperature fluctuations, which is a liability when attempting to scale the production of specific sizes reproducibly. Early organometallic methods were undesirable due to the reactivity (pyrophoric nature) and extreme toxicity of the metal alkyl precursors. This concern was addressed by Peng et al. with the introduction of a less toxic, nonvolatile, group II CdO precursor that allowed the hot-injection synthesis of high-quality QDs.[72,73] As the inherent toxicity of Cd cannot be entirely eliminated in the CdE (E = S, Se, Te) family, the design of "greener" QD variants based on Zn−VI, III−V, I_2−VI, and I−III−VI_2 has become an active area of research.[74,75]

Replacing the majority of the coordinating TOP−TOPO in the II−VI QD synthesis with a noncoordinating or at least very weakly coordinating solvent such as octadecene (ODE)[76,77] or mineral oil/paraffins[78] to form a mixed solvent, with a minor concentration of a coordinating species, further lowers the cost and reduces the toxicity of the waste from solvothermal reactions.[74] Hot injection continues to be employed at the laboratory scale, in large part due to the fact that the method can produce many types of semiconductor QDs, for example, I_2−VI Ag_2S and Ag_2Se,[79,80] II−VI CdS, CdSe, CdTe, ZnS, ZnSe, and ZnTe;[81−83] IV−VI PbS, PbSe, and PbTe;[84−87] and III−V InP and InAs.[88,89] Recently, the synthesis of colloidal perovskite QDs has become an area of intense study.[68−74] Kovalenko et al. showed that the injection of a solution of cesium oleate into a hot PbX_2 (X = Cl, Br, I) solution could produce the full set of $CsPbX_3$ (X = Cl, Br, I) perovskite QDs in an ODE solution.[90] Pb-free Cs_2SnI_6 QDs have also been reported.[91]

The rise in interest in applications in the early 2000s motivated the identification of scalable routes of QD production[92] that eliminated the precursor injection. The "heat-up" method was introduced. The route relies on a ramp up in temperature and favorable decomposition kinetics for the precursors to generate monomer *in situ*, and similarly achieve the temporally discrete nucleation followed by continued growth emphasized by the LaMer model[67] for the generation of monodisperse colloids.[93,94] van Embden et al. and Hyeon et al. have written extensive reviews on heat-up synthesis procedures.[95,96] In the heat-up approach, all reactants are mixed in the reaction vessel, and the reaction is heated at a controlled rate to induce nucleation and growth. As the reaction vessel's temperature is raised, the precursors decompose to form monomers, which can accumulate and briefly exceed supersaturation to trigger nucleation. The kinetics of the decomposition reaction and the rate of growth on the nuclei formed must be carefully balanced, making the selection of the precursors, ligands, and reaction conditions critical. Nucleation must be rapid enough to produce a large number of nuclei within a relatively short time window, and growth must be slow enough to allow size focusing without the monomer concentration ever returning to the degree of supersaturation needed to induce secondary nucleation. Over time, many syntheses first implemented with hot injection have been modified to allow the more scalable "heat-up" approach,[97,98] of many metal chalcogenide and pnictide QD compositions.[95,99−101]

To better control the variables of precursor addition, mixing, temperature, and temperature distribution that impact QD growth in both injection and noninjection methods, higher degrees of automation have been explored, including the translation of the syntheses for continuous flow production. These flow syntheses leverage advances in microfluidics, in which the reactants are continuously fed, undergo transformations in the flow, and yield products upon exit. The primary appeal is the precise control of reaction parameters (e.g., temperature profile and residence time), in comparison to batch operations, and the ability for online, analytical probes to monitor and provide feedback to reaction controllers to optimize the synthesis conditions.[102] Microfluidic systems have proven to be powerful platforms for the investigation of QD growth mechanisms and kinetics[103] and, with integrated heaters and fluid flow controls, have been shown to benefit QD "quality control".[104−106] Growth of both the QD cores and inorganic overlayers or shells (see section 4.2) can be achieved in flow. A challenge to implementing microfluidic reactions is the potential for nonuniform flow velocity, due to viscous drag at the channel walls, which leads to a dispersion in residence times and in thermal history. This challenge has largely been overcome by operation in a supercritical solvent.[107]

https://dx.doi.org/10.1021/acs.chemrev.0c00831
Chem. Rev. 2021, 121, 3186−3233

3.2.4. Purification and Separation. Synthetic methods that yield the highest-quality, most uniform samples are prized, as discussed in section 3.2. However, even procedures optimized to yield samples with narrow dispersion in size and shape benefit from a focus on post-synthesis processing. All colloidal QD products require post-synthesis isolation from the growth medium and purification to remove byproducts and reduce sample inhomogeneities, that are dominated by dispersions in QD size[1] and shape.[108] The benefits of purification were observed when they were first introduced[64] and have been critical to advancing our fundamental understanding of QD properties.[42] However, purification remained underappreciated until recently as the demand for quality control and purity dominate efforts to integrate QDs into devices and transition QDs as optical materials for commercial production. For a recent review of QD purification approaches, see Greytak et al.[109] Techniques such as ultraviolet−visible−near-infrared spectrophotometry, photoluminescence excitation, Fourier-transform infrared spectroscopy, nuclear magnetic resonance (NMR), thermogravimetric analysis, and calorimetry can help to characterize QD samples and follow purification processes increasingly in real time.

A critical consideration in selecting isolation and purification methods is that the approach must not degrade the desired optical, electronic, or chemical properties of the QDs.[42] These processes typically exploit differences that solvent polarity has on the growth medium and reaction byproduct solubility in comparison to QD dispersibility, or on the mobility (transport properties) contrast between byproducts and QDs, or more subtly, on the dispersibility of different sizes and/or shapes of QDs. Selective precipitation and extraction, ultracentrifugation, ultrafiltration, diafiltration, size-exclusion chromatography, and (di)electrophoretic methods dominate current QD purification strategies.

Precipitation. The process of QD precipitation from solution is ubiquitous as a purification step. This generally involves the addition of a "non-solvent", which is miscible with the solvent dispersing the QDs but incapable of dispersing the QDs themselves. At some concentration, the non-solvent will induce flocculation of the colloidal QDs. The precipitation of the QDs is often accelerated by filtration or centrifugation to remove the flocs from the supernatant. The flocculated QDs can generally be redispersed in a fresh solvent, now free of much of the byproduct of the original synthesis. If the stability of the QDs permits, the process may be repeated multiple times to achieve a desired level of separation and purification.[1,64,110] In addition to removing synthetic byproducts, the precipitation has also been used to refine the size distribution of the samples.[111] Care must be taken to select solvent systems that do not significantly desorb the protective ligand shell during the processing, as ligands can dictate the optical performance of the QDs,[112−116] the physical stability,[117−119] and/or the QD reactivity.[120,121] When non-solvents are titrated into the dispersion, a more controlled flocculation can be induced in which the most attractive (largest) particles in the dispersion flocculate first.[122] This size-selective precipitation method is simple and scalable, although the yield is often limited by the initial breadth of the QD size and shape distributions.[1,64,123] Some choices of solvent (e.g., ODE) or reactions with residual stabilizers, like alkyl phosphonates, have been shown to interfere with the size-selective precipitation processes.[124−127] However, precipitation methods remain the most practiced mode of QD purification. Precipitation from tunable solvents including gas expanded liquids[128,129] and in supercritical fluids[130] has also been explored to allow continuous and reversible adjustment of solvent density and dielectric constant.

Liquid−Liquid Extraction (LLE). Closely related to precipitation, LLE or phase transfer also separates QDs from byproducts based on exploiting differences in solvent polarity and, thus, solubility and dispersibility. LLE offers a potentially gentler process, as the QDs are not flocculated, and thus reduces the risk of irreversible aggregation. LLE-based purification of CdS, CdSe, and CdTe QDs by partitioning the QDs and byproducts between alkanes and alcohols has been demonstrated,[76,131,132] and the effectiveness of the process was improved by the introduction of coordinating phase transfer agents.[133−135] Chloroform/methanol and other solvent mixtures have been used to improve the separation of QDs with recursive application.[132,136,137]

Ultracentrifugation. Ultracentrifugation is a powerful technique that can produce both analytical and preparative scale quantities of QDs. The method separates material based on differential density in high centrifugal fields ($g > 10^5$) and as such can separate the inorganic cores from the free surface ligand.[138] More subtly, it can separate QDs of different size based on their surface-to-volume ratio and the resulting difference in the quantity of surface coordinated ligands. It is most prominently used to isolate materials after some change in surface functionalization.[131,138−141] Ultracentrifugation has also been used to sort QDs with different shapes by exploiting differences in hydrodynamic drag as well as density.[142−146]

Filtration and Dialysis-Based Separation. Porous membranes can be used in dialysis or filtration to remove reaction byproducts and to narrow the initial QD size distribution.[147] Dialysis is most effective in removing excess ligands and other small molecular impurities and can be implemented with a range of commercially available membranes matched for the specific solvents.[148−151] Although dialysis has the benefit that it is quite gentle, it can also be quite slow, taking hours or even days due to the limits of the diffusion coefficients. Filtration is distinct from dialysis in that a pressure difference is applied to push the dispersion across the membrane. However, the size cutoff of the pores will impede the crossing of species above a size threshold. Variants on the filtration process, such as centrifugal filtration,[152−156] ultrafiltration,[157] and diafiltration,[158] add additional driving forces of a centrifugal field or a semi-continuous or continuous flow field, respectively, to enhance separation across the membrane.

Electroseparation/Electrophoresis. The differential motilities of QDs and impurities in the presence of an electric field can be exploited in electrophoresis, with early successes including the separation of polymer-coated CdSe−ZnS[159] and biofunctionalized QDs.[160,161] Unfortunately, the separations are quite slow and difficult to scale. Free-flow electrophoresis (FFE) or continuous flow electroseparation addresses some of these limitations.[162,163] Electrophoretic deposition (EPD) has been extended to slightly polar or even non-polar solvents expanding the separation options[164,165] and to microfluidic processes.[158,166]

Chromatography. In its various forms, affinity or size-exclusion chromatographies have been applied extensively to purify QD samples both at analytical and preparative scales.[167−169] Affinity chromatographies exploit specific and/or enthalpic interaction between the QDs or byproducts and the stationary phase, as aliquots of the QD dispersion are run through the column modulating the concentration of material

https://dx.doi.org/10.1021/acs.chemrev.0c00831
Chem. Rev. 2021, 121, 3186−3233

exiting with time. Size-exclusion or gel-permeation chromatographies affect a separation by allowing the smaller species in the dispersion to explore much more of the porous volume of the support. As such, these smaller, more mobile constituents experience a much longer path length before transiting the column, allowing the species that could not sample that additional volume to exit the column more rapidly.[108,170−173] Chromatography can achieve high-resolution separations, but it is quite time-intensive and costly. As a class of analytical techniques, QD chromatography has been very useful when coupled with online detection (e.g., index of refraction, thermal conductivity, light scattering, absorption, or photoluminescence measurements).

3.2.5. Surface Ligands. Characterization of surface coordinated ligands is essential, as ligands help to mediate QD synthesis and post-synthesis processing, provide physical and chemical stability, and modify surface electronic states.[64,124] Although the introduction of inorganic shells (see section 4) can help to decouple the role of the ligands in modulating the electronic properties of the QDs, giving greater design freedom, the ligands are still an important component of colloidal QD systems. QD−ligand binding during synthesis must be dynamic, but the details of ligand binding and impact of ligand lability upon purification and processing are of increasing interest. Although many descriptions of QD−ligand binding modes have lacked molecular detail, there are examples from single-crystal X-ray diffraction studies for inorganic clusters and small QDs that give some insight[174,175] into the static ligand structure. NMR has also been used increasingly to follow the ligand dynamics.[176−180] It has long been observed that ligand exchange (see section 6.2.2) and even the choice and quantity of solvent used to purify and disperse the QDs can impact QD PL energy and QY.[45,112,181−184] A number of studies saw that merely diluting the QD dispersion leads to spectral changes including PL quenching,[181,185,186] which in some cases is reversible upon introduction of new ligand species to recoordinate the QD surface.[187] Isothermal titration calorimetry has been used to follow the energetics of ligand binding and exchange.[109,188]

Owen et al.[117,189] have introduced an approach to classify different types of QD−ligand interactions based on the nature of the surface bonding. Ligands are labeled as L-type (i.e., Lewis bases that are two-electron donors, such as amines, phosphines, etc.); X-type (i.e., anionic one-electron donors, such as carboxylates, phosphonates, sulfates, alkoxides, halides, thiols, etc.); or Z-type (i.e., neutral Lewis acids that are two-electron acceptors, such as alkyl boranes). The L-type binding exhibited by tertiary amines and phosphines tends to be more labile, showing dynamic exchange in the dispersed state, in contrast to secondary or primary amines or phosphines.[190] For example, primary amines tend to bind firmly even at high temperatures.[191] In contrast, X-type ligands do not readily exchange/dissociate in non-polar solvents, as it requires charge separation. In the presence of a competitive ionic species and a polar environment (e.g., alcohols), both L-type or X-type ligands can be stripped from the QDs and may even result in the removal of surface cations altering the stoichiometry of the QD.[117,135,192−194] Some ligands appear to display multiple binding modes as in the case of thiols, where both exchangeable "surface-bound" thiolates and "crystal-bound" sulfur have been identified on I−III−VI_2 QDs.[195,196]

3.2.6. Ion Exchange. Ion exchange has become a powerful tool for the creation and transformation of QDs and QD heterostructures (see section 4), allowing access to compositions and architectures that are often inaccessible by direct synthesis routes.[197−199] This class of reactions is dominated by cation exchange, the replacement of one metal ion $(M1)^{n+}$ with a second metal ion $(M2)^{n+}$, as smaller metal cations typically have higher diffusion constants compared to their larger anion partners. That said, there is also some precedent for anion exchange.[200,201] Cation exchange was initially introduced to extend the capabilities of aqueous syntheses[202] but expanded rapidly in its use when combined with solvothermally prepared materials.[203,204] In fact, ion exchange has long been known in bulk materials and thin films. However, in bulk semiconductors, the distance of most atoms from the surface is large, making exchange reactions impractical. In contrast, the high surface-to-volume ratio of QDs requires diffusion across only a few unit cells, and the lattice is more compliant to readily allow ion exchange and significant alteration of QD composition or structure.

There are several distinct approaches to ion exchange in colloidal QDs. Generally, a QD is synthesized by a solvothermal procedure, isolated, and then redispersed to allow the cation exchange step to be carried out. Alternately, a competitive cation precursor can be introduced at the latter stages of synthesis, without intermediate isolation of the parent QD, to induce cation exchange in a one-pot process. However, this strategy typically leads to only partial exchange. Cation exchange can yield alloyed QDs, core−shell QDs, and heterostructures with radial or periodic compositional modulation (see section 4.2). In most cases, ion exchange is performed in an aqueous or polar organic QD dispersion, although exchange processes have been carried out on QD thin films.[205] The exchange of isovalent cations is topotactic in most cases, although there may be significant residual strain in the exchanged QD. When the cations undergoing exchange are aliovalent, there is generally a change in the crystal structure and often a change in QD shape, although typically with modest distortion of the anion network. Cation exchange has been demonstrated in II−VI,[206] I−III−VI_2, and IV−VI QDs.[207]

Although a detailed understanding of the mechanisms driving cation exchange is still being developed, cation exchange is already established as a key technique in QD synthesis.[203] For a cation exchange reaction beginning with a QD of composition $(M1)E$, where E is a chalcogen, exposed to a solution containing $(M2)^{n+}$, and thus forming a QD of composition $(M2)E$ and a solution now including $(M1)^{n+}$, cation exchange is broken down into four steps: (1) $(M1)-E$ dissociation, (2) $(M2)-E$ association, (3) $(M2)^{n+}$ desolvation, and (4) $(M1)^{n+}$ solvation. To predict *a priori* the reaction spontaneity,[197] the balance of the (1) association and (2) dissociation relative to the (3) desolvation and (4) solvation energies is assessed. The (1) association and (2) dissociation processes depend on the sum of the lattice and surface energies of the $(M1)-E$ and $(M2)-E$ crystal phases, respectively. A relevant table of enthalpies ΔH is found in De Trizio et al.[203] The (3) solvation and (4) desolvation processes depend on a more specific description of the interaction of $(M1)^{n+}$ and $(M2)^{n+}$ with any ligands and the solvents employed. ΔH for solvation and desolvation tend to dominate the thermodynamics of most cation exchange reactions. The reaction can be favored by selecting ligands and/or solvents that increase the solubility (and thereby the extraction efficiency) of $(M1)^{n+}$ and promote insertion into the lattice of $(M2)^{n+}$. For example, QDs comprised of hard Lewis acid $(M1)^{n+}$ (e.g., Zn^{2+}, Cd^{2+}, In^{3+}, Sn^{2+}) can be readily exchanged for weaker Lewis acid $(M2)^{n+}$ (e.g., Cu^{+}, Ag^{+}, and

https://dx.doi.org/10.1021/acs.chemrev.0c00831
Chem. Rev. 2021, 121, 3186−3233

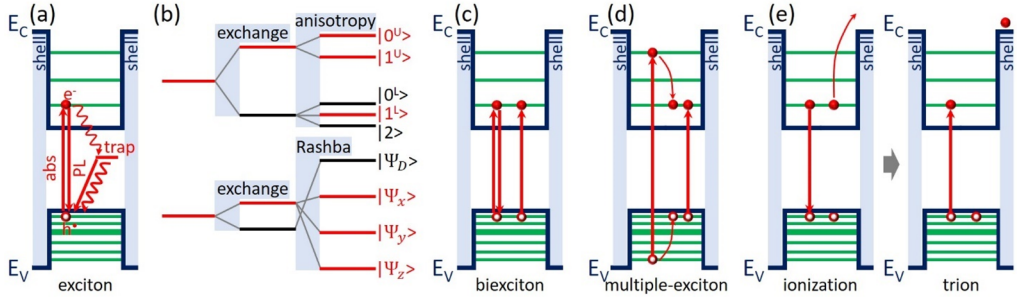

Figure 4. Schematic energy diagrams for (a) single-exciton generation, via interband optical absorption, and recombination, via radiative interband photoluminescence in competition with non-radiative or lower-energy radiative relaxation through trap states; (b) fine structure in the lowest-energy $1S_e1S_h$ transition exemplified for (top) wurtzite CdSe QDs and (bottom) metal-halide perovskite QDs; (c) biexciton generation via sequential photon absorption and radiative recombination; (d) multiexciton generation from a single high-energy excitation; and (e) Auger autoionization and trion generation.

Pb^{2}) when the solvent is a hard base (e.g., H_2O, R−OH). Inversely, weak Lewis acid $(M1)^{n+}$ can be exchanged for hard Lewis acid $(M2)^{n+}$ when soft bases (e.g., tertiary alkylphosphines, amines, and carboxylates) are present in the solvent mixture. The solubility of $(M1)^{n+}$ must be sufficient to allow the exchange to proceed to the desired extent before the solubility limit is reached. In the case of aqueous CdS or CdSe QDs and Pb^{2+}, Ag^{+}, Cu^{+}, Cu^{2+}, or Hg^{2+} ions, the exchange is thermodynamically favored as the solubility of the parent Cd^{2+} exceeds those of the product metal chalcogenides.[208−213] Zn^{2+} ions in ZnS can be exchanged with softer Lewis acid $(M2)^{n+}$ (e.g., Ag^{+}, Cu^{2+}, Pb^{2+}, Cd^{2+}, and Hg^{2+}) in H_2O or polar organic solvents, considering the solubility product constants of these compounds. As examples, these trends lead to a series of transformations "CuS → Ag_2S, CdSe → Ag_2Se or HgSe, PbS → Cu_2S, and ZnSe → CdSe or Ag_2Se".[203] Other exchange reactions have been demonstrated, for example, direct exchange between different divalent metal chalcogenides.

For isovalent cation exchange, it is believed that solid-state diffusion via vacancies associated with Frenkel defect pairs is critical in the cation exchange reaction.[214] The formation energy for these defects helps to establish a thermal threshold for cation exchange. Although many cases of cation exchange have been assumed to be diffusion limited, in which partial and continuous exchange is observed, there is some evidence for cooperativity in some systems as QDs are fully exchanged while others remain in the original state (e.g., in the conversion of CdSe to Ag_2Se or Cu_2Se).[215,216] In systems showing cooperativity, there is a barrier to the incorporation of guest cations (e.g., Ag^{+} or Cu^{+}) in the QD; however, once a guest $(M2)^{n+}$ is inserted, the barrier to a subsequent $(M2)^{n+}$ is lowered, and ultimately, the QD transforms. The volume change associated with cation exchange in some systems can be observed even when the shape of the particle is preserved, but lattice stress (as large as 30% for CdSe → PdSe and CdTe → PtTe) can induce the formation of voids or even fragment the particles.[217]

Anion exchange though less common than cation exchange has a recent exciting example in the development of halide ion exchange in metal-halide perovskite QDs, which display extremely high diffusivity even at room temperature.[218,219] The A- and B-site cations remain in place, allowing the band gap to be tuned across the visible as a function of halide composition.[203,220,221]

3.3. Optical Properties

In this section, we also describe the optical properties of colloidal QDs, that have come from 30 years of study, in order to lay the requisite foundation for more recent exploration of their quantum optical properties, described in section 3.4.

The optical absorption spectrum of bulk semiconductors shows an onset at (for direct band gap materials) or within a phonon energy of (for indirect band gap materials) E_g that increases, as the 3D density of states $g_{C,V} \propto E^{1/2}$ increases with energy, creating a broadband absorption with a linear absorption coefficient of $\sim 10^4-10^5$/cm (depending on composition) at higher energies. Photoexcitation of bulk semiconductors with light having an energy that exceeds E_g creates electron−hole pairs. At room temperature, the Coulomb energy binding the electron−hole pair is small compared to the thermal energy, as the relatively large dielectric constant of bulk solids screens their interaction, and they instantaneously form free electrons and holes. Free electrons and holes with excess kinetic energy rapidly thermalize at ∼1 eV/ps to the bottom of the conduction band and top of the valence band, and—in direct band gap semiconductors—radiatively recombine, yielding luminescence with energies $\sim E_g$. Since the Coulomb binding energy of electron and hole pairs is small, for low-intensity photoexcitation, excitonic luminescence in bulk semiconductors is only seen at cryogenic temperatures (note: PL at the excitonic resonance is possible at elevated temperatures for high-excitation intensities and at ultrafast time scales).[222] Atomic dopants or defects in the form of impurities or vacancies can introduce electronically shallow states or deep states within the band gap of bulk semiconductors. As these defects are typically found in low concentrations ($<10^{18}$/cm^3 for a non-degenerate semiconductor and typically many orders of magnitude lower for unintentional defects), these states are localized. Band-to-defect and defect-to-defect transitions are possible, and they may be observed in absorption and/or luminescence spectra if the energy of the transition exceeds thermal energy. Transitions are characterized according to their luminescence lifetimes, with lifetimes <10 ns typically corresponding to fluorescence from electric-dipole-allowed transitions and longer lifetimes from dipole-forbidden transitions giving rise to phosphorescence. See section 5 for further details on the optical properties of defects and dopants.

In contrast, the atomic-like electronic structure of QDs gives rise to linear optical absorption spectra with discrete excitonic resonances, consistent with the zero-dimensional density of states $g_{C,V} \propto 2\delta$. These transitions are excitonic, as electrons and holes are spatially confined yet delocalized over the volume of the QD and the energy of confinement exceeds thermal energy. For idealized semiconductors with simple band structures, these

https://dx.doi.org/10.1021/acs.chemrev.0c00831
Chem. Rev. 2021, 121, 3186−3233

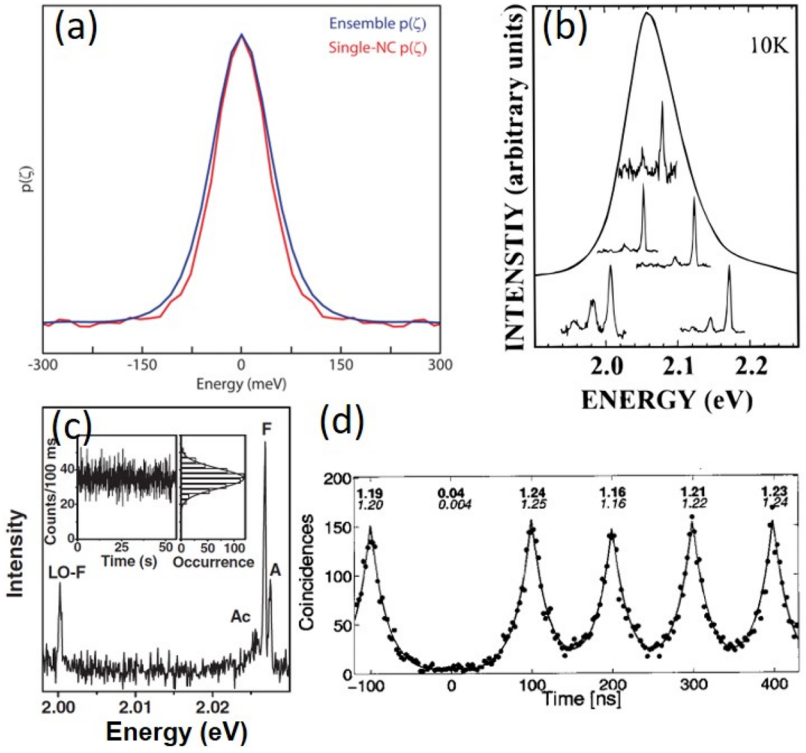

Figure 5. (a) Comparison of the room-temperature PL spectra of an ensemble of CdSe−CdS QDs (blue) and a single (red) CdSe−CdS QD.[244] Reproduced with permission from ref 244. Copyright 2011 The Royal Society of Chemistry. (b) 10 K PL spectra for an ensemble and example single CdSe QDs.[245] Adapted with permission from ref 245. Copyright 1999 American Chemical Society. (c) 2 K, high-resolution PL spectrum of a single CdSe−ZnS core−shell QD and (inset) a time trace of the integrated PL intensity.[246] The labels F and A are also used to represent the dark $|2\rangle$ and bright $|1^L\rangle$ states depicted in Figure 4b, top. Reprinted with permission from Figure 1a of ref 246. Copyright 2009 American Physical Society. (d) Coincidence $g^2(\tau)$ histogram of a single CdSe−ZnS core−shell QD.[247] Reprinted with permission from 247. Copyright 2004 AIP Publishing.

resonances follow the selection rules $\Delta n = 0$ and $\Delta L = 0$ for the difference in the radial and orbital angular quantum numbers between QD states, as introduced in section 3.1.[223] For actual semiconductors with sub-band structures, mixing between the bands, and in QDs with large Coulomb interactions, forbidden transitions with $\Delta n \neq 0$ gain significant oscillator strength (e.g., the $2S_{3/2}1S_e$ transition is the second absorption feature seen in CdSe QDs).[36,37] The absorption coefficient is typically derived from the molar absorption coefficient, since optical measurements are usually carried out on low-concentration QD dispersions in solvents. Its dependence on QD size has been a topic of significant discussion in the community.[224−226] The first excitonic resonance is the $1S_e1S_h$ transition (Figure 4a), which appears at higher energies than the semiconductor bulk band gap. Experimental and theoretical studies show that the first excitonic resonance of small, strongly confined QDs with volume V_{QD} has an absorption coefficient of $\alpha \propto {}^{1}/_{V_{QD}}$, as the bulk oscillator strength is concentrated in these discrete QD states. As the size increases and QDs become weakly confined, the zero-dimensional density of states is no longer accurate. Closely spaced, higher-energy transitions contribute to the oscillator strength of the first resonance, and the absorption coefficient near the band edge is smaller, akin to the bulk semiconductor. Higher-energy transitions are also observed, although the density of transitions increases with energy and the resonance structure is eventually lost, converging to a continuum, again like that of the bulk semiconductor.

Fine structure is further found in the lowest-lying band-edge $1S_e1S_h$ excitonic transition. This structure uniquely arises in QDs from strong electron−hole exchange interactions (∼10−100 times stronger than in bulk semiconductors), given the strong overlap of carrier wave functions confined to the QD, and from anisotropy in the parent semiconductor crystal structure (e.g., for the wurtzite structure), creating crystal field splitting, and in the QD shape (e.g., for prolate or rod-shaped particles).[33,227] The exchange interaction mixes the electron and hole spin states, splitting the excitonic transition into two, where the appropriate quantum number $N = F_h + F_e$ captures the electron−hole correlation (Figure 4b). Exchange interactions and fine structure are significant for QDs composed of semiconductors with large a_{ex}. For most semiconductors, which have an s-like conduction band and p-like valence band, the exchange interactions yield a higher-energy, dipole-allowed, optically bright singlet exciton state and a lower-energy, dipole-forbidden, optically dark triplet state. This is the origin of the "bright" and "dark" exciton model.[227] These states can be further split by the anisotropy in crystal structure and QD shape. In archetypical, spherical wurtzite CdSe QDs, the contributions of exchange interactions and anisotropy form five sublevels, and the lowest-energy transition remains dark (Figure 4b, top). Increasing the QD size[227] reduces the splitting between bright and dark states, $\Delta E_{B-D} \propto r^{-2}$, and tailoring the shape, e.g., CdSe rods,[228] can even reorder the energy of fine structure states, yielding a lower-energy bright state and a higher-energy dark state. As there are always semiconductors that defy the trends, recent studies of metal-halide perovskite QDs, which have an overall s-like valence band and p-like conduction band and an expected significant Rashba effect from strong spin−orbit interactions and broken inversion symmetry,[229] have reported

https://dx.doi.org/10.1021/acs.chemrev.0c00831
Chem. Rev. 2021, 121, 3186−3233

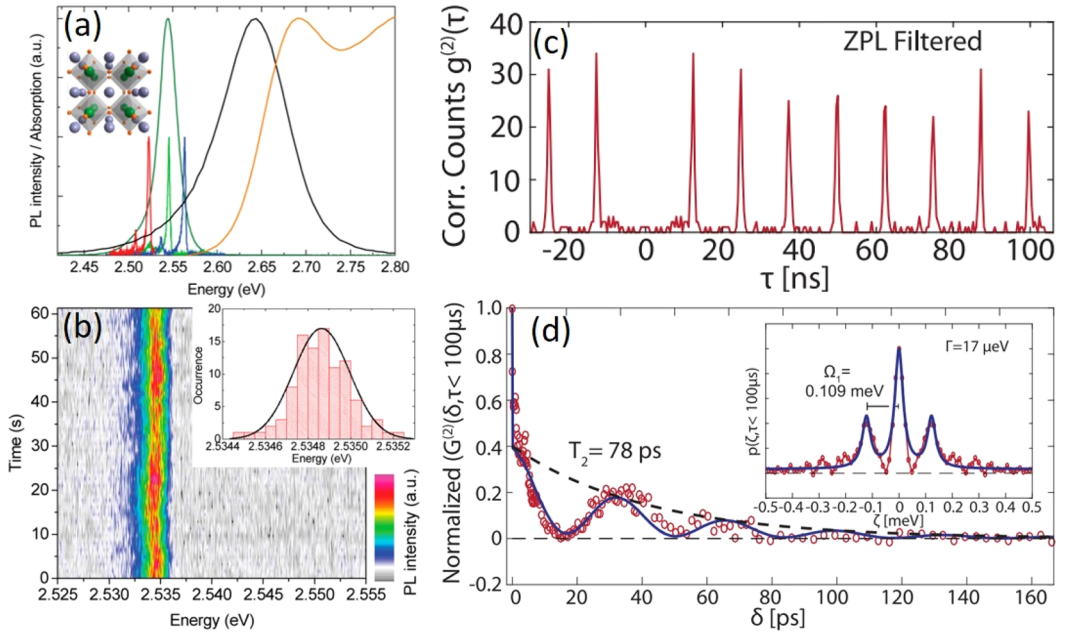

Figure 6. (a) Room-temperature ensemble absorption (orange) and PL spectra (black) and 6 K PL spectra for ensemble (dark green) and example single (red, blue, green) metal-halide perovskite QDs. (b) 6 K PL spectral time trace and (inset) histogram of the peak energy.[248] (a, b) Adapted with permission from ref 248. Copyright 2016 American Chemical Society. (c) Zero-phonon line filtered, correlation $g^2(\tau)$ traces and (d) PCFS interferogram envelope function (red circles) and best fit (blue line), where the decay (black dashed line) yields the optical coherence time T_2. (inset) Spectral correlation $p(\zeta, \tau)$ for $\tau < 100$ μs.[249] Parts c and d reprinted with permission from ref 249. Copyright 2019 AAAS.

an optically bright, low-energy triplet and optically dark, higher-energy singlet dark states (Figure 4b, bottom).[230] As the metal-halide perovskite QDs are newly synthesized and therefore relatively unexplored, there is active debate in the community about the ordering of the bright and dark fine structure states, the effects that contribute to their ordering, and their size and composition dependence.[231−233]

The formation of multiple excitons is more significant in QDs than in bulk semiconductors, again due to spatial confinement of and large Coulomb interactions between carriers.[234] At high illumination intensities, sequential absorption of multiple photons within the exciton lifetime can create biexcitons (Figure 4c) or even tri- or quadraexcitons, where the multiparticle binding energies reduce the energy of the multiple exciton relative to that of the single exciton.[235,236] Multiexciton formation was first observed in pump−probe measurements, where the time scale between excitation pulses was shorter than the lifetime of the excited state, and more recently has been observed in single-QD PL spectroscopy at increasing illumination intensities. Another pathway to create multiple excitons but at low excitation intensities yet with high excitation energies is through a process of multiple-exciton generation (MEG) (Figure 4d).[237−239] Excitation of a "hot" exciton with an excitation energy that theoretically exceeds the band-edge $1S_e1S_h$ exciton energy by more than a factor of two can form two lower-energy $1S_e1S_h$ excitons, i.e., a biexciton, instead of the single exciton thermalizing to the band edge (or "cooling"). MEG is akin to impact ionization that allows for carrier multiplication in bulk semiconductors. However, unlike in the bulk where impact ionization requires conservation of both energy and momentum and "hot" carriers rapidly thermalize to the band edge, the efficiency of MEG is increased in QDs as the need for momentum conservation is relaxed and a decrease in electron−phonon coupling slows carrier cooling. The MEG quantum yield depends on the composition, size, shape, and surface chemistry of the QDs, and the threshold energy for MEG typically exceeds twice the $1S_e1S_h$ exciton energy and depends on the MEG quantum yield. MEG has received significant attention in the community as a route to break the one-photon to one-thermalized, electron−hole pair paradigm that limits the thermodynamic power conversion efficiency, i.e., the Shockley−Quiesser limit, for broadband solar conversion in single-band-gap semiconductor photovoltaic devices.[240]

With exception to the fraction of multiple excitons generated by high-intensity or high-energy illumination of direct band gap QDs, single excitons with excess energy relax to and luminesce from the lowest-energy $1S_e1S_h$ transition (Figure 4a) and are responsible for the size-dependent PL (Figure 1a). In the following discussion, we exemplify the optical and quantum optical properties of excitonic transitions in colloidal QDs for most semiconductor compositions (e.g., II−VI, III−V, IV−VI, and ternaries) by archetypical CdSe cores with and without ZnS or CdS shells (Figure 5) and for recently introduced metal-halide perovskite QDs by $CsPbX_3$ (where X = Cl, Br, I, or their combination) (Figure 6). We highlight InP QDs where there are differences with interesting implications for quantum information and as they are receiving more recent attention as a Cd- and Pb-free composition. Room-temperature, band-edge PL QYs are typically ∼1−10% for most compositions (e.g., II−VI, III−V, IV−VI) of QD cores capped by organic ligands, as unpassivated surface trap states provide an alternative path for recombination, leading to non-radiative or low-energy, radiative recombination (Figure 4a).[241] More recent studies tailoring the stoichiometry and ligand chemistry at the surface have reported considerably higher-PL QYs,[242] although it is unclear that the high PL remains stable over time as the ligated surface is dynamic and often susceptible to oxidation. The growth of inorganic shells to create type-I core−shell QDs (see section 4.2) is known to better passivate surface states and create stable structures with high-PL QYs.[43,44] Optimization of core−shell

https://dx.doi.org/10.1021/acs.chemrev.0c00831
Chem. Rev. 2021, 121, 3186−3233

QD synthesis has delivered samples with near unity QY and small size distributions with narrow ensemble luminescence line widths of <100 meV. The best samples have line widths of <70 meV (~20 nm) for visible emitting QDs, approaching that of the single-QD line width (Figure 5a).[243,244] Metal-halide perovskite QDs are core-only structures with QYs up to 90% and similarly narrow line widths (Figure 6a).[90] The high QYs of core-only structures are attributed to energetically shallow surface states that do not lead to significant non-radiative recombination.

QD sample PL spectra are inhomogeneously broadened by structural dispersity in the ensemble, principally in QD size and shape, which leads to variation in the constituent QD emitting energies. Single-QD spectra were first approached using size-selective, fluorescence line narrowing spectroscopy[250] and then measured as "single-molecule" PL microspectroscopy[245] (Figures 5b and 6a) and solution photon-correlation Fourier spectroscopy (PCFS) techniques (Figure 5a) were advanced.[251] At room temperature, single-QD PL line widths are as small as ~50−60 meV and are limited by exciton−phonon coupling and to a lesser extent by emission from the manifold of states arising from fine structure, which are populated at elevated temperature.[252] Since exciton−phonon coupling and fine structure depend on the composition, size, shape, and surface chemistry of the QDs, thus so does the homogeneous QD PL line width. Low-temperature single-QD spectroscopy reveals spectra consisting of a narrow (<200 μeV), zero-phonon line (ZPL) luminescence accompanied by a longitudinal-optical (LO) phonon progression (Figures 5b and 6a), where the separation between luminescence lines is defined by the bulk LO phonon frequency.[245,253] For small size QDs, the ZPL and its progression are only seen for emission from the low-energy dark state. However, for larger size QDs, higher-resolution spectroscopy shows the ZPLs of both the dark and bright excitons (Figure 5c), as well as acoustic and LO phonon lines.[246] The observation of both dark and bright excitonic PL is consistent with a model of thermal mixing between these bright and dark states, which increases as ΔE_{B-D} gets smaller for larger size QDs, and with a phonon bottleneck, as ΔE_{B-D} becomes small compared to acoustic phonon energies, allowing PL from the higher-energy bright state to compete with thermalization. For InP QDs, ensemble measurements show slow thermalization even allows for PL from the upper bright state, suggestive of weaker exciton−phonon coupling and thus reduced phonon scattering.[254] At cryogenic temperatures, spectral diffusion of the single-QD spectrum is observed on slow (~second) time scales and attributed to fluctuations in the charge environment around the QD for many compositions of semiconductors.[245] Interestingly, this slow spectral diffusion has not been observed in low-temperature measurements of metal-halide perovskite QDs (Figure 6b).[248,255]

The fine structure in the lowest-energy $1S_e1S_h$ transition also has significant effects on the QD sample PL energy, lifetime, and brightness.[256] The occupancy of the manifold of states depends on their energy separation, governed by the size, shape, and composition of QDs (described above), relative to available thermal energy. In QDs from most semiconductor compositions (with p-like valence bands), the QD PL spectrum shows a Stokes shift from its absorption spectrum. The Stokes shift arises from a combination of the fine structure, as photons are absorbed into the high- and low-energy dipole-allowed transitions and emitted from only the lowest-energy transition, and from the PL line shape and its low-energy LO phonon sidebands.[252] In spherical QDs, the lowest-energy state is optically dark and weakly emitting with size-dependent PL lifetimes, which in CdSe QDs are on the order of microseconds at low temperature.[257] The bright state, higher in energy by ΔE_{B-D}, has a lifetime in CdSe QD of ~10 ns. At lower temperatures, the exciton decay depends on the thermal distribution of lower-energy dark and higher-energy bright states.[256] At higher temperatures, the exciton lifetime depends on the partition of emission from the bright and dark states, as well as additional non-radiative effects. At room temperature, both the lower-energy, mostly dark states as well as bright states in the manifold are populated with exciton lifetimes of ~10−100 ns. As described above, the metal-halide perovskite QDs provide a contrasting example with bright, near unity quantum yield PL and $\lesssim$10 ns lifetimes at low temperature and at room temperature.[90]

Single-QD spectroscopies also allow measurement of PL over longer, second-scale timeframes. The QDs reveal PL intermittency, also referred to as blinking, where there are *on* periods of emission and *off* periods where the QD is dark. PL intermittency was shown to be consistent with an Auger autoionization process (Figure 4d) that in older literature was referred to as photodarkening.[258,259] In this process, upon photoexcitation of two excitons (or a biexciton) in a single QD (Figure 4c), the energy of recombination of one exciton, instead of radiating, is transferred to the electron or hole of the other exciton, giving it enough energy to be ejected from the QD core to the nearby surrounding matrix (Figure 4e). This leaves a QD core, typically 2−10 nm in diameter and thus composed of 10^2−10^5 *atoms*, with a single charge. Further excitation would form a three-particle positively charged (two holes and one electron) or negatively charged (one hole and two electrons) trion. Akin to Auger recombination prevalent in highly doped bulk semiconductors, exciton recombination would be non-radiative, and the QD would be dark. The Auger autoionization rate depends on illumination intensity, as higher-intensity irradiation increases the ionization process and shortens the *on* periods; it increases with decreasing V_{QD}, as the need for momentum relaxation is relaxed and Coulomb interactions increase in QDs; and it depends on the composition of the matrix, where core−shell QDs reduce the rate of ionization, showing longer *on* periods, and reduce the rate of carrier tunneling back into the core, establishing longer *off* periods.[3,259,260] More recently, the opening and closing of non-radiative, surface states have also been identified as an additional source of PL intermittency.[261] Non-radiative Auger recombination is detrimental to the performance of many conventional QD-based applications[262] such as low-threshold lasers, reducing the optical gain lifetime;[263] as biological tags, limiting the PL QY; in light-emitting diodes, leading to a buildup of charge and roll-off (i.e., lowered efficiency at high current density and thus brightness);[264] and in photovoltaic devices, reducing the time to extract multiple excitations (i.e., the efficiency of MEG) and thus the advantage of QDs as a generation III material to exceed the Shockly−Quiesser thermodynamic limit for a single-band-gap semiconductor.[265]

Optimization of the shell composition and thickness to create type-II band offsets, giant shells,[266−268] and smoother interface potentials via alloying[269,270] has been pursued to reduce spatial overlap of carriers, and thus the Auger recombination rate and blinking of QDs (Figure 5c, inset) (see section 4). Once again, metal-halide perovskite QDs may provide a contrasting example, with reports of nonblinking QDs at low illumination intensities, as these materials are reported to have electronically shallow surface states that are not effective trap sites (Figure

https://dx.doi.org/10.1021/acs.chemrev.0c00831
Chem. Rev. 2021, 121, 3186−3233

6b).[248,249,255] Blinking is still observed at higher excitation intensities where the Auger process becomes significant. The A-cation site in perovskite QDs can either be a small organic methylammonium or formamidinium cation or inorganic Cs^+. The Auger rate has also been reported to depend on the composition and is slower for organic A-cations, suggesting these organic cations may mediate multiple exciton interactions.[271] The Auger process in most semiconductor QDs competes with multiexciton PL. The design of core−shell QDs of different thickness and composition has allowed the reduction in the Auger process, and the increased efficiency and lifetime of biexciton PL (Figure 4c).[272,273]

Engineering particle shape continues to provide new opportunities to tailor the properties of nanoscale emitters. An example important to include is that of two-dimensional Cd- and Pb-chalcogenide nanoplatelets. The nanoplatelets have thicknesses with integer numbers of atomic layers and are strongly confined only in this one direction; dispersion exists in their lateral dimensions. Since the thickness defines the energy of their PL, ensemble line widths of <40 meV in core only and <60 meV with a PL QY of 90% in core−shell structures are realized.[274−276] Even though these particles also have a fine structure of high-energy bright and low-energy dark excitonic states, they have giant oscillator strengths that yield ∼1 ns lifetimes at room and cryogenic temperature.[274]

3.4. Quantum Optical Properties of Bright, Dark, and Multiple Excitons

Interest in harnessing QDs as quantum emitters stretches back two decades.[277−280] Colloidal QDs represent a complementary materials class to SLE-QDs fabricated by molecular-beam epitaxy and strain-layer overgrowth,[277−280] yet with the advantage of scalable, solution-based synthesis and integration in photonic device architectures (see section 6). Prerequisite for single-photon emission, QDs behave like two-level systems, as low-intensity (and even higher-energy, assuming a low MEG efficiency) excitations rapidly thermalize to the lowest-energy, discrete $1S_e$ and $1S_h$ states and yield narrow line-width, high QY, excitonic PL.[281] The first report of single-photon emission from colloidal QDs was reported[282] in core−shell CdSe−ZnS QDs after the addition of the Hanbury−Brown−Twiss photon coincidence or correlation measurement configuration[283] to single-QD spectroscopy measurements. The autocorrelation function, $g^{(2)}(\tau)$, characterizes the probability for the QD to emit two photons separated by a time τ. In a two-level model, emission of a photon at $\tau = 0$ returns the QD to its ground state, implying that another photon cannot be emitted for a period of time determined by the optical pumping rate and spontaneous emission time (T_1). Thus, single-photon emission is confirmed by observing photon antibunching, i.e., $g^{(2)}(\tau = 0) < 1$. The value of $g^{(2)}(0)$ is a measure of the single-photon purity; values of $g^{(2)}(0) < 0.04$ have been observed for perovskite QDs and <0.004 for core−shell CdSe−ZnS QDs (Figures 5d and 6c).[247,249] Single-photon emission from colloidal QDs can be triggered optically[247,249,284] and electrically.[285]

The creation of indistinguishable photons and control over entangled photon pairs requires optical coherence of the emitted photons, with a characteristic coherence time, T_2, comparable to T_1. Low-temperature measurements of the ZPL width for core−shell CdSe−ZnS QD emission, $\Gamma_{ZPL} \sim 10\ \mu eV$, imply a lower limit for the optical coherence time of $T_2 = {}^{2\hbar}/_{\Gamma_{ZPL}} \sim 100$ ps.[246] Photon echo spectroscopy[286] and the PCFS technique,[249] an interference-based measurement akin to that of Hong−Ou−Mandel, have subsequently been used to measure T_2 directly in colloidal QDs (Figure 6d). At low temperature, both core−shell CdSe−ZnS and $CsPbBr_3$ QDs have a reported T_2 of ∼100 ps.[249,286] However, for CdSe−ZnS QDs, the radiative lifetime T_1 is >10 ns, a consequence of the fine structure in the $1S_eS_h$ transition yielding an optically forbidden, low-energy, dark excitonic state (described above). Thus, $T_1 \gg T_2$. The loss of optical coherence (i.e., dephasing) in the ZPL is attributed to a significant phonon density of states available to assist the spin-flip between higher-energy bright and lower-energy dark states. This is supported by temperature-dependent measurements that show faster dephasing from greater phonon occupation at elevated temperatures. This understanding presents an opportunity to design the electronic structure of QDs through control of their size, shape, composition, and internal structure to reduce ΔE_{B-D} compared to phonon energies and slow the spin flip between bright and dark states, e.g., in larger versus smaller size CdSe QDs or InP instead of CdSe QDs.[254] Even smaller fine structure splitting ΔE_{B-D} and therefore smaller density of lower-energy phonons in epitaxial InGaAs/GaAs is consistent with their long spin-flip times and less significant dephasing from phonon scattering.[287] In contrast, $CsPbBr_3$ QDs are reported to have low-energy optically bright states and, thus, much faster radiative lifetimes with $T_1 \sim 210$ ps, much closer to T_2.[249] In these perovskite QDs, T_2 is hypothesized to still be limited by phonon scattering, although environmental charge and spin noise are anticipated to play a role. Interestingly, the low-frequency spectral wandering observed in most QD compositions as a consequence of charge fluctuations[245] is not observed in metal-halide perovskite QDs. This is attributed to the material's electronically shallow surface states.[248]

The increased PL efficiency and lifetime of biexcitons found by reducing competitive non-radiative Auger processes in core−shell QDs[271,273] present both a challenge and an opportunity for application in quantum information processing. For single-photon emission from excitonic transitions, it is advantageous for the efficiency of biexciton PL to be low.[281] Biexciton PL limits photon purity since it leads to $g^{(2)}(\tau = 0) > 0$. In fact, single-QD correlation measurements have served as a tool to quantify biexciton efficiency.[288−290] The difference in the energy of the single exciton and biexciton (i.e., the binding energy of the biexciton) spectrally separates and allows filtering of the biexciton PL (this was done in collecting the data in Figure 6d).[249] On the other hand, biexcitons can be advantageous as a source of entangled photon pairs.[291] Biexcitons are composed of two electron−hole pairs with correlated electrons and holes having opposite spins. While not yet demonstrated in colloidal QDs, correlation between the carrier spins was proposed and reported to result in anticorrelation in the polarization of the emitted photons in III−V SLE-QDs, creating polarization-entangled photon pairs.[291,292]

Early work also aimed at probing spin coherence in core, wurtzite-CdSe QD samples with and without a CdSe shell.[293,294] In these experiments, rapid dephasing of spin coherence by interaction with the environment was observed. Further studies have explored spin relaxation particularly to understand dynamics within the exciton fine structure of bright and dark spin states.[295,296]

https://dx.doi.org/10.1021/acs.chemrev.0c00831
Chem. Rev. 2021, 121, 3186−3233

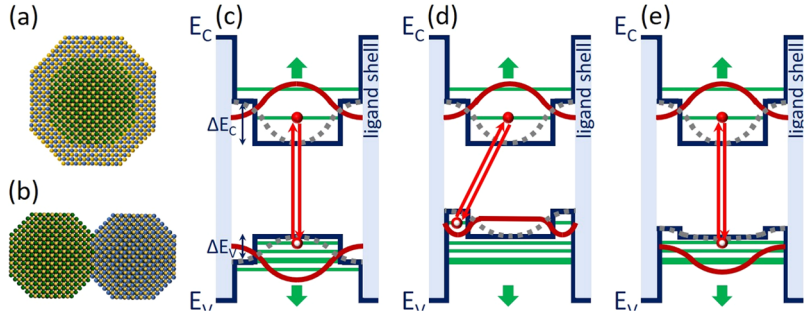

Figure 7. Schematic of (a) radial, core−shell and (b) axial, segmented heterojunctions. Energy diagrams exemplifying (c) type-I, (d) type-II, and (e) quasi-type-II band alignments. ΔE_C and ΔE_V are the band offsets between core and shell semiconductors. The red lines represent the probability amplitude of the wave function $|\Psi(x)|^2$, and the gray dashed lines represent a smoothing of the confinement potential.

4. HETEROSTRUCTURES

4.1. Electronic Structure of QD Heterostructures

Heterojunctions marry two dissimilar semiconductors, often differing in their band gaps and band energies, and are used in "band gap engineering" of semiconductor interfaces to control the behavior of charge and light in device architectures. Heterojunctions are used in bulk and low-dimensional semiconductor electronic transistors and optoelectronic photodiodes and laser diodes to improve device speed and efficiency. In the idealized Anderson model used to construct the band diagrams of heterojunctions (which neglects defects that can form at the interface), the band offsets ΔE_C and ΔE_V give rise to band discontinuities and the carrier types and concentrations of the constituent semiconductors control band bending, forming for non-degenerate semiconductors typical depletion region widths of $\sim$1 μm.[297]

In colloidal QDs, heterojunctions are also commonly introduced, especially in their application as optical materials. Heterojunctions may be formed radially in core−shell QDs or axially in segmented QDs (Figure 7a,b). QD size and composition allow independent control of band gaps and band energies. As the size of QDs is small compared to bulk semiconductor depletion regions, band diagrams look more like those presented for organic semiconductors with discontinuities between bands but without band bending. Importantly, since the electronic wave functions are delocalized across the QDs, heterojunctions enable wave function engineering to spatially control the overlap of electrons and holes.

In sections 3.3 and 3.4 above, we already introduced the importance of growing semiconductor shells on semiconductor cores,[115] without which we could not describe our understanding of their optical and quantum optical properties. Type-I heterojunctions confine the electron and hole to discrete conduction and valence band states in the core (Figure 7c) and have a shell to electronically passivate surface states and reduce Auger ionization key to realizing near unity PL QY. A staggered, type-II alignment separates one carrier in the core and the other in the shell (Figure 7d).[298] Intermediate to those cases are quasi-type-II heterojunctions (Figure 7e) in which the electronic structure presents a small offset in one of the bands, with some discrepancy in whether the offset formally yields a type-I or type-II alignment.[299] Both carrier wave functions reside in the core, but one carrier wave function has a greater extension into the shell. As the shell thickness is increased, the carrier wave function is further extended. In addition to abrupt core and shell junctions that give rise to sharp discontinuities in the energy landscape, alloying is also used to "smooth" the confinement potential in the junctions (Figure 7c−e). The energy diagrams exemplified for different type core−shell heterostructures can be generalized to that of heterodimer architectures (i.e., the energy diagrams of heterodimer QD structures are "half" those of core−shell structures).

4.2. QD Heterostructure Synthesis

Although the ability to access the smallest crystal dimensions and solution processability are prominent advantages of colloidal QD preparations, it may be the potential to heterointegrate different materials at nanoscale dimensions and engineer complex architectures that are the most powerful attributes. Here we describe the synthesis of QD heterostructures with composition modulations radially in core−shell and laterally in segmented heterostructure QDs.

4.2.1. Core−Shell QD Synthesis. Efforts to create such core−shell structures began in the late 1980s with arrested precipitation methods,[43] but research to design core−shells accelerated in the 1990s harnessing solvothermal methods.[44,45,300−303] Growth approaches using small-core QDs as seeds opened the door to a large library of heterostructures that have been realized with the ability to precisely tailor the core size and the shell thickness of epitaxially grown overlayers. The first solvothermally synthesized core—shell structures were a CdSe−ZnSe quasi-type-II system, used to enhance the QY in electroluminescent QD devices.[300,301] In the following years, type-I CdSe−ZnS QDs were produced,[45,302,303] which significantly improved the PL QY and led to the first commercialized core−shell−shell CdSe−CdS−ZnS and InP−ZnSe−ZnS systems, adopted as down-shifting nanophosphors in advanced displays[304] and emerging QD-LED electroluminescent devices.[305]

The selection of the shell material is dictated by the electronic energy alignment desired and the requirement that the two materials have a similar lattice constant and lattice symmetry to allow epitaxial growth.[115] One benefit of the small size and curvature of the core is the greater compliance, allowing epitaxial growth even with a lattice mismatch that would not be tolerated in planar thin films. Shell growth requires precursors that are highly selective and reactive to allow heterogeneous, epitaxial growth of the shell under conditions mild enough to ensure the core materials are not degraded. Initially toxic and pyrophoric reagents like hexamethyldisilathiane $(CH_3)_3SiSSi(CH_3)_3$ and diethyl zinc $Zn(CH_2CH_3)_2$ were employed, but a range of "greener" precursors better suited to scale up have become more popular, including elemental sulfur and zinc carboxylates or dithiocarbamates.

https://dx.doi.org/10.1021/acs.chemrev.0c00831
Chem. Rev. 2021, 121, 3186−3233

In addition to the control of the shell composition, its thickness must be precisely controlled. A shell that is too thin does not efficiently confine the carriers and does not significantly enhance photostability. In contrast, a shell that is too thick and has a non-negligible lattice mismatch will accumulate strain and eventually create defects or induce a transition to island-type growth and roughening similar to the effects exploited in SLE-QD growth. In most cases, core−shell QDs are synthesized in a two-step process. First, core QDs are synthesized and purified. Then, the QD cores are reintroduced to a growth vessel, the dispersion is heated, and a dilute solution of the shell precursors is added dropwise to initiate growth while maintaining the concentration of the shell precursors below the threshold for homogeneous nucleation. The amount of shell precursors added, to yield shell thicknesses of typically 1−6 monolayers, is quantified by measuring the optical absorbance of the cores to find the number density of QDs in solution.[132,306]

A significant advance in shell growth was reported by Peng et al. termed successive ion layer adsorption and reaction (SILAR). In SILAR, the anion and cation shell precursors are added separately and in succession in amounts calculated to provide a single ionic adsorption layer.[307] The QD monodispersity is maintained for CdS shell thicknesses of up to five monolayers. The SILAR method has also been extended to allow the synthesis of "giant" CdSe−CdS QDs. The giant QDs show optical properties that are largely independent of their ligand surface chemistry, which reduces Auger ionization and PL intermittency (as described in section 4.3), when CdS shell thicknesses of 6 nm (i.e., 19 monolayers) and graded CdSe−CdS−$Cd_{1-x}Zn_xS$−ZnS shells are employed.[266,268]

The ion-exchange process (see section 3.2.6) has proven to be a particularly effective route for the synthesis of core−shell and segmented heterostructure QDs when the beginning $(M1)E$ and cation-exchanged $(M2)E$ compositions are immiscible (Figure 8).[203,308−311] In contrast, if the two phases are miscible, cation exchange has been used to dope (see section 5.3.2) and alloy QDs.

4.2.2. Segmented QD Synthesis. A variety of syntheses have been developed to produce segmented colloidal QD heterostructures, such as heterodimers (also referred to as Janus particles) and homodimers, in which radial symmetry is broken but axial symmetry is preserved. Each colloidal particle exhibits inhomogeneity in composition and displays at least two distinct crystalline, inorganic QD domains.[312,313] Interdiffusion or compositional grading during QD growth may lead to diffuse interfaces that can be difficult to characterize.[115] In the growth of heterostructures, an initially prepared QD can be considered a precursor for the transformation into a variety of new structures when in intimate contact with a second distinct QD. The direct coupling leads to strong intra-QD interactions. Heterodimer and homodimer QDs can produce optical and electronic properties not seen in either separate particles or bulk crystals. The inter-QD interactions can be engineered and when sufficiently monodisperse captured in extended self-assembled structures.[314−317] The design of segmented heterostructure QDs offers a route to multifunctional materials for electronic, optical, optoelectronic, biomedical, photovoltaic, and catalytic applications, but scalability will depend on improved reproducibility and yield.[318] Seeded-growth methods are the most extensively studied, although oriented attachment (i.e., solution-phase sintering) and cation exchange approaches are also widely practiced.

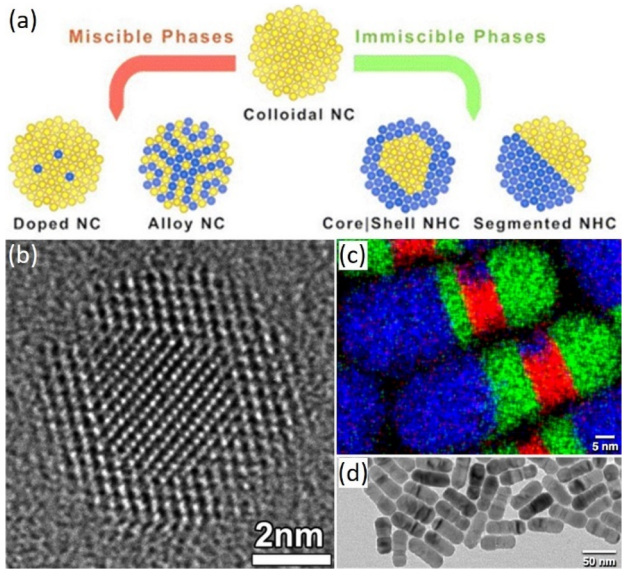

Figure 8. (a) Schematic of ion-exchange reactions to dope and alloy QDs and to form core−shell and segmented QDs or NCs.[203] Adapted with permission from ref 203. Copyright 2016 American Chemical Society. (b) TEM images of PbTe−CdTe core−shell QDs synthesized via cation exchange.[308] Adapted with permission from ref 308. Copyright 2009 American Chemical Society. (c) STEM-EDS maps (Cu is red, Zn is green, Cd is blue, and S is yellow). (d) TEM image of CdS−ZnS−$(CdS-Cu_{1.8}S)$−ZnS nanorods prepared via cation exchange.[309] Adapted with permission from ref 309. Copyright 2018 American Chemical Society.

Seeded growth involves the synthesis of QD seeds and the subsequent growth of a second semiconductor phase on those existing seeds, most commonly using the SILAR method. Seeded growth can be used iteratively to create complex heterostructures, for example, to prepare colloidal double QDs.[319] In this example, on a QD seed, SILAR is used to grow and embed a QD in a rod, forming a dot-in-rod system. Then, a different band gap semiconductor is nucleated and then grown via SILAR preferentially on one end of the rod, thus giving an axially symmetric double QD with a semiconductor spacer.

Solution-phase sintering or oriented attachment has been used to create more complex structures such as PbSe dimers from different size QDs,[320] type-II ZnSe−CdS heterodimers,[321] Au−CdSe−Au (dot−rod−dot) dumbbell heterostructures,[322,323] and CdS−PdS_x−CdS nano-dumbbells.[324] In each of these cases, fusion is triggered thermally or chemically to reduce the repulsive interactions created by surface ligands, thus allowing the close approach and attachment of QDs and NCs.

Partial ion exchange can be exploited for the rapid synthesis of nano-heterostructures[197,325] in which cation exchange and anion exchange can play a role (Figure 8). As discussed in section 3.2.6, cation exchange proceeds rapidly under relatively mild conditions due to their high diffusivities even at low temperatures, while anion exchange is carried out at higher temperatures and over longer times. Cation exchange has been used to form CdSe−PbSe and CdS−PbS heterodimers exploiting partial cation exchange.[326] Alivisatos et al. showed that facet specific Cu^+ exchange could introduce Cu_2S domains into wurtzite CdS nanorods.[208] CdSe−CdS dot-in-rod heterostructures have been used to template the formation of Cu_2Se−Cu_2S,[327] ZnSe−ZnS,[328] and PbSe−PbS[327] dot-in-rod QDs when Cu^+, Zn^{2+}, and Pb^{2+} are exchanged, respectively, for the

https://dx.doi.org/10.1021/acs.chemrev.0c00831
Chem. Rev. 2021, 121, 3186−3233

native Cd^{2+}. Through sequential partial and complete cation exchange, this approach can form multimaterial stripped CdS−ZnS−(CdS−$Cu_{1.8}S$)−ZnS rod-shaped QDs (Figure 8c,d).[309] Cation exchange can also be used to create metal−semiconductor hybrid heterostructures such as Au−CdS and Au/Ag−CdS nanorods. Here, Au nanorods were coated with Ag^+ and then exposed to sulfur to create Au−Ag_2S heterostructures, which were then transformed to Au−CdS by cation exchange with Cd^{2+}.[329]

An example of anion exchange is the production of CdS−CdTe heterodimers from CdS QDs by partial exchange of Te for S.[330] The large 11% lattice mismatch between CdS and CdTe components is thought to limit the extent of exchange. This approach has been used to create CdS−CdSe core−shell nanowires[331] and PbS−PbSe core−shell QDs.[332]

4.3. Optical and Quantum Optical Properties and Applications

In type-I core−shell QDs, the lowest-energy $1S_eS_h$ transition occurs in the small band gap cores (Figure 7c) and optical absorption measurements look similar but spectrally shifted to the red from that of isolated, ligand-capped cores, as the semiconductor shell reduces the barrier height to confinement. The fine structure within the $1S_eS_h$ transition of bright and dark states, and their energy splitting, is also not measurably changed.[333] Transitions in both the core and the shell contribute to optical absorption at higher energies. The epitaxial shell passivates the QD surface and reduces trap recombination and Auger ionization responsible for PL intermittency. Single-exciton PL is characteristic of the QD core band gap (Figure 7c) and produces materials with the highest-PL QY of near unity. It is with these bright core−shell QDs that the measurements of single photons and optical coherence have been made on most QD compositions,[282] as described above (Figure 5), with the exception of the perovskite QDs that show a particularly unusual tolerance to surface states (Figure 6).

In contrast, in type-II QDs, the lowest-energy transition is indirect between the $1S_e$ ($1S_h$) of the core and the $1S_h$ ($1S_e$) of the shell (Figure 7d).[298] Higher-energy transitions occur for states delocalized across the core and shell. The resonances characteristic of the discrete QD transitions of the core are primarily but not completely lost (as the core transitions have greater oscillator strength), and the optical absorption spectra are nearly featureless. The staggered energy landscape is effective for charge separation and transfer of photoexcitations and is pursued for photovoltaic and photoconductive devices. PL is observed at energies characteristic of the indirect exciton (Figure 7d), but with low QY, that decreases as the shell thickness and therefore the spatial separation of electron and hole wave functions increases.

Intermediate, and perhaps most interesting for quantum information science in most semiconductors, are quasi-type-II QDs. The lowest-energy transition is between a confined core state and, with the small band offset, a delocalized state extending across the core and shell (Figure 7e). This offset could be in the valence or the conduction band. Optical absorption spectra show resonances characteristic of discrete states but that are shifted to the red by the lower energy barrier for the confined carrier (as in type-I heterostructures) and by the reduced confinement of the carrier delocalized across the core and shell. Wave function engineering in the quasi-type-II QD band alignment has a significant effect on the fine structure in the $1S_eS_h$ transition.[334−336] As the thickness of the shell material is increased and the probability amplitude for the delocalized carrier shifts more into the shell, the magnitude of the exchange interaction is reduced, and therefore, so is the splitting between the bright and dark states.[334] PL is characteristic of the low-energy transition with reported QYs of >50%. Since the spin-flip between the higher-energy bright and low-energy dark states serves as a source of optical dephasing, the quasi-type-II structure provides an intriguing configuration to explore for quantum information science. Low-temperature measurements of the ZPL dephasing time were reported to increase, as the energy level separation between bright and dark states decreases with increasing core size and shell thickness.[287]

The spectroscopic characteristics of heterodimer QDs have been more limitedly explored to date than core−shell QD heterostructures. However, interest in photovoltaic devices and photocatalysis has spurred studies of heterodimers with type-II or quasi-type-II band alignments. These band alignments allow control over the electron and hole overlap, yet unlike core−shell QDs, they enable collection of both carriers. In particular, the CdE−PbE family of heterodimers has been studied.[326] Absorption spectra show signatures of transitions in both CdE and PbE components with energies that depend on the size of their domains. As the narrow-band gap PbE component increases in size, the PL spectrum changes. Band-edge and trap PL from CdE become less prominent, and indirect exciton (i.e., between the conduction band of CdE and the valence band of PbS) emission is observed. The PL from the PbE component red shifts and eventually grows to dominate the spectrum.[337] In addition, these QDs (e.g., for 50:50 PbS:CdS) advantageously show MEG with a threshold close to $2E_g$, unlike PbS QDs, and a more rapid increase in MEG quantum yield, compared to core−shell QDs. The improved MEG characteristics are attributed to increased Coulomb interactions in the asymmetric, heterodimer architecture, in comparison to spherically symmetric core−shell QDs,[338] and to slow carrier cooling, as carriers interact with a manifold of CdE−PbE interfacial states.

In another example, core−shell CdSe−CdS QDs were fused to create homodimers, akin to coupled QDs grown by MBE but advantageously with smaller QD cores and interparticle spacings to probe more strongly coupled QD molecules.[339] The band-edge absorption and PL of the QD dimers were broadened and red-shifted, compared to a single QD, consistent with quantum mechanical coupling and hybridization of QD core electronic states. Compared to a single QD, the dimers also showed PL with shorter lifetimes, PL intermittency with a broader distribution of energies, and an increase in $g^{(2)}(0)$ indicative of reduced photon antibunching. This behavior is attributed to the multiexciton configurations of biexcitons and trions with different character than those in single QDs, as carriers and excitons can tunnel and reside in different QD cores. For quantum information science, while increased $g^{(2)}(0)$ and PL intermittency are not clearly advantageous, this example of QD dimers shows the possibility of quantum mechanical design of QD homo- or heterodimers. It could be used to optically address and create excitations in one component and then to selectively transfer one carrier to the adjacent semiconductor, e.g., by engineering proper band alignments and interfaces, thus increasing the distance and reducing the interaction between photogenerated electrons and holes and thereby increasing the lifetime of the initialized spin. CdSe/CdS tetrapods have shown ~1 μs spin lifetimes.[340]

https://dx.doi.org/10.1021/acs.chemrev.0c00831
Chem. Rev. 2021, 121, 3186−3233

5. DEFECTS AND DOPANTS

Defects and impurities are ubiquitous and unavoidable in solid-state crystals. Their literature is vast; many defect systems have been intensely studied with the goal of identifying and ultimately eliminating them to improve material purity. Meanwhile, the incorporation of certain defects is desirable, for example, as electronic dopants to tune the charge carrier density or as optically active impurities to tune the absorption and emission of light. In this section, we review the current understanding of optically active defects and dopants in QDs, especially for their use as light-emitting materials and color-converting phosphors. Then, we describe the rapidly expanding role of defects and dopants in bulk semiconductors as spin qubits and light−matter interfaces for quantum information science. Finally, we consider the prospects for engineering and controlling defects and dopants with desirable quantum properties in colloidal QDs.

5.1. Defects and Dopants in Colloidal QDs: History and Background

Defects and dopants modify a material's structural, electrical, and optical properties. In this review, we are primarily interested in optical properties. In semiconductors, crystallographic point defects, including intentional and unintentional impurities, vacancies, and their complexes, introduce midgap states that create new pathways for optical excitation and recombination. Even at relatively low concentration ($<10^{16}$ cm^{-3}, corresponding to ppm levels), such defects can have dramatic effects on a material's optical absorption and emission properties. Some defects provide non-radiative recombination pathways for excitons that would otherwise have decayed radiatively, quenching the material's intrinsic PL (Figure 4a). Other defects introduce radiative decay pathways that produce PL at new wavelengths. The latter class of defects are known as *color centers* or *phosphors*. The term color center is generally associated with defects in insulators such as the halide salts, metal oxides, or ultrawide-band-gap semiconductors such as diamond,[341−343] whereas phosphor refers more commonly to luminescent defects in semiconductors that can be directly pumped optically or electrically through the host's electronic states.[344] Well-known classes of optically active defects include anionic vacancies (often called "F-centers" after the German *Farbzentrum* for color center) and halogen impurities, as well as transition-metal (TM) and rare-earth (RE) ions, which typically substitute for metal atoms in compound semiconductors. The name phosphor derives from the long-lived phosphorescence that is typically associated with TM and RE ions. ZnS, in particular, is a prototypical host material for the study of phosphors because of its large, direct band gap. In 1866, Théodore Sidot reported phosphorescence from unintentionally Cu-doped ZnS while studying its crystal growth. Subsequent development of ZnS and other, primarily transition metal and alkaline earth chalcogenide hosts has produced libraries of well-known phosphor materials which have been used in various electronic display technologies.[344,345]

5.2. Electronic Structure of Isolated Defects

We draw a distinction between shallow and deep defects based on their ionization energy, a measure of the strength of the Coulomb interaction between the defect and charge in the host semiconductor. Shallow donor and acceptor defects have small ionization energies; i.e., their electronic energy states are close to the conduction or valence band edges, respectively, and weak Coulomb interactions. At elevated temperature, the thermal energy, kT, is comparable to the ionization energy and effectively promotes carriers into the bands, such that dopant concentrations define the electron and hole concentrations of semiconductors in the extrinsic regime. The electronic structure of a shallow defect can often be effectively derived from the band extrema of the perfect host lattice. It is modeled like a hydrogen atom where charge is solvated in a medium with the dielectric constant of the semiconductor. Its excited states are weakly bound excitons with optical properties that closely resemble that of QDs. In contrast, deep defects' electronic energy levels lie many kT away from the band edge and are defined by strong Coulomb interactions, giving rise to tightly bound, spatially localized states. The electronic structure of a deep defect is instead derived from the electronic orbitals associated with the dopant and nearby atoms or vacancies, including their modifications by the host crystal field.[346] The number and degeneracy of electronic orbitals can be predicted by molecular orbital theory, which relies on group theory to determine the arrangement of orbitals consistent with the defect's symmetry properties. Coulomb, spin−spin, spin−orbit, and hyperfine interactions further determine the energy ordering and fine structure of the defect's electronic states. Deep defects are also known as R−G (recombination−generation) centers, as they dramatically modify recombination pathways for photoexcitations.

Figure 9 shows examples of two well-studied deep defects—the negatively charged diamond nitrogen-vacancy (NV^-) center[347] (a prototypical spin qubit) and the ZnS:Mn^{2+} system (a classic phosphor).[344] The energy levels are labeled using molecular symmetry notation, which classifies molecular orbitals according to irreducible representations of the point group describing a complex. The notation is widely used to designate both single-particle electronic orbital states and multiplet or spin−orbit states, as in the Tanabe−Sugano diagrams that catalog crystal-field-dependent excited states in coordination compounds.[348] Letters and subscripts correspond to irreducible representations of the relevant point group (C_{3v} in Figure 9a and

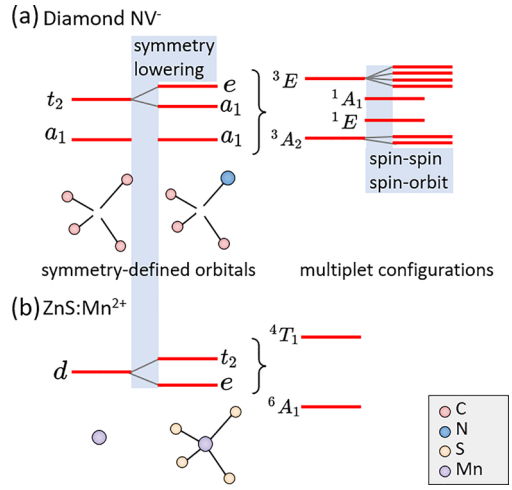

Figure 9. Simplified electronic structures of two well-known defect systems giving rise to deep trap states in their respective hosts. Energy separations are not to scale. Letters and subscripts labeling energy levels are molecular symmetry notation used to describe single-particle orbitals (left) or multiplet states (right). (a) The diamond NV^- center, a complex of a carbon vacancy with a nearest-neighbor substitutional nitrogen. (b) A substitutional manganese ion on a zinc site Mn_{Zn} in cubic ZnS.

https://dx.doi.org/10.1021/acs.chemrev.0c00831
Chem. Rev. 2021, 121, 3186−3233

T_d in Figure 9b), which indicate the symmetry properties of an electronic orbital. Lowercase symbols, such as a_1 and t_2, represent single-particle orbitals, whereas uppercase symbols such as ^3E and $^3A_2$ represent multiparticle states in spectroscopic notation. For example, the $^3A_2$ state in Figure 9a represents the spin-triplet ground state with orbital symmetry A_2 and total spin degeneracy $2S + 1 = 3$. The a_1 and e states in Figure 9a represent linear combinations of carbon and nitrogen sp^3 orbitals around a carbon vacancy, which transform according to the A_1 and E representations of the defect's C_{3v} point group.

In the case of the diamond NV^--center shown in Figure 9a, from left to right, the electronic structure can be thought of as the result of symmetry lowering from the T_d point group of a carbon vacancy to the C_{3v} point group of a nitrogen-vacancy complex. The tetrahedral coordination of dangling sp^3 bonds around a carbon vacancy in a diamond lattice forms a_1 and t_2 electronic orbitals in the vacancy's point group, T_d.[349] With the substitution of a nitrogen atom on a nearest-neighbor carbon site and the symmetry lowering of the defect complex to C_{3v}, the degeneracy of the t_2 orbital is lifted, splitting into a doubly degenerate e orbital and a non-degenerate a_1 orbital. Ground- and excited-state electronic configurations within these orbitals give rise to multiplet states. For the NV^- center, the multiplets are arranged into singlet and triplet manifolds according to their exchange symmetry.[349−352] The states that are manipulated in NV-center-based spin qubits are shown on the right-hand side of Figure 9a: the ground- and excited-state spin triplets, $^3A_2$ and ^3E, which are associated with the defect's characteristic 637 nm ZPL and broadband emission between 650 and 750 nm, and two singlet states, $^1A_1$ and ^1E, accessible via an intersystem crossing between the triplet and singlet manifolds. The decay from $^1A_1$ and ^1E generates emission in the infrared with a 1042 nm ZPL.[353] Degeneracies of the spin and orbital sublevels in the triplet states are further lifted by spin−spin and spin−orbit interactions.

In the case of the ZnS:Mn^{2+} system of Figure 9b, from left to right, we consider the case of a Mn^{2+} ion substituting for a Zn^{2+} site in cubic ZnS, to form the defect configuration Mn_{Zn}. The degeneracy of the partially filled Mn^{2+} 3d-shell is lifted by a tetrahedral crystal field. Electrons can fill these orbitals to form various multiplets including the ground state $^6A_1$ along with the $^4T_1$ excited state. Transitions between these two multiplets cause the characteristic 585 nm emission arising from this system. Several additional multiplet configurations exist, and some are optically active.[354−356]

Because defect electronic structures are shaped by crystal field effects, the position of a dopant inside a semiconductor host profoundly influences the resulting luminescence characteristics, especially in colloidal QDs, in which a high percentage of doping sites are at or near the surface.[33,357−360] Strategies for controlling the spatial distributions of dopant concentrations within colloidal QDs are therefore critical.

5.3. Doping Strategies for Colloidal QDs

An early and current target in the colloidal QD community is the introduction of electronic dopants and optically active impurities.[361] Due to the QDs' small size, adding only a small number of impurity atoms can dramatically change and introduce new physical properties. The introduction of shallow and deep dopants has been used in the design of electronic and optoelectronic devices,[362] to create localized surface plasmon resonances,[363] to enhance photocatalysis and surface redox reactions, and, the topic of this section, to introduce new emissive centers.[364]

Typically, dopant ions have different ionic radii than those in the lattice, and whether they insert substitutionally or interstitially, the dopants often induce lattice strain. Thus, doping may be easier when there is a closer match in the ionic radii of the dopant and host. For example, Mn^{2+} (typically in its high-spin state) is larger than Zn^{2+} but smaller than Cd^{2+}, inhibiting its doping of both pure ZnS and CdS QDs, respectively. However, the doping of alloyed $Zn_{0.5}Cd_{0.5}S$ QDs, with a lattice constant close to MnS, proceeds more readily even up to 7.5% Mn^{2+}.[365] Ions can have the same charge (isovalent) or different charge (aliovalent) than that of the host QD ions. Defects may introduce strain or microscopic needs for charge balance that require thermal treatments to heal.

Here, we focus on strategies to insert impurity atoms and ions that introduce deep electronic states and new emissive centers. These strategies open up a new dimension in QD design and their use as quantum optical materials with control over their charge and spin states.[366,367] In particular, we describe approaches to deliberately dope the core of QDs with TM or RE ions either during the growth of the host QD or by postgrowth cation exchange. It has been shown that ZnS and ZnSe QDs incorporating TM impurities at surface sites exhibit less or no characteristic emission compared to those incorporating TM impurities at core sites, owing to lower crystal field symmetries at QD core doping sites.[358,359,368] We also provide a description of routes to electronically dope QDs by exploiting their surfaces, providing a means to control the carrier concentration and thus charge states of deep level centers.

5.3.1. Doping during QD Synthesis. In bulk semiconductors, dopants and defects are introduced most commonly during growth by substitution in the lattice. Similarly, the incorporation of dopants in SLE and gas-phase-synthesized QDs is achieved by mixing the host and dopant precursor during nucleation and growth. However, the incorporation of impurity atoms in the QD core during synthesis using wet-chemical approaches has proved to be a challenge. Early studies on doping were thought to be limited by "self-purification", i.e., the exclusion of impurities atoms from the core, and later, it was shown that differences in QD shape, surface morphology, and surfactants limited the initial impurity adsorption to the QD surface needed for its incorporation.[369] The different reactivities of the dopant and host precursors limit the choice of precursors to achieve optimum QD size and shape control, and the high mobility of ions makes the balance of QD growth and doping conditions difficult. Early studies also showed that dopants are incorporated in the QD lattice at concentrations often typically an order of magnitude lower than that corresponding to the bulk solubility limit or the concentration in the growth solution. For example, for Mn^{2+} doping, the solubility of Mn^{2+} is more than 10% in bulk II−VI semiconductors, eventually transforming to rock salt Mn-chalcogenides. In contrast, Mn^{2+} is generally incorporated at only a few percent in the lattice of II−VI QDs, and ions often enrich the outer surface of the QDs.[361] While the low solubility of Mn^{2+} in metal chalcogenide QDs was a disadvantage in earlier explorations of these materials as diluted magnetic semiconductors, it in fact may be an advantage in efforts to isolate single dopants in QDs as a platform for quantum information science.

Significant strides have been made in doping of QD cores.[370−377] It was found that, if the nuclei and QDs first

https://dx.doi.org/10.1021/acs.chemrev.0c00831
Chem. Rev. 2021, 121, 3186−3233

formed are kept small initially, surface adsorption of the dopant ions can be favored. The addition of more host precursor can encapsulate and embed the impurities if the growth temperature is kept low.[366,378,379] This has allowed the synthesis of ZnSe:Cu^+ or ZnSe:Mn^{2+} when ZnSe is regrown on the surface of small QDs nucleated in the presence of both the Cu- of Mn-dopants and host precursors. The thermal budget must be kept low to avoid segregation of the impurities, as has been seen in ZnSe:Cu^+ QDs, when heated above 220 °C.[380] Near molecular magic-sized clusters have been employed to seed QD growth and realize more uniform QD doping.[381] These clusters are the smallest, <2 nm diameter QD species, adopting closed-shell configurations with typically <100 atoms in the inorganic core and are thus homogeneous in size, shape, and stoichiometry. Thus, adding a single dopant to a magic size cluster provides <2 nm spatial resolution.

Definitive characterization has always been the greatest challenge to the development of doping. Electron paramagnetic resonance studies of Mn^{2+} in a chalcogenide host provided the first clear evidence of successful doping[382] and the creation of ZnS:Mn^{2+}, CdS:Mn^{2+}, and ZnSe:Mn^{2+}.[357,366,383,384] The synthesis of QDs doped with Mn^{2+} and Co^{2+} progressed in part due to their characteristic magnetic and optical signatures of successful incorporations.[357]

5.3.2. Doping QDs Post-Synthesis by Partial Cation Exchange. When the number of impurities is very small, we can consider cation exchange as a doping methodology rather than transformation chemistry. Again, the small size and large surface-to-volume ratio of QDs means that the doping levels achieved via cation exchange may be quite high by comparison with bulk analogues. As discussed previously, doping by direct synthesis requires a precise balance of precursor reactivity to ensure impurities are incorporated at a controlled rate. This is complicated by the fact that precursor reactivity also impacts particle size, shape, and crystal phase. The incorporation of dopant ions may also be frustrated in synthesis by their greater mobility at high temperature, which can allow dopants to be segregated at surfaces or defects. Thus, cation exchange offers the potential to separate the doping and growth stages.

Norris et al. prepared lightly-doped CdSe:Ag^+ QDs by implementing cation exchange procedures normally used to transform CdSe into Ag_2Se but by adding TOP to mediate and keep the concentration of available Ag^+ very low. QD samples with an average of N = 1, 2, 3, ... Ag-dopants per QD can be attained. PL spectra show a strong modulation in QD emission properties, including sub-band gap defect emission at higher Ag-dopant concentrations and a PL QY that first increases, goes through a maximum at N = 2, and then decreases as N is increased. The modulation in optical properties is proposed to arise from dopant incorporation in a mixture of interstitial and substitutional sites in the CdSe QD lattice. Cation exchange employing hydrazine as a promoting ligand has been used to form ZnSe:Cu^+ QDs and Cu- or Ag-doped $Cd_{1-x}Zn_xSe$ QDs.[385] By exposure of ZnSe to Ag^+ or Cu^+ ions, the respective Zn−Ag−Se or Zn−Cu−Se alloy QDs are produced. Then, in a second cation exchange with Cd^{2+}, the doped $Cd_{1-x}Zn_xSe$ QDs are formed. More complicated dopant systems have also been realized, such as dopants that allow isotopic labeling, namely, positron-emitting ^{64}Cu-doped CdSe/ZnS QDs.[386] Cation exchange can even work to dope small, ∼2 nm "magic-sized" QDs and has been demonstrated in the example of Mn^{2+} doping of ZnTe to produce ZnTe:Mn^{2+} QDs. Even these magic-size QDs show PL spectra that display the $^4T_1 \rightarrow {}^6A_1$ emission characteristic of Mn^{2+} in zinc chalcogenides (described in more detail in section 5.4).[387]

5.3.3. Remote Doping of QDs Post-Synthesis. Since QDs have a large surface-to-volume ratio, the surface provides sites for "remote" doping.[388] Exposure of QDs to gases, liquids, or solids that add surface atoms, ions, or ligands can intentionally or unintentionally introduce impurities and alter stoichiometry and are effective routes to electronic doping.[389] These approaches have been utilized to engineer the carrier type, concentration, mobility, and energy in electronic and optoelectronic devices.[362,390]

Although QDs are generally passivated by long-chain organic ligands, the large surface area makes the QDs susceptible to oxidation and this modest protection may be further reduced when the ligands used in the synthesis are exchanged, particularly for shorter ligands as used in electronic and optoelectronic applications.[357,391,392] The degree and character of QD oxidation can be tuned by illumination, the choice and concentration of ligands, and the size of the QDs.[393] Generally, oxygen serves as a p-type dopant in Pb-chalcogenide QDs, shifting the Fermi level nearer to the valence band,[388,393−395] and creates deeper electron-accepting states in Cd-chalcogenide QDs.[396] Physically adsorbed molecular oxygen can serve as a p-dopant at concentrations low enough to limit irreversible oxidation, while exposure to N_2 gas was seen to impart n-type doping.[397]

Stoichiometry can significantly influence QD electronic doping, as excess anions and cations (or equivalently cation and anion vacancies) create shallow acceptor and donor states,[398−403] allowing the Fermi level to be swept across the band gap with composition. Similarly, the intentional addition of excess atomic species, that will incorporate as the respective ions, can dope the QDs; for example, adding elemental Pb or Se atoms n- and p-dopes Pb-chalcogenide QDs, respectively.[398] Cu_2S has a propensity to form Cu vacancies upon oxygen exposure, leading to doping levels high enough to degenerately dope the QDs and establish a localized surface plasmon resonance.[404,405]

Incorporation of aliovalent dopants is often associated with significant distortion of the QD lattice. However, if the dopants can remain outside the lattice but reside close enough to donate charge, this distortion can be reduced. The adsorption of ions in an electrochemical cell has been shown to dope QDs, leading to the development of interband bleaches in the visible and intraband induced IR features in the optical absorption spectra for charged QDs.[406−408] The introduction of strong reducing agents such as cobaltocene has been seen to completely bleach the first excitonic feature, indicating a very high degree of n-type doping.[409] Just like in methods to control stoichiometry, aliovalent atoms or ions can be added and are effective dopants of QDs. For example, elemental In or In^{3+} has been used to n-dope CdSe QDs.[410−412] Remote doping has also been demonstrated by the close placement of a second QD phase.[413]

5.4. Optical Properties of Doped QDs

In general, there are three classes of optical transitions that can occur in doped semiconductors: band-to-defect transitions, defect-to-defect transitions (participating defects are referred to as donor−acceptor pairs or coactivators), and intradefect transitions within defect-localized states.[414] The transitions are illustrated in Figure 10, along with some of the excitation and relaxation pathways that can contribute to defect-related luminescence in doped QDs. The lifetimes of optical transitions

https://dx.doi.org/10.1021/acs.chemrev.0c00831
Chem. Rev. 2021, 121, 3186−3233

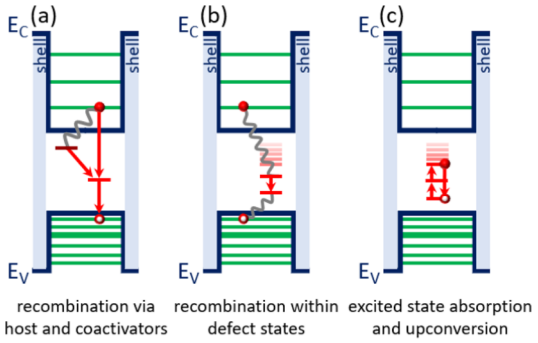

Figure 10. Examples of optical excitation and relaxation pathways mediated by defect-localized states in doped QDs. Following host interband excitation (not shown for simplicity), radiative recombination can occur via (a) band-to-defect and defect-to-defect transitions or (b) transitions within defect states. (c) Especially for transitions with long radiative lifetimes, direct excitation followed by excited state absorption can result in upconversion luminescence.

can be estimated based on the degree to which they are spin- and parity-allowed. This explains in part why, while both electronic structures in Figure 9 arise from point defects in cubic crystals, their different orbital characters, namely, sp orbitals in the case of the diamond NV^- center versus d orbitals in the case of ZnS:Mn^{2+}, give rise to very different optical characteristics.

Following from the nature of the electric dipole operator which determines the oscillator strengths of transitions in quantum systems, transitions between states with the same parities are considered parity-forbidden, and transitions between states with different spin multiplicities are considered spin-forbidden. For example, since the superscripts in the molecular symmetry notation used to label spin−orbit states in Figure 9 indicate total spin angular momentum, it is easy to see that the $^4T_1 \rightarrow {}^6A_1$ transition of Figure 9b is spin-forbidden. In fact, this will be the case for transitions between the ground sextet and any excited d^5 level of the Mn^{2+} ion, which will be a doublet or a quartet.[344] Because these sublevels are formed from the same d orbital, they will also have the same parities and transitions are therefore parity-forbidden. As a result, characteristic emission from ZnS:Mn^{2+} occurs with relatively long, millisecond lifetimes. Similar lifetimes are expected in the case of phosphorescence arising from weakly allowed transitions within the open d- and f-shells of TM and RE dopants, respectively. In contrast, fully allowed transitions such as those between s and p orbitals of a direct-band-gap semiconductor occur with nanosecond lifetimes.[344] The hybridized sp^3 orbital makeup of the optically active spin−orbit states in the diamond NV center makes the characteristic optical transitions spin- and parity-allowed with an emission lifetime of ∼10 ns.[348]

Nominally forbidden optical transitions within the open d- or f-shell of a TM or RE dopant become weakly allowed inside crystalline hosts thanks to spin−orbit coupling and the low symmetry of the crystal field at the dopant site.[415] In the case of RE dopants compared to TM dopants, the open f-shell is shielded from these effects by outer orbitals and does not mix strongly with the s and p orbitals comprising the conduction and valence bands of common semiconductors. Therefore, the oscillator strengths of RE intrashell transitions are even weaker than those of TM dopants. These protected f orbitals offer long spin coherence times and narrow energy line widths.[416] Long-lived defect-localized excited states in systems with such weak optical dipoles are also amenable to upconversion luminescence (UCL), which arises from excited state absorption (ESA) processes. The UCL energy transfer mechanism illustrated in Figure 10c, whereby ESA generates blue-shifted emission relative to the excitation source, is an example of a dopant-mediated process that has been widely exploited in a class of doped QDs known as upconverting nanophosphors (UCNPs).[417] In addition to being affected by crystal field symmetry and spin−orbit coupling, spin selection rules describing impurity intrashell transitions may be further relaxed by exchange coupling between host and impurity spins, which causes spin-flip interactions that explain reduced emission lifetimes in ZnS:Mn^{2+} QDs.[418,419] This exchange interaction is particularly important to quantum optical paradigms that will be discussed in the following sections.

In QD hosts, increased spatial overlap between confined exciton electron−hole wave functions and defect-localized states leads to a high rate of energy transfer, allowing defect-related luminescence from quantum-confined hosts to occur with high quantum efficiency under interband excitation (Figure 10a,b). Historically, the observation of this high quantum efficiency along with reduced emission lifetime (now a source of debate[418,420]) in nanocrystalline ZnS:Mn^{2+}, which is a well-known phosphor in its bulk form, initially drew attention to doped semiconductor QDs as a distinct class of optical materials.[421] Since then, a wide array of TM- and RE-doped semiconductor QDs have been studied and are abundant in display, sensing, and imaging applications, especially Cu^{2+}, Mn^{2+}, and lanthanide ion dopants in II−VI semiconductor QDs.[422] Progress has been heavily motivated by bioimaging applications, wherein colloidal QDs can be incorporated with biological samples of interest, and the large Stokes shifts and long emission lifetimes associated with dopant emission facilitate the separation of signals from background fluorescence.[423] Where QD doping results in dual emission associated with a combination of host and dopant relaxation pathways, the size-dependent band gap of a QD host can also be tuned to control the temperature dependence of the rate of energy transfer between host and dopant states, allowing for the design of solution-processable, ratiometric optical nanothermometers.[424] With the availability of codoping and surface modification techniques to introduce multiple emission pathways within a single QD, white light emission under monochromatic excitation can be achieved for general illumination applications.[425−427] In the case of Cu-doped ZnS, especially, recombination via processes illustrated in Figure 10a,b produces characteristic red, green, and blue emissions in variable proportions within the same material, and confinement effects can further increase the tunability of excitation and emission.[428]

When luminescence results from transitions within TM- or RE-localized dopant states, as in Figure 10b,c, emission energies are relatively unchanged by confinement effects.[33] However, the energy landscapes of QD hosts may offer operational advantages; for example, efficient energy transfer between QD host and defect states resulting from exciton confinement provides a convenient excitation mechanism with a large optical cross section, whereas direct excitation of defect-localized transitions would be weak. Strong association of electron−hole pairs in QD hosts also results in dramatically reduced thermal quenching of dopant emission.[429] While UCL behavior does not arise from confinement effects, colloidal QD hosts are convenient for bioimaging applications, motivating UNCPs

https://dx.doi.org/10.1021/acs.chemrev.0c00831
Chem. Rev. 2021, 121, 3186−3233

based on RE-doped QDs ($NaYF_4$:Yb^{3+},Er^{3+}, ZnO:Yb^{3+},Tm^{3+}) and codoped QDs like ZnS:Mn^{2+},Eu^{3+}.[417,423,430,431]

5.5. Defects as Platforms for Quantum Information Science

In recent years, a new class of defects has emerged. Known as quantum point defects (QPDs),[13] these systems exhibit localized quantum-mechanical degrees of freedom—generally electronic orbital and spin states—that can be coherently controlled using light or electronics.[14−17,23] Well-known examples include the phosphorus donor in silicon;[11] the NV^- center in diamond;[347] the group-IV-vacancy complexes in diamond (e.g., SiV, GeV);[432,433] the divacancy and silicon vacancy in SiC;[434−436] and RE ions such as Er^{3+}, Ce^{3+}, and Pr^{3+} in complex oxides.[437] When introduced at low concentrations such that they do not interact with each other, QPDs are analogous to trapped atoms or individual molecules. They are building blocks for quantum information technologies including quantum memories, quantum repeaters, quantum simulators, and quantum sensors.

5.5.1. Controlling Defect Qubits. To date, most QPD research has concentrated on bulk, group-IV, primarily wide-band-gap semiconductors, especially diamond, Si, and SiC. These materials are attractive hosts for spin qubits due to their dilute nuclear spin bath (which limits magnetic noise), low spin−orbit coupling (which limits coupling to phonons and electronic noise), their availability as high-purity single crystals, and—in the case of diamond and SiC—a large band gap to accommodate isolated electronic ground and optically excited states. Moreover, most well-known QPDs consist of impurity−vacancy complexes that exhibit "molecule-like" s- and p-electronic states confined deep within the band gap. Their ground- and excited-state wave functions are strongly localized on a few atoms surrounding the defect.

In general, optically controllable defect spins arise from QPD structures with widely separated ground and excited state wave functions connected by optical transitions, typically in the visible to near-infrared wavelength ranges. Optical QPDs are usually excited directly through these intradefect transitions, in contrast with phosphor dopants in QDs which rely on indirect excitation via the host followed by exciton-mediated energy transfer (Figure 10). Subsequently, these QPDs emit photons through the same intradefect transitions, although the emission is often Stokes shifted to longer wavelengths due to vibronic coupling. For the QPDs such as those of Figure 11 with dipole-allowed transitions between hybridized s and p orbitals, typical optical decay lifetimes are primarily independent of temperature at ∼10 ns, and the spectral line shape consists of a ZPL accompanied by a phonon sideband.[346] The ZPL narrows as the temperature is reduced, exhibiting optical coherence below ∼10 K in pure samples,[438,439] whereas the shape of the phonon sideband is mostly independent of temperature.[440] QPDs further possess fine structure in their ground and excited states, which can be observed at low temperatures as a set of energy-resolved transitions in the ZPL. As described in section 5.2, the QPD electronic structure results from orbital splittings due to symmetry breaking in the crystal field, spin−orbit coupling, spin−spin coupling between unpaired electrons, and hyperfine interactions with atomic nuclear spins. The spin and orbital energy levels can be further shifted through the application of magnetic, electric, and strain fields.[441,442]

In order to use QPDs as spin qubits, mechanisms must be available to initialize and read out their spin and orbital degrees of freedom. Spin initialization and readout is typically achieved

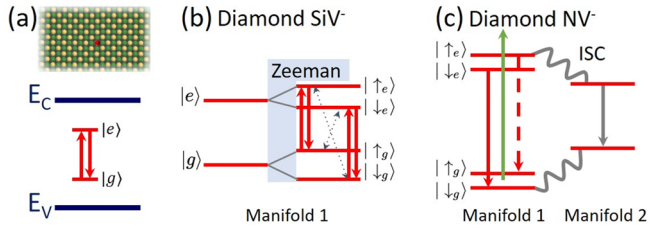

Figure 11. Simplified electronic structure of prototypical QPDs. (a) Illustration of a QPD in a bulk semiconductor host and its corresponding energy diagram. (b) The Zeeman-split ground and optically excited states within an effective spin-$^1/_2$ manifold of a diamond SiV^- center, addressed using resonant optical excitation. Optically addressed, spin-conserving transitions are indicated by solid arrows, and spin-flip transitions are indicated by dashed arrows. (c) Two distinct spin manifolds coupled by a spin-dependent intersystem crossing (non-radiative process indicated by wavy lines) in a diamond NV^- center, which allows for non-resonant optical spin initialization and readout. The arrows within Manifold 1 indicate transitions which are optically addressed, with emission occurring at similar energies but with different intensities (lower intensity is indicated by a dashed line) due to the spin-dependent intersystem crossing. The transition shown within Manifold 2 produces infrared emission and is not generally addressed for spin control.

in one of two ways, as shown in Figure 11b,c. The first method, resonant optical pumping of the individual spin-resolved transitions, is shown in Figure 11b. This scheme is appropriate for systems with relatively simple fine structure, like the spin-$^1/_2$ levels associated with a single unpaired electron in the diamond SiV^- center. The operating principle in this scheme is that resonantly pumping the optical transition associated with one spin state eventually depopulates that spin state in favor of the other if there is any spin-flip relaxation process available. The transition strengths associated with spin-conserving and spin-flip transitions depend on the QPD's symmetry, spin−orbit coupling, and the relative orientation of an applied magnetic field. In some cases, the transitions can be arranged such that resonant pumping of one transition by a tunable laser efficiently polarizes the ground-state spin, while resonance fluorescence from a spin-preserving transition enables high-fidelity spin readout. This is essentially the same mechanism that is used for initialization and state-readout of trapped ion qubits.[9,443−445] A variety of related schemes exist, depending on the details of each QPD's fine structure. Examples include the SiV^- and NV^- centers in diamond,[432,433] the silicon vacancy (V_{Si}) in SiC,[446] and the Er^{3+} ion in Y_2SiO_5.[416] Resonant optical control facilitates spin initialization and readout with high fidelity, which is crucial for spin−photon interfaces used in quantum communication.[15,16] However, these schemes require stable, narrow, optical transitions that are presently available only for QPDs in high-purity bulk substrates at cryogenic temperatures.

The second typical approach to addressing QPD spin states is illustrated in Figure 11c and is most famously applied with the diamond NV^- center. For this defect, a fortuitous arrangement of spin-triplet and spin-singlet states leads to optical dynamics modulated by a spin-dependent intersystem crossing (ISC) between the triplet and singlet manifolds (Manifolds 1 and 2 in Figure 11c, respectively). ISC processes are incoherent, non-radiative transitions that are facilitated by phonons and spin−orbit coupling; they are a common feature of many molecules and defects.[447] In the NV^- center, the ISC provides a relaxation pathway (indicated by wavy gray lines in Figure 11c) that preferentially populates the $m_s = 0$ spin sublevel of the ground-

https://dx.doi.org/10.1021/acs.chemrev.0c00831
Chem. Rev. 2021, 121, 3186−3233

state triplet (denoted $|\downarrow_g\rangle$) when the center is non-resonantly illuminated by a laser that equally pumps all spin states.[448,449] Based on this spin-selective ISC, spin initialization usually consists of an illumination period following which the center has a certain probability of having relaxed into the $|\downarrow_g\rangle$ state and a significantly lower probability of having relaxed into the $|\uparrow_g\rangle$ state, or $m_s = \pm 1$ sublevel. Furthermore, the spin-selective ISC creates a fluorescence contrast between the spin states given the different emission energies and lifetimes associated with relaxation through each manifold. In practice, the infrared emission produced by relaxation through Manifold 2 is not collected, and this singlet manifold is a shelving state that partially quenches the red emission from Manifold 1. The resulting fluorescence contrast allows for robust optical spin readout.[450] Although the initialization and readout fidelities associated with the NV^- center's ISC dynamics are not as high as those that can be achieved using resonance fluorescence, the mechanism is compatible with room-temperature operating conditions, since it does not rely on resolving fine structure in the optical transitions, and the spin-dependent ISC rates are relatively insensitive to noisy environments. These features have enabled the wide range of applications for NV^- centers as room-temperature qubits and versatile quantum sensors. More recently, similar ISC mechanisms for spin initialization and readout have been used to address the divacancy and silicon-vacancy QPDs in SiC,[434,435] and they are believed to explain room-temperature, magnetic-field-dependent fluorescence for QPDs in hexagonal boron nitride.[451,452]

5.5.2. Identifying New Quantum Point Defects. There is growing interest in identifying QPDs in new host materials and different QPD classes that would enable new forms of optical or electronic quantum control. The interest in exploring new materials is driven by the realization that different applications in quantum information science demand different QPD functionality, which in turn is related to different properties of the defect and its host. For example, quantum photonics requires pure, stable sources of single photons, whereas spin-based quantum sensors require a robust mechanism for spin initialization and readout that is compatible with the sensing modality. These considerations have motivated researchers around the world to investigate optically active defects in wide-band-gap II−VI and III−V semiconductors such, as ZnO,[453] ZnS,[454] and GaN,[455] as well as in layered van der Waals materials, such as WSe_2 and hBN.[456,457]

Defect identification based on spectroscopic observations alone—especially of individual defects—remains a major challenge. In bulk crystals, observing spatially resolved fluorescence from individual defects using standard confocal microscopy techniques requires a concentration below $10^{11}/cm^3$; this is many orders of magnitude smaller than the background impurity concentrations in most crystals. Hence, defects that exist as single-photon emitters in bulk crystals are generally rare defects, coexisting with other defect species at much higher concentrations. This complicates efforts to identify fluorescent defects by controlling synthesis and treatment conditions, and it is one reason why many of the defects responsible for the emission observed in the materials listed above remain unknown.

An alternate approach to QPD development has been to use nanofabrication and spectroscopic techniques in order to isolate individual qubits from well-understood families of optically active impurities that exist at higher concentrations. This approach has met particular success in the case of RE ions, which are well-known for their coherent optical properties as ensembles in laser crystals.[437,458] Several RE species have been isolated at the single-ion level, including Pr^{3+},[459−461] Ce^{3+},[462−464] Nd^{3+},[465] and Er^{3+}.[416,466,467] The major challenge in controlling individual RE ions is the small oscillator strength associated with the dipole-forbidden f-shell transitions, which leads to very long optical lifetimes and an inability to detect individual fluorescence photons. In the works above, the problem has been addressed either by utilizing dipole-allowed 4f−5d transitions from higher-lying electronic levels (in the case of Pr^{3+} and Ce^{3+}) or by enhancing the emission rate of the 4f transitions by coupling the ions to a nanophotonic cavity (in the case of Nd^{3+} and Er^{3+}). In a complementary approach, Yin et al. demonstrated electrical readout of photoionization for Er^{3+} in silicon.[466] In all of these cases, individual ions are isolated from a dense ensemble using resonant excitation to select particular transitions from the larger inhomogeneous distribution.

QPDs based on TM impurities in bulk semiconductors have also emerged in recent years as an interesting class of spin qubits. Examples include Fe^{3+} in ZnO[468] and Cr^{3+} and V^{4+} in silicon carbide.[469−472] Similar to RE ions, TM impurities feature long-lived spin states and stable optical transitions associated with d-level orbitals that generally do not participate in bonding and hence are decoupled from their environment. There are some exceptions to this rule, however, and in some configurations, the d-shell can become bright, either through strong symmetry breaking or hybridization with s and p orbitals. This seems to be the case, for instance, with recent reports of short lifetimes for V^{4+} ions in SiC that emit in the telecom band.[471,472]

In all of these emerging material systems, there is a pressing need for improved control over QPD synthesis and device fabrication to realize atomically precise, multiqubit arrangements of QPDs that would enable scalable quantum computing or quantum simulation of more complex systems. Despite decades of research and steady progress,[473] our ability to control the formation and localization of the best-known QPDs in diamond and SiC remains limited.

From this perspective, colloidal QDs are especially attractive platforms for engineering defect-based spin qubits. Many of the most common QD materials, including ZnS, ZnO, and CdS, are characterized by large band gaps, relatively low spin−orbit coupling, and dilute nuclear spin environments—all ideal characteristics for a QPD host.[13,474] These materials are well-known hosts for phosphor dopants, including TM and RE ions. Furthermore, colloidal QDs can be synthesized with near-atomic precision, arranged into complex assemblies, and incorporated in optoelectronic devices. The key missing ingredient is a robust spin qubit that can be initialized, controlled, measured, and—ideally—coupled coherently to light. We discuss the opportunities and challenges associated with this endeavor in the next subsection.

5.6. Identifying and Engineering Spin Qubits in Colloidal QDs

A comparison of the optical excitation and detection mechanisms for common phosphor dopants in QDs versus the QPDs discussed in the previous subsections highlights several similarities and differences. Generally, defects in QDs are excited indirectly through the QD absorption transitions, which subsequently relax through the defect levels via a combination of non-radiative and radiative transitions. In contrast, QPDs are typically excited directly through resonant optical driving or non-resonant, vibronic excitation of the intradefect transitions.

https://dx.doi.org/10.1021/acs.chemrev.0c00831
Chem. Rev. 2021, 121, 3186−3233

Moreover, most of the well-known QPDs involve light elements such as N and Si in complexes with vacancies, whereas phosphors are often substitutional dopants of TM or RE ions. Nonetheless, many phosphor dopants in QDs exhibit nonzero spin states isolated within the band gap, and they could be utilized as spin qubits given appropriate mechanisms for initialization and readout. Several potential mechanisms exist, as we will discuss in this section. In fact, optically detected magnetic resonance (ODMR) has been associated with several phosphor transitions in bulk II−VI crystals.[475] Observations of ODMR are often a first step toward developing protocols for optical spin control. In particular, we propose that TM and RE dopants in colloidal QDs are prime candidates for development as spin qubits.

5.6.1. Unique Characteristics of Defects in Colloidal QDs. Colloidal QDs provide many advantages for qubit design. One is size; a 5 nm-diameter QD contains only ∼6000 atoms, and the particles can be dispersed and arranged for individual study. This relaxes the doping concentration requirements to spatially isolate individual impurity atoms with optical microscopy from an essentially unattainable $10^{11}/cm^3$ in bulk crystals (part per trillion levels) to a much more reasonable level of ∼100 ppm. Furthermore, for semiconductor QDs, it is possible to consider unique spin−photon interfaces that harness both the large oscillator strength of the QD host and the long-lived coherence of the impurity-localized electronic spin. Quantum confinement in these structures strongly increases the spatial overlap, and accordingly the exchange interaction, between impurity-localized spins and resonantly generated electron−hole pairs, allowing for optical orientation of the defect spins via host excitation.[419] The optical cross-section of this light−matter interface is much larger than that of traditional QPDs, which are optically addressed inside bulk semiconductor hosts by direct excitation of defect states. Other advantages related to defect spin control and readout that are associated with the low dimensionality of QD hosts include reduced decoherence caused by host nuclear spins,[476] inherent proximity of the QPD to surfaces that facilitate external couplings for quantum sensors, and the ability to precisely control the QD surface chemistry.

5.6.2. QPD Synthesis: Challenges and Opportunities. The synthesis methods described in section 5.3 represent recent advances in overcoming challenges to dope colloidal QDs, by inserting impurities in the core or by adding atoms, ions, or ligands at the surface. However, doping the core and remote doping through the surface may provide different utilities to engineer quantum defects and dopants. As we described above, the crystal field of the core is important in creating the defect electronic structure and thus in establishing the manifold(s) of charge and spin states that govern the energy and dynamics of their luminescence.[33,357−360] Meanwhile, defects and dopants introduced at the QD surface have proven to be very effective as electronic dopants. Unlike other QPD nanoparticles (e.g., nanodiamonds), the surface chemistry of colloidal QDs is well-established and well-controlled, with known libraries of and processes to introduce surface species, such as metal and chalcogen atoms; metal, chalcogen, and halide anions; and organic (e.g., short, long, and polymeric; redox active; etc.) and inorganic ligands.[41] These surface chemical species can shift the absolute energies of the QD conduction and valence band states.[46] They can be used to tailor electron and hole concentrations from low to high, shifting the Fermi level through the band gap.[389] Surface modification provides an opportunity to control the charge state and thus luminescence of core defects and dopants.

The methods used to dope the core through direct introduction of precursors in synthesis often yield a high level of doping in QDs. In contrast, ion exchange has been shown to yield light doping, even to realize single defects or dopants in the QD core.[477] There is also an opportunity to deterministically position defects within the QD. Deterministic doping could be achieved by exploiting the facet selective adsorption energy for different ions.[366,369] Radial control of doping can be achieved using small doped seeds and overcoating them with additional material to grow larger particles.[372] True digital doping may be possible by employing magic-sized clusters, which yield molecularly precise seeds.[478−480] In addition, a nucleation doping route has gained in popularity, in which dopants are introduced at the nucleation stage and retained in the growing QD.

5.6.3. Quantum Control Strategies for QPDs in Colloidal QDs. As discussed in section 5.5, there exist several different ways to address and control QPD spin states in bulk semiconductors. In addition to these established schemes, the colloidal QD architecture presents exciting alternative strategies for quantum control that leverage the QD's unique physical and optical properties. Some of these are discussed below.

Direct QPD Excitation through Spin-Selective Transitions. Especially for wide-band-gap QDs such as ZnO and ZnS, it may be possible to identify QPDs similar to the nitrogen-vacancy or silicon-vacancy center in diamond, for which optical ground and excited states are both accessible and protected deep within the band gap. In fact, the quantum confinement effects that enlarge the effective band gap can make this condition easier to achieve in QDs compared to bulk crystals. In such cases, QPD spin states can be controlled via resonant or non-resonant excitation through spin-selective transitions, as shown in Figure 11. The key advantage of non-resonant techniques is their potential to work at elevated temperatures; however, they require a particular arrangement of energy levels and spin-dependent relaxation processes. On the other hand, resonant control schemes can be developed for essentially any arrangement of levels, assuming spin−orbit or hyperfine interactions produce variations in the fine structure of the optically excited state compared to the ground state. These schemes require low temperatures and stable optical transitions protected from spectral diffusion, but they directly enable a wide range of approaches to coherently couple spins with light,[23] including the generation of spin−photon entanglement,[481,482] all-optical coherent spin control using coherent population trapping and ultrafast pulses,[483−488] and nanophotonic quantum-electrodynamics platforms to interface individual spin qubits in optical cavities with coherent photon states.[489,490]

The identification of suitable QPD candidates and corresponding colloidal QD materials is a challenging problem, but rapid progress in *ab initio* theory and new experimental characterization techniques is making a targeted search seem tractable.[13] Several potential QPD candidates are already known from the literature, including defect-bound excitons in ZnSe[491−493] and ZnO[494] and defect-related single-photon emitters in ZnO[453,495,496] and ZnS.[454] Furthermore, ODMR signals associated with defects have been detected in many II−VI bulk crystals,[475] raising the clear possibility that non-resonant optical spin initialization and control schemes can be realized in these materials.

https://dx.doi.org/10.1021/acs.chemrev.0c00831
Chem. Rev. 2021, 121, 3186−3233

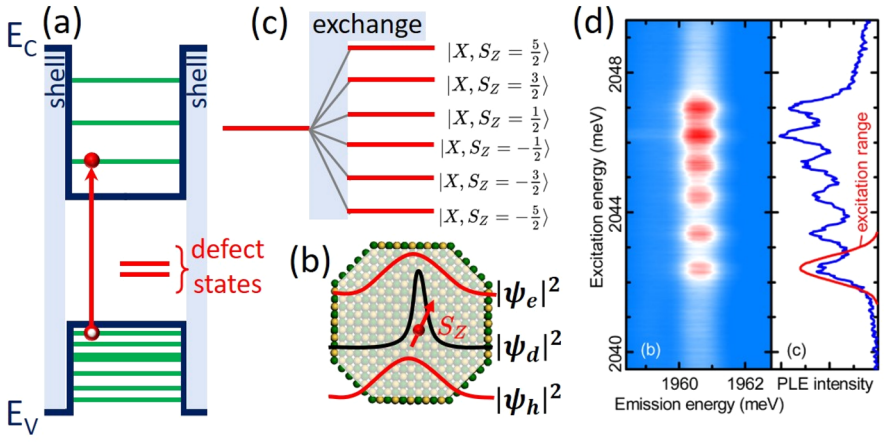

Figure 12. (a) Energy diagram of a QD containing a deep defect with spin sublevels and a strongly confined exciton. (b) Illustration of the QD in part a with a red arrow to indicate that the defect has a localized magnetic moment. S_z is the defect's spin projection along a measurement axis. Spatially overlapping probability amplitudes of the confined exciton electron and hole wave functions (red) and the defect electronic wave function (black) results in strong exchange coupling. (c) Excitonic fine structure in the exchange field of the dopant-localized magnetic moment. Corresponding to the case of a Mn^{2+} impurity ion with $S = {}^5/_2$, six composite exciton−dopant ($X - S_z$) states are shown. (d) Photoluminescence excitation spectrum showing the excitonic fine structure resulting from exchange coupling in a CdTe:Mn^{2+} QD. Excitation occurs in the QD with a single Mn^{2+} ion, and emission occurs in a neighboring, undoped QD. The red curve indicates the spectrum of a pulsed laser used for state-selective excitation.[500] Panel d is reprinted from Figure 1b,c of ref 500 with permission. Copyright 2014 American Physical Society.

Utilizing QD Resonances for Spin Control. For defects in bulk crystals, there is a clear difference between QPDs whose electronic wave functions are composed of hybridized s and p orbitals and those like the substitutional TM and RE ion impurities whose spin states reside in d or f orbitals. The former exhibit efficient optical excitation and high brightness due to their electric dipole transitions, whereas the latter generally exhibit weak optical transitions that are dipole- or spin-forbidden. For defects in colloidal QDs, however, the electronic and optical structure of the quantum-confined host provides an alternative means to address the spin levels of QPDs with weak optical transitions.[335]

In particular, a localized magnetic moment associated with a TM-ion impurity confined in a QD alters the energy diagram of the host via sp−d exchange coupling, as illustrated in Figure 12a−c. The exciton transition is split into sublevels that are selective for the projection of the TM impurity's spin. Several authors have exploited the excitonic fine structure resulting from sp−d exchange coupling to demonstrate initialization and readout of individual Mn^{2+} spins in doped, MBE-grown, II−VI semiconductor QDs.[497−500] In these experiments, the Mn-exciton spin-state population depends upon both the energy and helicity of the optical excitation. Following an excitation sequence, the resulting Mn spin-polarization can be read out based on the absorption selectivity (Figure 12d) of a subsequent excitation or the emission energy of the system.[501] Furthermore, excitation or emission can occur within a single QD or upon energy transfer via a neighboring, undoped QD. In the latter case, spin-polarized carriers retain their polarizations during the transfer between hosts with a sufficient rate to enable initialization mechanisms based on the helicity of the optical excitation.[502]

These experiments highlight the ability to harness the large optical cross sections associated with QD exciton transitions in order to control spin states associated with highly localized TM impurities that are otherwise challenging to access. In the future, it will be interesting to consider alternative TM and RE species, especially those with a simpler spin structure than Mn^{2+}, which has $S = {}^5/_2$ and therefore six potential spin states. It is also interesting to consider variations on the initialization and readout protocols, where excitation or emission occurs either through the exciton transitions or the intralevel defect transitions.

Cavity Enhancement. An alternative approach to enhancing weakly allowed d- or f-shell transitions is to use optical cavities to enhance the local density of optical states at the relevant photon energy. This approach has been used successfully to detect photons from RE ions in bulk complex oxide crystals coupled to nanophotonic cavities.[465,467] Aside from the Purcell effect that enhances the emission rate, the emitted photons are efficiently coupled into the cavity's well-defined spatial mode, which increases the collection efficiency and enables routing of photons between devices. Furthermore, the cavity coupling has been shown to improve the cyclicity of nominally spin-preserving transitions used for spin readout (see Figure 11b, for example) but which suffer from non-radiative spin-flip relaxation in the absence of a cavity. This improves the fidelity of spin initialization and readout, and it has enabled quantum nondemolition measurements of individual Er^{3+} ions.[416] Building on these recent advances, the small size of colloidal QDs coupled with advanced protocols for top-down and bottom-up assembly (see section 6) present opportunities for realizing efficient, compact, nanophotonic quantum devices based on individual spin qubits hosted in QDs.

Addressing and Controlling Nuclear Spins. In addition to a QPD's electronic spins, individual nuclear spins associated with the host impurity or proximal atoms offer quantum-mechanical degrees of freedom that can be used for memories,[503−506] local quantum processing,[507−510] and enhanced quantum sensing.[511,512] Many II−VI colloidal QD materials have naturally low concentrations of nuclear spins, and the concentration could be further reduced through isotopic purification during synthesis. Especially considering the potential to synthesize core−shell QDs or other structures deterministically incorporating QPDs with near atomic-resolution precision, it becomes feasible to imagine an architecture consisting of an electron-spin

https://dx.doi.org/10.1021/acs.chemrev.0c00831
Chem. Rev. 2021, 121, 3186−3233

QPD qubit connected to a small register of nuclear spins within the QD core, while the outer shell is purified of nuclear spins that would otherwise cause decoherence. Such an architecture, especially if coupled to light in an optical cavity, could serve as a multifunctional quantum memory node as part of a quantum repeater.[513]

Alternatively, the nuclear spins could be utilized to enhance the QPD's quantum sensitivity to external stimuli, including the coherent dynamics of nuclear spins associated with molecules outside the QD. Molecular-scale NMR is one of the most important future applications of quantum sensors.[514] The leading nano-NMR platforms are based on shallow NV^- centers beneath the surface of bulk diamond, but their performance is limited by a lack of control over the diamond surface chemistry.[515] A nanoparticle sensing platform would be preferable for many applications, especially for chemical sensing in solution or *in vivo*; however, the coherence properties of NV^- centers in nanodiamonds remain far worse than their bulk counterparts due to increased impurity levels and surface contamination.[516] Colloidal QDs—with far superior control over purity, shape, and surface chemistry—present clear advantages over nanodiamond platforms. For example, electron paramagnetic resonance studies of colloidal, ZnO:Mn^{2+} QDs[335] showed hyperfine coupling between the impurity manganese spins and protons outside the QD (likely those of the capping ligands, which could feasibly be replaced by a functionalized surface for sensing) and reduced dipole−dipole interactions between individual impurity spins that increase coherence times from ∼0.07 to ∼0.9 μs compared to bulk ZnO:Mn^{2+} with the same Zn:Mn ratio. Likewise, the coherent dynamics of donor-bound excitons in ZnSe provide a mechanism to induce and control nuclear spin ensembles.[517] These results foreshadow the suitability of custom-engineered colloidal QDs for quantum sensing applications.

6. ASSEMBLY AND INTEGRATION

Colloidal QDs can be dispersed in solvents and readily integrated on surfaces and in devices using solution-based assembly techniques, such as spin- or dip-coating, drop-casting, doctor-blading, ink- and transfer-printing, and imprinting.[518] Spin-coating in combination with lithography also allows patterning of QD assemblies.[411,519] These solution-based deposition methods have been exploited to integrate colloidal QDs in conventional electronic, optoelectronic, and optical device architectures.[390] Spin-coating dilute QD dispersions has been the most common approach used to separate QDs on the surface for single-particle spectroscopy[245] and to integrate QDs in photonic and plasmonic cavities.[520,521] In this review, we focus on assembly techniques that allow the deterministic positioning of single QDs and the assembly of ordered QD arrays, targets for their integration in optical cavities and in architectures for quantum information processing. The assembly and integration of colloidal QDs is a key advantage of this materials class and stands in contrast to the challenges faced by SLE-QDs that nucleate and grow randomly, giving rise to a dispersion in QD size and therefore properties and to a lack of positional control. SLE-QDs are also limited in their scalability by the nature of their vacuum-based growth.

6.1. Deterministic Assembly of Single QDs

Single-photon sources require the deterministic positioning of single QDs in photonic cavities that serve to enhance, direct, and control the polarization of their emission. Nanomanipulation, patterning, and assembly techniques providing <100 nm positional accuracy have been explored, developed, and, in some cases, commercialized by the scientific community. These techniques commonly use external forces, i.e., mechanical, chemical, optical, electrical, or thermal forces, to control or direct the placement of QDs, and more broadly nanomaterials, on surfaces. Here, we survey these techniques and give examples where they have been applied to position emitters in optical cavities.

6.1.1. Nanomanipulation. Nanomanipulation in the scanning probe microscope takes advantage of the weak interactions between the QDs, and again nanomaterials broadly, and the surface to allow the scan probe tip to mechanically "push" the QD to a desired location.[522] The lateral QD displacement is achieved by controlling the *z*-feedback; i.e., turning off the feedback removes the constant tip-to-QD distance and allows the QD to be pushed, and turning back on the feedback lifts the tip from the QD to stop the movement when it reaches the targeted location. Scanning probe manipulation has been implemented to position QDs in fabricated photonic structures[523−525] or to push a plasmonic NC in proximity to a QD.[526] For example, Figure 13a depicts an

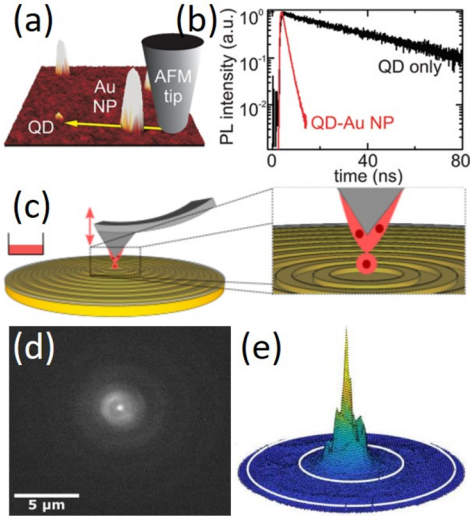

Figure 13. (a) Schematic of the tip from an AFM cantilever pushing a Au NC near a CdSe−ZnS QD and (b) the PL decay from an isolated QD and when the Au NC is proximal.[526] Adapted with permission from ref 526. Copyright 2011 American Chemical Society. (c) Schematic of DPN placement of a colloidal QD liquid ink at the center of a metal-dielectric antenna and (d) a spatially resolved map and (e) back focal plane image of the QD-nanoantenna PL.[528]

atomic force microscope (AFM) cantilever being used to position a Au NC near a CdSe−ZnS core−shell QD. The proximal Au NC significantly reduces the QD PL lifetime and intermittency (Figure 13b). The scanning probe microscope is a serial technique providing control over one QD at a time. Scanning probe arrays are being developed to parallelize the manipulation process.[527]

Dip-pen nanolithography (DPN) builds on the nanometer positional control of the scanning probe microscope to pick up QDs, by inking the tip upon dipping it into a QD dispersion, and placing the QDs, by bringing the "inked" tip down to the surface in the target location.[529] The mechanism for material transport from the tip to the surface depends on the chemical and physical properties of the ink (i.e., (non)-aqueous, (non)-volatile, and

https://dx.doi.org/10.1021/acs.chemrev.0c00831
Chem. Rev. 2021, 121, 3186−3233

the volume and viscosity if the liquid is nonvolatile), the substrate (i.e., the wetting of and chemical affinity for the ink material), and the environmental conditions (i.e., temperature and humidity). Materials systems are broadly classified as either diffusive inks or liquid inks.[530] Upon inking, the solvent of diffusive inks evaporates, leaving the material dried on the tip. In humid environments, a water meniscus condenses spontaneously at the narrow gap between the tip and substrate and allows for material dissolution, diffusion, and capillary assembly on the surface. Liquid inks are nonvolatile, and material transport occurs by fluid flow from the tip to the surface. The amount of material, in this case QDs that are transferred, depends on the amount of ink on the tip (i.e., the concentration of and immersion time in the QD dispersion) and the tip dwell time at the target location. Figure 13c shows a recent demonstration of DPN using a liquid ink to position CdSe−CdSe core−thick-shell QDs at the center of a bullseye metal−dielectric nanoantenna. The integration of the QD in the nanoantenna architecture allows room-temperature, directional emission of single photons (Figure 13d,e) that is advantageous to use lens-free, in free space or to couple to optical fiber.[528] Efforts to parallelize scanning probe manipulation are similarly explored for DPN.[527] Variants such as polymer-pen lithography, in which Si cantilevers are replaced by polymers molded in the shape of tips and in which the transfer of material to the surface occurs via a mechanism akin to microcontact printing, allow scalable, array-based printing.[531]

6.1.2. Template-Directed Assembly. Template-directed assembly marries lithography to define size- and shape-engineered topographical "traps" with assembly, in which capillary forces drive particle deposition at a liquid meniscus into the trap site.[532,533] Optical, e-beam, nanoimprint, or scanning probe lithographies can be used to pattern the traps. The template traps can be concave (e.g., cavities) or convex (e.g., posts) and can be composed of photoresist (which can subsequently be removed), polymers, or an inorganic material (e.g., glass, metal). Template-assisted assembly has been most frequently carried out for aqueous dispersions of spherical and rod-shaped Au and Ag NCs to create large-area and complex assemblies and to study the optical properties of these structures.[533−537] A NC dispersion is placed between a patterned substrate and a glass slide, establishing a water meniscus (Figure 14a). As the slide and the meniscus are translated with respect to the substrate, a long-range evaporation-induced, convective flow field transports the NCs to the meniscus, dominating diffusion and recirculation flows, creating an accumulation of NCs. Capillary forces and local confinement effects of the cavities drive the NCs at the air−water interface into and retain the NCs in the traps. The intricate balance of forces requires control over the temperature and humidity of the environment, the temperature and wettability of the substrate, and the translation speed and distance to the substrate of the glass slide to successfully assemble the NCs.[538]

As many emissive NCs, including QDs, are often dispersed in non-aqueous solvents, a squeegee process has been used to similarly position particles in template sites.[540−542] An elastomer, such as polydimethylsiloxane (PDMS), is cut to form a "wiper", and the wiper is dragged at a shallow angle (e.g., 35°) across the surface, in a method akin to screen printing. As the meniscus is moved across the substrate, the NCs at the interfaces are pushed into the trap sites. While the detailed mechanistics of the squeegee process are not well studied, empirically conditions allow reliable, high-yield assembly. In a

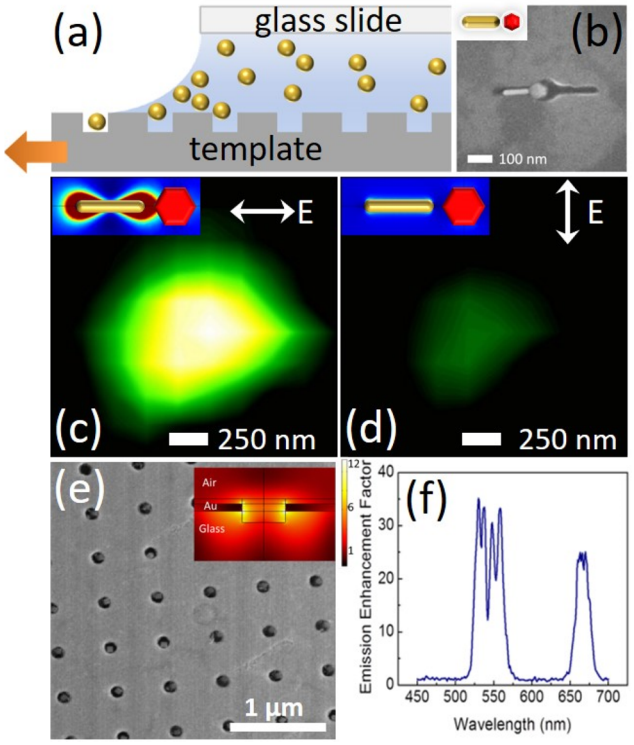

Figure 14. (a) Schematic of template-assisted, capillary assembly of NCs. (b) SEM image of a $NaYF_4$:Er^{3+},Yb^{3+}, hexagonal prismatic, UCNP−Au nanorod assembled heterodimer. Spatially resolved PL maps and (inset) simulated field intensity enhancement maps for single-heterodimers with 977 nm excitation light polarized (c) along and (d) perpendicular to the rod axis.[539] Panels b−d adapted with permission from ref 539. Copyright 2014 American Chemical Society. (e) SEM image of $NaYF_4$:Er^{3+},Yb^{3+} UCNPs assembled in a Au nanohole array and (inset) simulated field intensity enhancement map in one aperture of the nanohole array. (f) The spectrum of the emission enhancement factor for $NaYF_4$:Er^{3+},Yb^{3+} UCNPs assembled in an Au nanohole array.[540] Panels e and f adapted with permission from ref 540. Copyright 2013 American Chemical Society.

conceptually similar and clever approach, 8 nm Au NCs were assembled with high yield in lithographically defined templates.[543] Instead of using a wiper, a hexane dispersion was allowed to spread by climbing against gravity into patterned templates, creating a meniscus and drying front to direct assembly.

Template-assisted capillary and squeegee assembly can be mixed and matched to enable the formation of complex multiparticle structures. Figure 14b shows an example of heterodimers constructed in templates by sequential squeegee assembly of $NaYF_4$:Er^{3+},Yb^{3+} hexagonal prismatic UCNPs from hexane dispersions followed by capillary assembly of Au nanorods dispersed in water.[539] The size and shape of the trap sites are designed so the center could only accept a single nanophosphor and the extended arms would only be filled with the nanorods. The dimensions of the nanorods are selected to spectrally match their localized surface plasmon resonance (LSPR) to the sensitization of the nanophosphor, yielding heterodimers that show enhanced luminescence when the LSPR is excited by light polarized along the rod axis (Figure 14c,d). Template-assisted assembly is a scalable process, enabling the parallel yet deterministic positioning of NCs in traps, with yields of >90% for a single particle in each trap site. For example, Figure 14e shows a Au nanohole array designed to have holes (i.e., trap

https://dx.doi.org/10.1021/acs.chemrev.0c00831
Chem. Rev. 2021, 121, 3186−3233

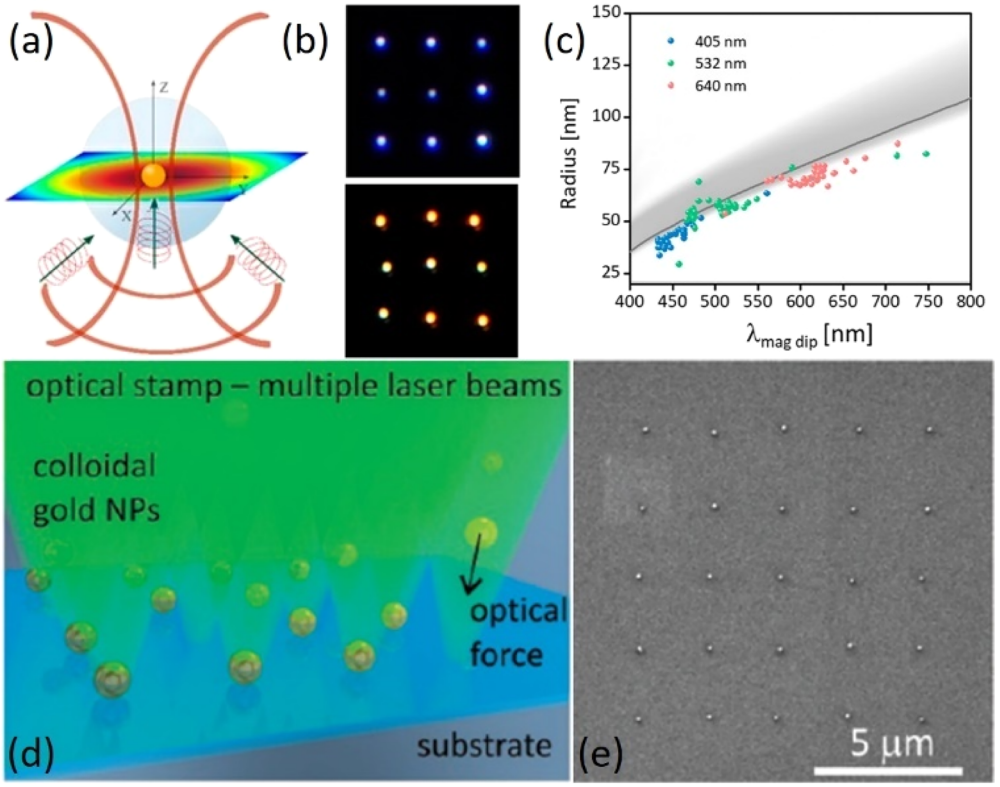

Figure 15. (a) Optical printing using radiation pressure from a laser field to trap and assemble a NC on a surface. (b) The spectrally selective printing of small and large Si NCs with (top) 405 nm and (bottom) 640 nm excitation, following (c) the size-dependent magnetic dipole resonance, in comparison to the (gray) size-dependent maximum radiation pressure for the magnetic resonance.[546] Parts a–c adapted with permission from ref 546. Copyright 2019 American Chemical Society. (d) Schematic of optical force stamping and (e) SEM image of assembled Au NC arrays.[547] Parts d and e adapted with permission from ref 547. Copyright 2011 American Chemical Society.

sites) that are slightly larger in size than that of the UCNPs.[540] The metal nanohole array thickness and the periodicity are selected to create a strong electric field at the trap site when each site is filled with a UCNP and illuminated with light matched to the excitation wavelength of the UCNP. The optical cavity created by the nanohole array substantially enhances the luminescence efficiency of the colloidal UCNPs (Figure 14f).

To date, template-assisted assembly has been demonstrated to deterministically position single NCs that are typically >50 nm in size, but these techniques do allow the extension to <10 nm. Many QDs are <20 nm in size and thus will require patterning of smaller trap sites, which is possible using high-resolution lithographies, but not as routine; studies to understand the effectiveness of capillary and confinement forces, that reduce Brownian motion,[538] to successfully trap these smaller NCs; and efforts to exploit surface chemical methods to add organic ligand and inorganic shells and increase the physical "QD-in-particle" size.

6.1.3. Optical Nanoprinting. Instead of chemical or mechanical forces, optical nanoprinting uses light to direct NC assembly.[544] Optical printing is akin to optical tweezing in that a laser field is used to create optical forces that localize the NCs (Figure 15a). The distinction is in the selection of whether the illumination is spectrally matched to a resonance in the NC. Optical tweezing uses non-resonant illumination to trap particles in the laser field but is too weak to overcome the electrostatic repulsion between a charged NC and the surface. Optical printing uses resonant illumination to strengthen the optical forces to both trap the NCs and exceed NC-surface repulsive interactions and allow van der Waals assembly of NCs on surfaces. Again, most examples of optical printing involve various size and shape plasmonic NCs, which are typically charged to enable their electrostatic stabilization in water.[544,545] Early examples of optical printing reported a limitation in the distances between NCs to ∼300 nm. This is now understood to arise from thermal gradients created by heat dissipation upon resonant excitation. Adding a thermal sink to the substrate, such as a layer of reduced graphene oxide, removes the thermal gradient and allows the printing of closely spaced NCs. The need for resonant excitation also provides spectrally selective printing and, with multicolor illumination, the sequential printing of different NCs based on their optical resonances. Beyond optical printing of plasmonic metal NCs, resonances such as magnetic dipolar resonances in semiconductor NCs also allow their printing. Figure 15b,c shows examples of optical printing of Si NCs varying in size.[546] Adding a spatial light modulator in the excitation path has been used to create multiple beams for parallel printing of NCs, as shown in Figure 15d,e.[547] As optical forces scale with the size of the NC, optical printing has been limited to NCs >25 nm in size.

By selecting the properties of the underlying substrate, optical illumination can create additional local electrical, thermal, and chemical forces to indirectly control the printing of colloidal particles. Other processes have also been demonstrated which allow the assembly of single colloidal QDs. For example, electrostatic assembly takes advantage of the different isoelectric points of metal oxides and SiO_2.[548] By patterning positively charged metal oxide pads on a negatively charged SiO_2 surface, the polarity of the substrate charge is spatially differentiated to allow the selective assembly of negatively charged QDs on the

https://dx.doi.org/10.1021/acs.chemrev.0c00831
Chem. Rev. 2021, 121, 3186–3233

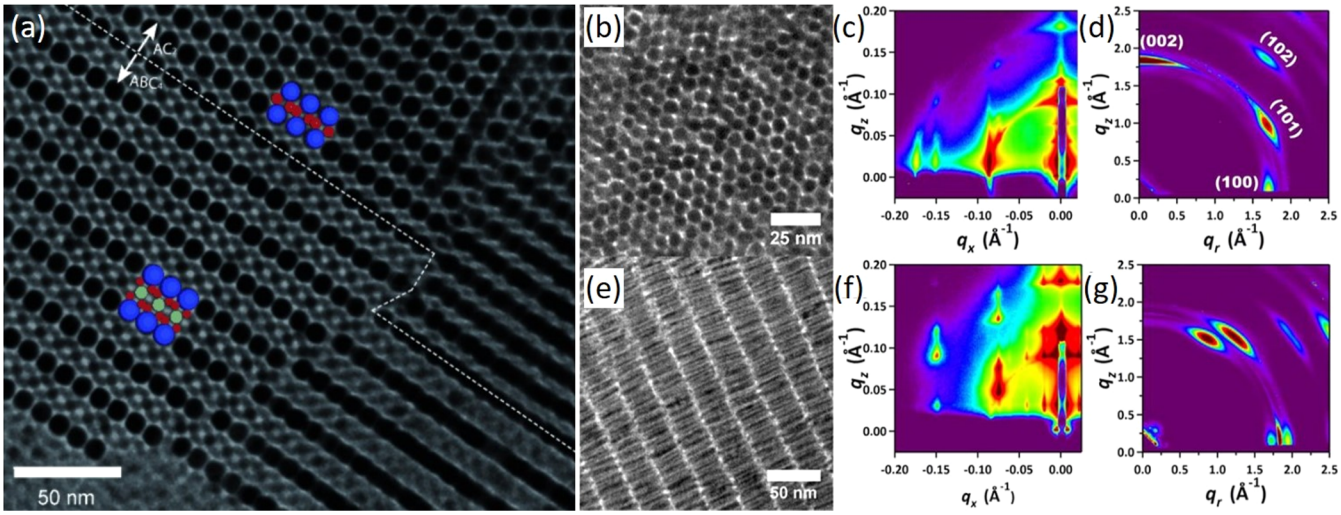

Figure 16. (a) TEM image of the (100) of a ternary superlattice, isostructural with $AlMgB_4$, composed of large PbSe QDs (blue spheres), medium-sized PbSe QDs (green spheres), and small CdSe QDs (red spheres) in epitaxial contact with a binary superlattice, isostructural with AlB_2, composed of PbSe QDs and CdSe QDs.[581] Adapted with permission from ref 581. Copyright 2009 John Wiley and Sons. CdSe/CdS dot-in-rod QDs assembled into smectic B superlattices with parts b and c vertically aligned and parts e−g horizontally aligned lamellae of dot-in-rod QDs.[589] Adapted with permission from ref 589. Copyright 2015 American Chemical Society.

metal-oxide pads. In another example, a microfluidic device was designed to allow electroosmotic pressure to guide the flow of QDs dispersed in photoresist.[549] The photoresist was UV-polymerized to immobilize the QD at its target location.

6.2. Quantum Dot Arrays

Essential to large-scale quantum information processing platforms are the integration and coupling of large numbers of qubits in arrays. Colloidal QDs can be assembled into extended arrays or superlattices, allowing their novel excitonic, charge, and spin-based properties to be captured and engineered for complex, solid-state assemblies. The interactions between QDs can be finely tuned by the length of ligands or thickness of shells (in core−shell QDs) that define the distance between QDs. The spacing is precisely tailorable from ∼25 nm to touching. As interparticle separation decreases, the coupling between QDs increases from weaker dipolar to stronger exchange interactions, and new properties emerge as excitations and carriers become delocalized over multiple QDs.[389] For QDs that host spin qubits, direct dipole−dipole interactions between spins with dipole moments μ_1 and μ_2 scale as $A \sim \mu_1\mu_2/d^3$. Such dipolar interactions can be used to generate entanglement between spin qubits as long as $A > 1/T_2$, where T_2 is the spin coherence time.[26] For electron spins with $\mu_1 \sim \mu_1 \sim \mu_B$, where μ_B is the Bohr magneton, and $T_2 \sim 1$ ms, the maximum distance for coherent coupling is ∼30 nm. The single-nanometer dimensions of host QDs permit assembly of qubits at or below this length scale, where interactions could generate entanglement and permit the realization of complex quantum systems such as spin−lattices.

6.2.1. QD Self-Assembly. Colloidal self-assembly is the phenomenon in which individual (discrete) colloidal particles organize themselves into structures, most commonly with elements of both translational and rotational symmetry, although only rotational symmetry is found in recently identified quasiperiodic NC assemblies.[550] Colloidal crystallization encompasses both natural (e.g., geologic opal formation[550]) and artificial self-assembly processes such as the assembly of amorphous latex and silica particles.[551] To emphasize the presence and importance of both the QDs' internal crystalline lattices and the lattice constituted by the QD centers, the term QD or NC superlattice is often used.[1,389,552,553] QD superlattices can form by simple solvent evaporation to form thin films or by destabilization in a bulk dispersion to create three-dimensional polyhedral assemblies, sometimes distinguished as supercrystals[554−556] or superparticles[556] or mesocrystals when the QD subunits have precise crystallographic registry.[557]

QD self-assembly is a multiscale process requiring uniformity in QD core (or core−shell) size of ±10%, and preferably <7%, in which cores are typically only 1−20 nm in diameter. Surface coordinating ligands add a "softer", more compliant shell of 0.5−5.0 nm to the overall particle dimension. When the cores of the QDs are small compared to the physical extent of the ligand shell, these soft spheres can take on a range of less close-packed symmetries.[558−560]

In superlattices, these QDs are organized on regular lattice sites to form ∼1 μm to >1 mm domains and packed together to create "polycrystalline films" extending >1 cm laterally in the best-developed systems. The interactions that drive QD assembly are typically noncovalent (e.g., van der Waals, hydrogen bonding, or hydrophobic forces) or specific ligand attractions (e.g., DNA) or entropic forces[1,561−565] that contribute to the overall interparticle potential.[566] Self-assembly can be triggered by concentration changes, temperature changes, evaporative flows, or magnetic, electric, centrifugal, or gravitational fields.[558] Rapid destabilization often results in uncontrolled aggregation and disordered low-density structures.[558,567] Best practices generally involve some degree of reversibility in the particle attachment to the growing superlattice. However, irreversible linking may follow the self-assembly stage.

The most straightforward route to form QD superlattices exploits the spontaneous formation of regular arrays (superlattices) during the evaporation of dispersions, as first shown for nearly monodisperse II−VI QDs.[552] Evaporation-based assembly can be implemented by allowing a dispersion to dry over a period from minutes to hours in an open vessel containing a semisubmerged substrate.[568] Alternately, the more rapid, seconds to minutes evaporation processes of drop-casting, in

https://dx.doi.org/10.1021/acs.chemrev.0c00831
Chem. Rev. 2021, 121, 3186−3233

which a few microliters of dispersion is deposited onto a solid substrate[1,394,552] or an air−liquid interface,[569] yield superlattice thin films or membranes, respectively. QDs have also been deposited on a variety of substrates using Langmuir−Blodgett techniques.[570,571]

Destabilization-based assembly reduces the repulsive interactions between particles by addition of a non-solvent or controlled evaporation of a good solvent from a suitable solvent/non-solvent mix. A variant exploits the slow interdiffusion of largely miscible liquids over several days to induce the controlled formation of faceted QD superlattices,[572,573] analogous to macromolecular or protein crystallization.[574] The ligand's favorable interaction with the solvent provides steric repulsion.[575−579]

Moderate heating during evaporation can facilitate assembly because thermal energy enhances QD mobility and allows annealing of the growing structures;[580] however, temperatures high enough to decompose or desorb ligands must be avoided.[568]

Controlled evaporation of bidisperse colloids with different size but precisely controlled size ratios and relative concentrations has yielded a wide range of structural types,[314] including binary and ternary superlattices (Figure 16a),[581] allowing great flexibility in the design of the physical properties of the resulting artificial solids.[582,583] Binary and ternary superlattices can pack with a density that outcompetes that of superlattices from each of the separated components.[314,584−588] Rod- and platelet-shaped QDs can self-assemble into superlattices with their lower symmetry imparting a degree of liquid crystal ordering (Figure 16b−g).[589] In addition to the regularity of the QD spacing, there is a preferred texture of crystal alignment from particle to particle with smectic, for rod,[590−592] and discotic, for plate, assemblies.[593] Semiconductor nanoplates of regular size and shape, including discs, hexagons, and triangular plates, have been shown to undergo self-assembly upon deposition.[594−596]

6.2.2. Ligand Engineering of QD Assemblies. The chemical nature, dimensions, and density of the surface coordinating ligands play an important role in controlling many aspects of QDs, and more broadly NC superlattices.[597−599] The ligands are often described by the softness ligand shell $S = {}^{L}/_{R}$, where L is the ligand length and R is the inorganic QD core (or core−shell) radius. Although early studies explored varying ligand chain length (and thereby shell softness) in QD superlattice assembly,[1,552] the influence of softness was investigated in detail recently.[559,560,597,600]

Solvothermal QD synthesis typically employs long-chain, organic alkyl amines, phosphines, or thiols as stabilizing ligands. These molecules enforce an ∼1−2 nm separation with a precision of ∼0.1 nm between neighboring QDs, depending on the chain length and steric bulk. However, often it is desirable to adjust the interparticle spacing that would be established by the ligands in a QD superlattice. There are some examples of directly synthesizing the QDs in the presence of other ligands, such as the polycatenar ligands;[601] however, it is more common to replace the ligands used in synthesis by exchange with ligands that are shorter or longer or that add or alter functionality.[602] The QD community has established a large ligand library and processes to exchange the ligands used in synthesis for ligand compositions that allow tuning of QD structure and function.[597]

The ligand exchange process can be carried out while the QDs are dispersed in solvent and is known as "solution-exchange", or after the QDs are assembled into superlattices, referred to as "solid-state" exchange. In either case, the QD dispersion or the QD superlattice is exposed to a solution of the new ligand. For solution-exchange, the QDs are typically washed via dispersion in solvent and centrifugation, akin to the process used in purification (see section 3.2.4), whereas, for solid-state exchange, the QD superlattice is washed by cycles of rinsing in fresh solvent to remove unbound ligand. There are pros and cons to each approach, as solution-exchange is more challenging as QDs bearing the new ligand must be able to sterically or electrostatically stabilize the QD in solvents for assembly but advantageously allows the formation of dense QD assemblies.[389] Solid-exchange allows for the use of a wide library of ligand chemistries, but changes in ligand volume can create strain and voids in the QD superlattice.

Longer spacings up to ∼15 nm interparticle spacings have been realized by use of DNA,[603] dendrimeric,[604] or polycatenar ligands.[601] These long ligands, and their increased softness, provide flexibility to assemble QD superlattices with complex structures. For electronic and optoelectronic devices, shorter organic (e.g., alkyl amines and thiols) and compact inorganic (e.g., hydrazine, chalcogenodimetallates, halometallates, chalcogenides, hydroxides, halides, and pseudohalides) ligands have been introduced to reduce interparticle spacing to ≲0.5 nm in order to strengthen electronic coupling, and therefore charge transport between QDs,[362,389] and to create surface dipoles, and thus tune the absolute QD energy levels and band alignment.[46,605]

7. SUMMARY AND OUTLOOK

Colloidal QDs pack versatile functionality prerequisite to constructing photon and spin qubits at the scale of individual semiconductor crystals, <100 nm, and typically 1−20 nm in diameter. Quantum states can be encoded as excitons delocalized across their volume or in charge and spin states localized at defects or dopants within their core. Synthetic methods now allow near-atomic-scale precision in tailoring the size and shape of QDs from all major semiconductor compositions, precise engineering of semiconductor heterostructures, and controlled introduction of defects and dopants. Extensive spectroscopic measurements and theoretical and computational methods have uncovered the quantum mechanics that govern QDs' photonic properties, i.e., the energy and time scale of optical absorption and emission, which lay the foundations for understanding their quantum photonic properties, important to controlling superposition, entanglement, and quantum measurement. The coordinated exploration of QD synthesis, structure, spectroscopic, and theoretical investigation in the community has and continues to support the development of QDs as bright, stable optical emitters. These QDs can be synthesized at scales that have allowed their commercial adoption as optical materials in display technologies. As colloids, directed- and self-assembly techniques enable deterministic positioning of single QDs on surfaces and integration in optical cavities with evidence of ≲10 nm precision and organization into ordered QD arrays with subnanometer precision in spacing defined by the selection of surface ligands that mediate inter-QD interactions.

The time is right to harness the exquisite design of colloidal QDs as platforms for quantum information science. With precise control over composition and structure and the advantages of quantum confinement to engineer the spatial distribution, energy, and interactions between charge and spin states, a variety of photon and spin qubits can be realized. Their small size presents opportunities for device integration and complex

https://dx.doi.org/10.1021/acs.chemrev.0c00831
Chem. Rev. 2021, 121, 3186−3233

assembly, while the availability of large-scale production indicates their viability for commercial applications. Looking toward this aspiration, we highlight a few areas where the community is already exploring QDs as quantum optical materials and key directions for future research that can facilitate the realization of robust, optically addressable qubits.

- *Single-photon emission*: A QD's discrete, core electron and hole states constitute the prerequisite two-level electronic structure for single-photon emission. Single-QD spectroscopies have reported single-photon excitonic emission for various colloidal QD sizes, shapes, and compositions, including observations of spherical II−VI and cubic metal-halide perovskite QDs with near-perfect single-photon purity. An important difference in these two materials systems is the role of the QD surface. In archetypical II−VI QDs, surface electronic states create non-radiative pathways for recombination via traps and Auger autoionization; however, the problem can be solved using well-established growth methods for core−shell QD heterostructures. By engineering the composition and thickness of the shell, guided by wave function engineering to reduce the overlap of carriers, this approach has nearly eliminated the Auger process and the associated PL intermittency, for low excitation intensities. For metal-halide perovskite QDs, in contrast, surface states are electronically shallow and ineffective recombination pathways in core-only QDs.

  Studies of these example QDs are uncovering the design rules for bright single-photon emitters, i.e., the role of the core and surface on the electronic structure that governs the brightness and optical coherence of single-photon emission, described in more detail next. These design rules are guiding the development of color-tunable, single-photon emitters in the ultraviolet, visible, and infrared spectrum from the broader colloidal QD library for the wide range of quantum information science applications. The most studied examples are Cd-based II−VI QDs and Pb-based metal-halide perovskite QDs. Demonstrations of single-photon emission from Cd- and Pb-free compositions, such as InP−ZnSe core−shell QDs,[606] are important in particular for life-science applications. Unlike the water solubility of metal-halide perovskites, protocols for ligand engineering of core−shell II−VI, III−V, IV−VI, and I−III−VI_2 QDs are well established and have allowed their use as compatible, fluorescent probes for biological imaging, labeling, and tracking.[607,608]

- *Optical coherence*: For the purpose of generating indistinguishable single photons, the two examples of II−VI core−shell QDs and metal-halide perovskite QDs provide an interesting comparison. The shorter exciton lifetime, even at room temperature, of metal-halide perovskite QDs advantageously makes for brighter emission than that for spherical II−VI QDs. At cryogenic temperatures, these systems show similar ZPL line widths and comparable optical coherence times, $T_2 \sim 100$ ps. However, the fine structure in the lowest-energy state creates a 100-fold disparity in their radiative lifetimes, T_1. Spherical II−VI QDs have an optically forbidden, low-energy, dark excitonic state and thus a relatively long $T_1 >$ 10 ns. In contrast, $CsPbBr_3$ QDs have low-energy optically bright states and much faster radiative lifetimes of $T_1 \sim 210$ ps, closer to T_2.[249] In II−VI QDs, dephasing is dominated by phonon-assisted, spin-flip transitions between bright and dark states within the fine structure manifold. For applications that require longer T_2, and thus longer T_1, engineering the electronic fine structure by tailoring the size, crystal structure, shape, composition, and internal structure can alter the energy separation and order of bright and dark states in the fine structure, promising a route to exploit the sophistication of QD design and to explore the manipulation of optical coherence times. In metal-halide perovskite QDs, ligands at the QD surface have been suggested as a possible source of phonon dephasing.[249] To create indistinguishable photons and to limit coupling to phonons and prevent electronic fluctuations that cause noise, the architecture of core−shell QD heterostructures may provide a route to remove the interactions with vibrational modes of the ligands and to electrostatically shield states delocalized across or in defect states within the QD core.
- *Oscillator strength*: Excitonic QD states have large optical dipole moments of ∼50 D,[609] as the oscillator strength of bulk semiconductors is concentrated in the QD core. The large optical dipole moment naturally leads to a large coupling strength with photonic structures, e.g., making it easier to achieve strong coupling with an optical cavity. For QDs hosting defects and dopants, the oscillator strength of the defect transitions depends on their electronic structure. Defects with ground and excited states composed of sp orbitals with dipole-allowed transitions generally have dipole moments comparable to single molecules at ∼1−10 D, whereas transitions arising from d or f orbitals from TM and RM dopants, respectively, generally have much smaller optical dipole moments of 0.001−0.1 D, consistent with their longer optical lifetimes. These considerations raise the possibility of intentionally coupling the strong optical absorption or emission properties of the host QD to the spin or optical properties of a defect in the core, which may have a weaker intrinsic oscillator strength. Charge or energy transfer between the QD and defect states could be used, for example, to improve the optical excitation or readout efficiency of defects utilized as spin qubits or sensors.
- *Spin coherence*: The spin coherence times of excitonic states in QDs are generally short, ∼100 ps. However, QDs can serve as wide-band-gap hosts for QPDs, with low spin−orbit coupling and dilute nuclear spin concentrations that protect the defects' spin coherence. The exploration of defects and dopants as spin qubits in colloidal QDs is still in early stages. However, a great deal is known about defect complexes and TM and RE dopants in the bulk analogues of many classic colloidal QD materials. QDs may provide a convenient platform to probe and identify defects and dopants at the individual level, since they can be spatially isolated in individual QDs even at relatively high (i.e., ∼100 ppm) impurity levels. Several pioneering studies have already shown the ability to use exchange coupling between spin levels of TM dopants such as Mn^{2+} with QD excitonic states for spin initialization and readout. This effect is especially promising for interfacing with QPDs that have internal transitions which are weak or energetically removed from bands that are useful for telecommunications or biological

https://dx.doi.org/10.1021/acs.chemrev.0c00831
Chem. Rev. 2021, 121, 3186−3233

sensing. Adaptation of these approaches, through collaborations between experts in theory, synthesis, and quantum measurements, can likely provide a versatile set of new spin qubit architectures.

- *Spin−photon interfaces*: Ultimately, many of the most exciting future applications in quantum information science—including long-distance quantum communication and scalable, distributed quantum computing—will be enabled by robust, efficient quantum interfaces between long-lived, controllable quantum registers (e.g., spin states) and coherent photonic channels. A spin−photon interface is the essence of a quantum repeater, which facilitates the distribution and control of entanglement over arbitrary distances. The realization of spin−photon interfaces demands control over optical coherence, spin coherence, and efficient conditional interactions between the spin and photonic degrees of freedom. Practical applications will likely require integration with optical cavities and integrated photonic devices to control the flow of photons between spatially separated nodes. For all of the reasons listed earlier, colloidal QDs are promising platforms for building quantum repeaters and other systems based on spin−photon interfaces. In particular, they feature strong, tunable optical properties, are ideal hosts for spin qubits, and can be reproducibly synthesized and integrated with photonic structures. Research in pursuit of this goal can focus on the identification of stable spin qubits with long coherence times (this will likely include individual nuclear spins coupled to an optically addressable electron-spin qubit) along with optimization of optical coherence and spin-dependent transitions that can be used to transfer quantum information from spins to photons and vice versa.
- *Scalable fabrication*: One of the clear advantages of colloidal QDs is their scalable synthesis and assembly. QD inks are being commercially produced at the tens of tons scale per year for display technologies. In research, nanomanipulation, colloidal assembly, and optical printing techniques are enabling the deterministic assembly of individual particles with tens of nanometers precision, setting the stage for the integration of QD emitters in optical cavities and device architectures, created by metallic, dielectric, and magnetic materials via fabrication and multiparticle assembly, to control the behavior of exciton, charge, and spin states at will. Akin to colloidal crystallization, self-assembly of QD superlattices enables single-nanometer precision in interparticle spacing and the organization of single-particle and multiparticle assemblies, a platform commensurate with the definition of arrays that entangle quantum coherent spin states.

AUTHOR INFORMATION

Corresponding Authors

Cherie R. Kagan − *Department of Electrical and Systems Engineering, Department of Materials Science and Engineering, and Department of Chemistry, University of Pennsylvania, Philadelphia, Pennsylvania 19104, United States;* orcid.org/0000-0001-6540-2009; Email: kagan@seas.upenn.edu

Lee C. Bassett − *Department of Electrical and Systems Engineering, University of Pennsylvania, Philadelphia, Pennsylvania 19104, United States;* orcid.org/0000-0001-8729-1530; Email: lbassett@seas.upenn.edu

Christopher B. Murray − *Department of Materials Science and Engineering and Department of Chemistry, University of Pennsylvania, Philadelphia, Pennsylvania 19104, United States*; Email: cbmurray@sas.upenn.edu

Author

Sarah M. Thompson − *Department of Electrical and Systems Engineering, University of Pennsylvania, Philadelphia, Pennsylvania 19104, United States;* orcid.org/0000-0002-1870-0633

Complete contact information is available at: https://pubs.acs.org/10.1021/acs.chemrev.0c00831

Notes

The authors declare no competing financial interest.

Biographies

Cherie R. Kagan is the Stephen J. Angello Professor of Electrical and Systems Engineering, Materials Science and Engineering, and Chemistry at the University of Pennsylvania. Her group studies the chemical and physical properties of nanostructured materials and their electronic, optoelectronic, optical, and sensing devices. She earned her PhD in Materials Science and Engineering from MIT (1996) and was a postdoc at Bell Laboratories. She worked for 8 years at IBM's T.J. Watson Research Center before moving to Penn in 2007. She is an Associate Editor for *ACS Nano* and is currently Vice President of the Materials Research Society.

Lee C. Bassett is an Associate Professor of Electrical & Systems Engineering at the University of Pennsylvania. He is responsible for the Quantum Engineering Laboratory, which studies quantum dynamics in nanoscale devices and materials using optics and electronics. Prior to arriving at Penn, he earned a MASt in Mathematics (2005) and PhD in Physics (2009) from the University of Cambridge as a Marshall Scholar and NSF Graduate Research Fellow, and he was a postdoc at the University of California, Santa Barbara.

Christopher B. Murray is the Richard Perry University Professor of Chemistry and Materials Science at the University of Pennsylvania. His group focuses on the preparation and assembly, characterization, and integration of nanomaterials. Chris earned his PhD in Chemistry from MIT (1995) and became a Research Staff Member at IBM's T.J. Watson Research Center managing the Nanoscale Materials and Devices Department from 2000 until moving to Penn in 2007. Chris is a member of the National Academy of Engineering and contributes to the broader scientific community in nanoscience and engineering by serving on numerous advisory boards for national and international scientific centers, journals, conferences, and professional organizations.

Sarah M. Thompson is a PhD student at the University of Pennsylvania. She studies photoluminescent point defects in semiconductors with the goal of harnessing new materials systems for spin−light quantum interfaces, particularly doped colloidal nanocrystals. She received her BS in Electrical Engineering from Columbia University in 2018.

ACKNOWLEDGMENTS

C.R.K., L.C.B., and C.B.M. are grateful for support from the NSF through the University of Pennsylvania Materials Research Science and Engineering Center (MRSEC) under Award No. DMR-1720530. S.M.T. acknowledges support from the National Science Foundation Graduate Research Fellowship under Grant No. DGE-1845298.

REFERENCES

(1) Murray, C. B.; Kagan, C. R.; Bawendi, M. G. Synthesis and Characterization of Monodisperse Nanocrystals and Close-Packed Nanocrystal Assemblies. *Annu. Rev. Mater. Sci.* **2000**, *30*, 545−610.

(2) Smyder, J. A.; Krauss, T. D. Coming Attractions for Semiconductor Quantum Dots. *Mater. Today* **2011**, *14*, 382−387.

(3) Nirmal, M.; Brus, L. Luminescence Photophysics in Semiconductor Nanocrystals. *Acc. Chem. Res.* **1999**, *32*, 407−414.

(4) Kairdolf, B. A.; Smith, A. M.; Stokes, T. H.; Wang, M. D.; Young, A. N.; Nie, S. Semiconductor Quantum Dots for Bioimaging and Biodiagnostic Applications. *Annu. Rev. Anal. Chem.* **2013**, *6*, 143−162.

(5) Jang, E.; Jun, S.; Jang, H.; Lim, J.; Kim, B.; Kim, Y. White-Light-Emitting Diodes with Quantum Dot Color Converters for Display Backlights. *Adv. Mater.* **2010**, *22*, 3076−3080.

(6) Panfil, Y. E.; Oded, M.; Banin, U. Colloidal Quantum Nanostructures: Emerging Materials for Display Applications. *Angew. Chem., Int. Ed.* **2018**, *57*, 4274−4295.

(7) Kagan, C. R.; Lifshitz, E.; Sargent, E. H.; Talapin, D. V. Building Devices from Colloidal Quantum Dots. *Science* **2016**, *353*, No. aac5523.

(8) DiVincenzo, D. P. The Physical Implementation of Quantum Computation. *Fortschr. Phys.* **2000**, *48*, 771−783.

(9) Bruzewicz, C. D.; Chiaverini, J.; McConnell, R.; Sage, J. M. Trapped-Ion Quantum Computing: Progress and Challenges. *Appl. Phys. Rev.* **2019**, *6*, 021314.

(10) Krantz, P.; Kjaergaard, M.; Yan, F.; Orlando, T. P.; Gustavsson, S.; Oliver, W. D. A Quantum Engineer's Guide to Superconducting Qubits. *Appl. Phys. Rev.* **2019**, *6*, 021318.

(11) Zwanenburg, F. A.; Dzurak, A. S.; Morello, A.; Simmons, M. Y.; Hollenberg, L. C. L.; Klimeck, G.; Rogge, S.; Coppersmith, S. N.; Eriksson, M. A. Silicon Quantum Electronics. *Rev. Mod. Phys.* **2013**, *85*, 961−1019.

(12) Wang, J.; Sciarrino, F.; Laing, A.; Thompson, M. G. Integrated Photonic Quantum Technologies. *Nat. Photonics* **2020**, *14*, 273−284.

(13) Bassett, L. C.; Alkauskas, A.; Exarhos, A. L.; Fu, K.-M. C. Quantum Defects by Design. *Nanophotonics* **2019**, *8*, 1867−1888.

(14) Awschalom, D. D.; Bassett, L. C.; Dzurak, A. S.; Hu, E. L.; Petta, J. R. Quantum Spintronics: Engineering and Manipulating Atom-like Spins in Semiconductors. *Science* **2013**, *339*, 1174−1179.

(15) Awschalom, D. D.; Hanson, R.; Wrachtrup, J.; Zhou, B. B. Quantum Technologies with Optically Interfaced Solid-State Spins. *Nat. Photonics* **2018**, *12*, 516−527.

(16) Atatüre, M.; Englund, D.; Vamivakas, N.; Lee, S.-Y.; Wrachtrup, J. Material Platforms for Spin-Based Photonic Quantum Technologies. *Nat. Rev. Mater.* **2018**, *3*, 38−51.

(17) Aharonovich, I.; Englund, D.; Toth, M. Solid-State Single-Photon Emitters. *Nat. Photonics* **2016**, *10*, 631−641.

(18) Senellart, P.; Solomon, G.; White, A. High-Performance Semiconductor Quantum-Dot Single-Photon Sources. *Nat. Nanotechnol.* **2017**, *12*, 1026−1039.

(19) Gottesman, D.; Chuang, I. L. Demonstrating the Viability of Universal Quantum Computation Using Teleportation and Single-Qubit Operations. *Nature* **1999**, *402*, 390−393.

(20) Knill, E.; Laflamme, R.; Milburn, G. J. A Scheme for Efficient Quantum Computation with Linear Optics. *Nature* **2001**, *409*, 46−52.

(21) Aspuru-Guzik, A.; Walther, P. Photonic Quantum Simulators. *Nat. Phys.* **2012**, *8*, 285−291.

(22) Aaronson, S.; Arkhipov, A. The Computational Complexity of Linear Optics. In *Proceedings of the 43rd annual ACM symposium on Theory of computing - STOC '11*; ACM Press: New York, 2011; p 333.

(23) Gao, W. B.; Imamoglu, A.; Bernien, H.; Hanson, R. Coherent Manipulation, Measurement and Entanglement of Individual Solid-State Spins Using Optical Fields. *Nat. Photonics* **2015**, *9*, 363−373.

(24) Lodahl, P.; Mahmoodian, S.; Stobbe, S. Interfacing Single Photons and Single Quantum Dots with Photonic Nanostructures. *Rev. Mod. Phys.* **2015**, *87*, 347−400.

(25) Degen, C. L.; Reinhard, F.; Cappellaro, P. Quantum Sensing. *Rev. Mod. Phys.* **2017**, *89*, 035002.

(26) Dolde, F.; Jakobi, I.; Naydenov, B.; Zhao, N.; Pezzagna, S.; Trautmann, C.; Meijer, J.; Neumann, P.; Jelezko, F.; Wrachtrup, J. Room-Temperature Entanglement between Single Defect Spins in Diamond. *Nat. Phys.* **2013**, *9*, 139−143.

(27) Leonard, D.; Krishnamurthy, M.; Reaves, C. M.; Denbaars, S. P.; Petroff, P. M. Direct Formation of Quantum-sized Dots from Uniform Coherent Islands of InGaAs on GaAs Surfaces. *Appl. Phys. Lett.* **1993**, *63*, 3203−3205.

(28) Goldstein, L.; Glas, F.; Marzin, J. Y.; Charasse, M. N.; Le Roux, G. Growth by Molecular Beam Epitaxy and Characterization of InAs/GaAs Strained-layer Superlattices. *Appl. Phys. Lett.* **1985**, *47*, 1099−1101.

(29) Loss, D.; DiVincenzo, D. P. Quantum Computation with Quantum Dots. *Phys. Rev. A: At., Mol., Opt. Phys.* **1998**, *57*, 120−126.

(30) Vandersypen, L. M. K.; Bluhm, H.; Clarke, J. S.; Dzurak, A. S.; Ishihara, R.; Morello, A.; Reilly, D. J.; Schreiber, L. R.; Veldhorst, M. Interfacing Spin Qubits in Quantum Dots and Donors—Hot, Dense, and Coherent. *npj Quantum Inf.* **2017**, *3*, 34.

(31) Hanson, R.; Kouwenhoven, L. P.; Petta, J. R.; Tarucha, S.; Vandersypen, L. M. K. Spins in Few-Electron Quantum Dots. *Rev. Mod. Phys.* **2007**, *79*, 1217−1265.

(32) Alivisatos, A. P. Semiconductor Clusters, Nanocrystals, and Quantum Dots. *Science (Washington, DC, U. S.)* **1996**, *271*, 933−937.

(33) Efros, A. L.; Rosen, M. The Electronic Structure of Semiconductor Nanocrystals. *Annu. Rev. Mater. Sci.* **2000**, *30*, 475−521.

(34) Bawendi, M. G.; Steigerwald, M. L.; Brus, L. E. The Quantum Mechanics of Larger Semiconductor Clusters ("Quantum Dots"). *Annu. Rev. Phys. Chem.* **1990**, *41*, 477−496.

(35) Banin, U.; Lee, C. J.; Guzelian, A. A.; Kadavanich, A. V.; Alivisatos, A. P.; Jaskolski, W.; Bryant, G. W.; Efros, A. L.; Rosen, M. Size-Dependent Electronic Level Structure of InAs Nanocrystal Quantum Dots: Test of Multiband Effective Mass Theory. *J. Chem. Phys.* **1998**, *109*, 2306−2309.

(36) Norris, D. J.; Bawendi, M. G. Measurement and Assignment of the Size-Dependent Optical Spectrum in CdSe Quantum Dots. *Phys. Rev. B: Condens. Matter Mater. Phys.* **1996**, *53*, 16338−16346.

(37) Ekimov, A. I.; Kudryavtsev, I. A.; Efros, A. L.; Yazeva, T. V.; Hache, F.; Schanne-Klein, M. C.; Rodina, A. V.; Ricard, D.; Flytzanis, C. Absorption and Intensity-Dependent Photoluminescence Measurements on CdSe Quantum Dots: Assignment of the First Electronic Transitions. *J. Opt. Soc. Am. B* **1993**, *10*, 100.

(38) Brus, L. E. Electron-Electron and Electron-hole Interactions in Small Semiconductor Crystallites: The Size Dependence of the Lowest Excited Electronic State. *J. Chem. Phys.* **1984**, *80*, 4403−4409.

(39) Harrison, M. T.; Kershaw, S. V.; Burt, M. G.; Rogach, A. L.; Kornowski, A.; Eychmüller, A.; Weller, H. Colloidal Nanocrystals for Telecommunications. Complete Coverage of the Low-Loss Fiber Windows by Mercury Telluride Quantum Dot. *Pure Appl. Chem.* **2000**, *72*, 295−307.

(40) Even, J.; Pedesseau, L.; Dupertuis, M.-A.; Jancu, J.-M.; Katan, C. Electronic Model for Self-Assembled Hybrid Organic/Perovskite Semiconductors: Reverse Band Edge Electronic States Ordering and Spin-Orbit Coupling. *Phys. Rev. B: Condens. Matter Mater. Phys.* **2012**, *86*, 205301.

(41) Boles, M. A.; Ling, D.; Hyeon, T.; Talapin, D. V. The Surface Science of Nanocrystals. *Nat. Mater.* **2016**, *15*, 141−153.

(42) Owen, J. Nanocrystal Structure. The Coordination Chemistry of Nanocrystal Surfaces. *Science* **2015**, *347*, 615−616.

(43) Kortan, A. R.; Hull, R.; Opila, R. L.; Bawendi, M. G.; Steigerwald, M. L.; Carroll, P. J.; Brus, L. E. Nucleation and Growth of CdSe on ZnS Quantum Crystallite Seeds, and Vice Versa, in Inverse Micelle Media. *J. Am. Chem. Soc.* **1990**, *112*, 1327−1332.

(44) Danek, M.; Jensen, K. F.; Murray, C. B.; Bawendi, M. G. Synthesis of Luminescent Thin-Film CdSe/ZnSe Quantum Dot Composites Using CdSe Quantum Dots Passivated with an Overlayer of ZnSe. *Chem. Mater.* **1996**, *8*, 173−180.

(45) Hines, M. A.; Guyot-Sionnest, P. Synthesis and Characterization of Strongly Luminescing ZnS-Capped CdSe Nanocrystals. *J. Phys. Chem.* **1996**, *100*, 468−471.

(46) Brown, P. R.; Kim, D.; Lunt, R. R.; Zhao, N.; Bawendi, M. G.; Grossman, J. C.; Bulović, V. Energy Level Modification in Lead Sulfide

https://dx.doi.org/10.1021/acs.chemrev.0c00831
Chem. Rev. 2021, 121, 3186−3233

Quantum Dot Thin Films through Ligand Exchange. *ACS Nano* **2014**, *8*, 5863−5872.
(47) Siaj, M.; Johnson, A. C.; Taylor, J. M.; Laird, E. A.; Yacoby, A.; Lukin, M. D.; Marcus, C. M.; Hanson, M. P.; Gossard, A. C. Creating, Varying, and Growing Single-Site Molecular Contacts. *Science (Washington, DC, U. S.)* **2005**, *309*, 588−590.
(48) Hanson, R.; van Beveren, L. H. W.; Vink, I. T.; Elzerman, J. M.; Naber, W. J. M.; Koppens, F. H. L.; Kouwenhoven, L. P.; Vandersypen, L. M. K. Single-Shot Readout of Electron Spin States in a Quantum Dot Using Spin-Dependent Tunnel Rates. *Phys. Rev. Lett.* **2005**, *94*, 196802.
(49) Tersoff, J.; Teichert, C.; Lagally, M. G. Self-Organization in Growth of Quantum Dot Superlattices. *Phys. Rev. Lett.* **1996**, *76*, 1675−1678.
(50) Ishikawa, T.; Nishimura, T.; Kohmoto, S.; Asakawa, K. Site-Controlled InAs Single Quantum-Dot Structures on GaAs Surfaces Patterned by *in Situ* Electron-Beam Lithography. *Appl. Phys. Lett.* **2000**, *76*, 167−169.
(51) Wang, Y. R.; Han, I. S.; Jin, C.-Y.; Hopkinson, M. Precise Arrays of Epitaxial Quantum Dots Nucleated by In Situ Laser Interference for Quantum Information Technology Applications. *ACS Appl. Nano Mater.* **2020**, *3*, 4739−4746.
(52) Dongre, S.; Paul, S.; Mondal, S.; Panda, D.; Shriram, S. R.; Mantri, M. R.; Gazi, S. A.; Das, D.; Kumar, R.; Tongbram, B.; Chakrabarti, S. Optimization of Vertical Strain Coupling in InAs/GaAs p-i-p Quantum Dot Infrared Photodetectors with Applied Growth Strategy. *J. Lumin.* **2020**, *226*, 117499.
(53) Yamaguchi, K.; Yujobo, K.; Kaizu, T. Stranski-Krastanov Growth of InAs Quantum Dots with Narrow Size Distribution. *Jpn. J. Appl. Phys.* **2000**, *39*, L1245−L1248.
(54) Atkinson, P.; Schmidt, O. G.; Bremner, S. P.; Ritchie, D. A. Formation and Ordering of Epitaxial Quantum Dots. *C. R. Phys.* **2008**, *9*, 788−803.
(55) Gresback, R.; Hue, R.; Gladfelter, W. L.; Kortshagen, U. Combined Plasma Gas-Phase Synthesis and Colloidal Processing of InP/ZnS Core/Shell Nanocrystals. *Nanoscale Res. Lett.* **2011**, *6*, 68.
(56) Kortshagen, U. R.; Sankaran, R. M.; Pereira, R. N.; Girshick, S. L.; Wu, J. J.; Aydil, E. S. Nonthermal Plasma Synthesis of Nanocrystals: Fundamental Principles, Materials, and Applications. *Chem. Rev.* **2016**, *116*, 11061−11127.
(57) Kruis, F. E.; Fissan, H.; Peled, A. Synthesis of Nanoparticles in the Gas Phase for Electronic, Optical and Magnetic Applications—a Review. *J. Aerosol Sci.* **1998**, *29*, 511−535.
(58) Rossetti, R.; Ellison, J. L.; Gibson, J. M.; Brus, L. E. Size Effects in the Excited Electronic States of Small Colloidal CdS Crystallites. *J. Chem. Phys.* **1984**, *80*, 4464−4469.
(59) Henglein, A. Photo-Degradation and Fluorescence of Colloidal-Cadmium Sulfide in Aqueous Solution. *Berichte der Bunsengesellschaft für Phys. Chemie* **1982**, *86*, 301−305.
(60) Fojtik, A.; Weller, H.; Koch, U.; Henglein, A. Photo-Chemistry of Colloidal Metal Sulfides 8. Photo-Physics of Extremely Small CdS Particles: Q-State CdS and Magic Agglomeration Numbers. *Berichte der Bunsengesellschaft für Phys. Chemie* **1984**, *88*, 969−977.
(61) Meyer, M.; Wallberg, C.; Kurihara, K.; Fendler, J. H. Photosensitized Charge Separation and Hydrogen Production in Reversed Micelle Entrapped Platinized Colloidal Cadmium Sulphide. *J. Chem. Soc., Chem. Commun.* **1984**, No. 2, 90.
(62) Howe, A. M. Some Aspects of Colloids in Photography. *Curr. Opin. Colloid Interface Sci.* **2000**, *5*, 288−300.
(63) Steigerwald, M. L.; Alivisatos, A. P.; Gibson, J. M.; Harris, T. D.; Kortan, R.; Muller, A. J.; Thayer, A. M.; Duncan, T. M.; Douglass, D. C.; Brus, L. E. Surface Derivatization and Isolation of Semiconductor Cluster Molecules. *J. Am. Chem. Soc.* **1988**, *110*, 3046−3050.
(64) Murray, C. B.; Norris, D. J.; Bawendi, M. G. *J. Am. Chem. Soc.* **1993**, *115*, 8706−8715.
(65) Murray, C. B. *Synthesis and Characterization of II-IV Quantum Dots and Their Assembly into 3D Quantum Dot Superlattices*; Massachusetts Institute of Technology: 1995.
(66) Owen, J. S.; Chan, E. M.; Liu, H.; Alivisatos, A. P. Precursor Conversion Kinetics and the Nucleation of Cadmium Selenide Nanocrystals. *J. Am. Chem. Soc.* **2010**, *132*, 18206−18213.
(67) LaMer, V. K.; Dinegar, R. H. Theory, Production and Mechanism of Formation of Monodispersed Hydrosols. *J. Am. Chem. Soc.* **1950**, *72*, 4847−4854.
(68) Abe, S.; Čapek, R. K.; De Geyter, B.; Hens, Z. Tuning the Postfocused Size of Colloidal Nanocrystals by the Reaction Rate: From Theory to Application. *ACS Nano* **2012**, *6*, 42−53.
(69) Yin, Y.; Alivisatos, A. P. Colloidal Nanocrystal Synthesis and the Organic-Inorganic Interface. *Nature* **2005**, *437*, 664−670.
(70) Vengrenovich, R. D.; Gudyma, Y. V.; Yarema, S. V. Ostwald Ripening of Quantum-Dot Nanostructures. *Semiconductors* **2001**, *35*, 1378−1382.
(71) Slejko, E. A.; Lughi, V. Size Control at Maximum Yield and Growth Kinetics of Colloidal II-VI Semiconductor Nanocrystals. *J. Phys. Chem. C* **2019**, *123*, 1421−1428.
(72) Peng, Z. A.; Peng, X. Formation of High-Quality CdTe, CdSe, and CdS Nanocrystals Using CdO as Precursor. *J. Am. Chem. Soc.* **2001**, *123*, 183−184.
(73) Qu, L.; Peng, Z. A.; Peng, X. Alternative Routes toward High Quality CdSe Nanocrystals. *Nano Lett.* **2001**, *1*, 333−337.
(74) Ghorpade, U.; Suryawanshi, M.; Shin, S. W.; Gurav, K.; Patil, P.; Pawar, S.; Hong, C. W.; Kim, J. H.; Kolekar, S. Towards Environmentally Benign Approaches for the Synthesis of CZTSSe Nanocrystals by a Hot Injection Method: A Status Review. *Chem. Commun.* **2014**, *50*, 11258.
(75) Peng, X. Green Chemical Approaches toward High-Quality Semiconductor Nanocrystals. *Chem. - Eur. J.* **2002**, *8*, 334−339.
(76) Yu, W. W.; Peng, X. Formation of High-Quality CdS and Other II-VI Semiconductor Nanocrystals in Noncoordinating Solvents: Tunable Reactivity of Monomers. *Angew. Chem., Int. Ed.* **2002**, *41*, 2368−2371.
(77) Zlateva, G.; Zhelev, Z.; Bakalova, R.; Kanno, I. Precise Size Control and Synchronized Synthesis of Six Colors of CdSe Quantum Dots in a Slow-Increasing Temperature Gradient. *Inorg. Chem.* **2007**, *46*, 6212−6214.
(78) Deng, Z.; Cao, L.; Tang, F.; Zou, B. A New Route to Zinc-Blende CdSe Nanocrystals: Mechanism and Synthesis. *J. Phys. Chem. B* **2005**, *109*, 16671−16675.
(79) Zhu, C.-N.; Jiang, P.; Zhang, Z.-L.; Zhu, D.-L.; Tian, Z.-Q.; Pang, D.-W. Ag_2Se Quantum Dots with Tunable Emission in the Second Near-Infrared Window. *ACS Appl. Mater. Interfaces* **2013**, *5*, 1186−1189.
(80) Jiang, P.; Tian, Z.-Q.; Zhu, C.-N.; Zhang, Z.-L.; Pang, D.-W. Emission-Tunable Near-Infrared Ag_2S Quantum Dots. *Chem. Mater.* **2012**, *24*, 3−5.
(81) Lu, Y.; Yang, Y.; Guan, L.; Wang, D.; Zhao, J.; Yang, J.; Wei, Z.; Wang, F.; Yang, Z.; Li, X. Luminescent Modulation of Zinc Sulphide Nano-Particles by Thermal Injection Method. *J. Lumin.* **2020**, *226*, 117332.
(82) Reiss, P. ZnSe Based Colloidal Nanocrystals: Synthesis, Shape Control, Core/Shell, Alloy and Doped Systems. *New J. Chem.* **2007**, *31*, 1843.
(83) Wang, X.; Ma, X. L.; Feng, X.; Zheng, Y. F. Controlled Synthesis and Characterization of ZnSe Quantum Dots. *J. Nanosci. Nanotechnol.* **2010**, *10*, 7812−7815.
(84) Li, H.; Chen, D.; Li, L.; Tang, F.; Zhang, L.; Ren, J. Size- and Shape-Controlled Synthesis of PbSe and PbS Nanocrystalsvia a Facile Method. *CrystEngComm* **2010**, *12*, 1127−1133.
(85) Acharya, K. P.; Khon, E.; O'Connor, T.; O'Conner, T.; Nemitz, I.; Klinkova, A.; Khnayzer, R. S.; Anzenbacher, P.; Zamkov, M. Heteroepitaxial Growth of Colloidal Nanocrystals onto Substrate Films via Hot-Injection Routes. *ACS Nano* **2011**, *5*, 4953−4964.
(86) Hines, M. A.; Scholes, G. D. Colloidal PbS Nanocrystals with Size-Tunable Near-Infrared Emission: Observation of Post-Synthesis Self-Narrowing of the Particle Size Distribution. *Adv. Mater.* **2003**, *15*, 1844−1849.

https://dx.doi.org/10.1021/acs.chemrev.0c00831
Chem. Rev. 2021, 121, 3186−3233

(87) Murray, C. B.; Sun, S.; Gaschler, W.; Doyle, H.; Betley, T. A.; Kagan. Colloidal Synthesis of Nanocrystals and Nanocrystal Superlattices. *IBM J. Res. Dev.* **2001**, *45*, 47−56.
(88) Song, W.-S.; Lee, H.-S.; Lee, J. C.; Jang, D. S.; Choi, Y.; Choi, M.; Yang, H. Amine-Derived Synthetic Approach to Color-Tunable InP/ZnS Quantum Dots with High Fluorescent Qualities. *J. Nanopart. Res.* **2013**, *15*, 1750.
(89) Tietze, R.; Panzer, R.; Starzynski, T.; Guhrenz, C.; Frenzel, F.; Würth, C.; Resch-Genger, U.; Weigand, J. J.; Eychmüller, A. Synthesis of NIR-Emitting InAs-Based Core/Shell Quantum Dots with the Use of Tripyrazolylarsane as Arsenic Precursor. *Part. Part. Syst. Charact.* **2018**, *35*, 1800175.
(90) Protesescu, L.; Yakunin, S.; Bodnarchuk, M. I.; Krieg, F.; Caputo, R.; Hendon, C. H.; Yang, R. X.; Walsh, A.; Kovalenko, M. V. Nanocrystals of Cesium Lead Halide Perovskites ($CsPbX_3$, X = Cl, Br, and I): Novel Optoelectronic Materials Showing Bright Emission with Wide Color Gamut. *Nano Lett.* **2015**, *15*, 3692−3696.
(91) Wang, A.; Yan, X.; Zhang, M.; Sun, S.; Yang, M.; Shen, W.; Pan, X.; Wang, P.; Deng, Z. Controlled Synthesis of Lead-Free and Stable Perovskite Derivative Cs_2SnI_6 Nanocrystals via a Facile Hot-Injection Process. *Chem. Mater.* **2016**, *28*, 8132−8140.
(92) Masala, O.; Seshadri, R. SYNTHESIS ROUTES FOR LARGE VOLUMES OF NANOPARTICLES. *Annu. Rev. Mater. Res.* **2004**, *34*, 41−81.
(93) Pradhan, N.; Efrima, S. Single-Precursor, One-Pot Versatile Synthesis under near Ambient Conditions of Tunable, Single and Dual Band Fluorescing Metal Sulfide Nanoparticles. *J. Am. Chem. Soc.* **2003**, *125*, 2050−2051.
(94) Park, J.; Joo, J.; Kwon, S. G.; Jang, Y.; Hyeon, T. Synthesis of Monodisperse Spherical Nanocrystals. *Angew. Chem., Int. Ed.* **2007**, *46*, 4630−4660.
(95) van Embden, J.; Chesman, A. S. R.; Jasieniak, J. J. The Heat-Up Synthesis of Colloidal Nanocrystals. *Chem. Mater.* **2015**, *27*, 2246−2285.
(96) Kwon, S. G.; Hyeon, T. Formation Mechanisms of Uniform Nanocrystals via Hot-Injection and Heat-Up Methods. *Small* **2011**, *7*, 2685−2702.
(97) Nguyen, T.-D. From Formation Mechanisms to Synthetic Methods toward Shape-Controlled Oxide Nanoparticles. *Nanoscale* **2013**, *5*, 9455.
(98) Tao, A. R.; Habas, S.; Yang, P. Shape Control of Colloidal Metal Nanocrystals. *Small* **2008**, *4*, 310−325.
(99) Yang, Y. A.; Wu, H.; Williams, K. R.; Cao, Y. C. Synthesis of CdSe and CdTe Nanocrystals without Precursor Injection. *Angew. Chem., Int. Ed.* **2005**, *44*, 6712−6715.
(100) Cao, Y. C.; Wang, J. One-Pot Synthesis of High-Quality Zinc-Blende CdS Nanocrystals. *J. Am. Chem. Soc.* **2004**, *126*, 14336−14337.
(101) Zhao, T.; Oh, N.; Jishkariani, D.; Zhang, M.; Wang, H.; Li, N.; Lee, J. D.; Zeng, C.; Muduli, M.; Choi, H.-J.; Su, D.; Murray, C. B.; Kagan, C. R. General Synthetic Route to High-Quality Colloidal III-V Semiconductor Quantum Dots Based on Pnictogen Chlorides. *J. Am. Chem. Soc.* **2019**, *141*, 15145−15152.
(102) Lignos, I.; Protesescu, L.; Stavrakis, S.; Piveteau, L.; Speirs, M. J.; Loi, M. A.; Kovalenko, M. V.; deMello, A. J. Facile Droplet-Based Microfluidic Synthesis of Monodisperse IV-VI Semiconductor Nanocrystals with Coupled In-Line NIR Fluorescence Detection. *Chem. Mater.* **2014**, *26*, 2975−2982.
(103) Maceiczyk, R. M.; Bezinge, L.; deMello, A. J. Kinetics of Nanocrystal Synthesis in a Microfluidic Reactor: Theory and Experiment. *React. Chem. Eng.* **2016**, *1*, 261−271.
(104) Phillips, T. W.; Lignos, I. G.; Maceiczyk, R. M.; deMello, A. J.; deMello, J. C. Nanocrystal Synthesis in Microfluidic Reactors: Where Next? *Lab Chip* **2014**, *14*, 3172.
(105) Song, Y.; Hormes, J.; Kumar, C. S. S. R. Microfluidic Synthesis of Nanomaterials. *Small* **2008**, *4*, 698−711.
(106) Nightingale, A. M.; de Mello, J. C. Microscale Synthesis of Quantum Dots. *J. Mater. Chem.* **2010**, *20*, 8454.
(107) Marre, S.; Park, J.; Rempel, J.; Guan, J.; Bawendi, M. G.; Jensen, K. F. Supercritical Continuous-Microflow Synthesis of Narrow Size Distribution Quantum Dots. *Adv. Mater.* **2008**, *20*, 4830−4834.
(108) Kowalczyk, B.; Lagzi, I.; Grzybowski, B. A. Nanoseparations: Strategies for Size and/or Shape-Selective Purification of Nanoparticles. *Curr. Opin. Colloid Interface Sci.* **2011**, *16*, 135−148.
(109) Shen, Y.; Gee, M. Y.; Greytak, A. B. Purification Technologies for Colloidal Nanocrystals. *Chem. Commun.* **2017**, *53*, 827−841.
(110) Gravelsins, S.; Dhirani, A.-A. A Rapid, High Yield Size-Selective Precipitation Method for Generating Au Nanoparticles in Organic Solvents with Tunably Monodisperse Size Distributions and Replaceable Ligands. *RSC Adv.* **2017**, *7*, 55830−55834.
(111) Akdas, T.; Walter, J.; Segets, D.; Distaso, M.; Winter, B.; Birajdar, B.; Spiecker, E.; Peukert, W. Investigation of the Size-Property Relationship in $CuInS_2$ Quantum Dots. *Nanoscale* **2015**, *7*, 18105−18118.
(112) Peterson, M. D.; Cass, L. C.; Harris, R. D.; Edme, K.; Sung, K.; Weiss, E. A. The Role of Ligands in Determining the Exciton Relaxation Dynamics in Semiconductor Quantum Dots. *Annu. Rev. Phys. Chem.* **2014**, *65*, 317−339.
(113) Weiss, E. A. Organic Molecules as Tools To Control the Growth, Surface Structure, and Redox Activity of Colloidal Quantum Dots. *Acc. Chem. Res.* **2013**, *46*, 2607−2615.
(114) Boles, M. A.; Ling, D.; Hyeon, T.; Talapin, D. V. The Surface Science of Nanocrystals. *Nat. Mater.* **2016**, *15*, 141−153.
(115) Reiss, P.; Protière, M.; Li, L. Core/Shell Semiconductor Nanocrystals. *Small* **2009**, *5*, 154−168.
(116) Goodwin, E. D.; Straus, D. B. D. B.; Gaulding, E. A. A.; Murray, C. B. C. B.; Kagan, C. R. C. R. The Effects of Inorganic Surface Treatments on Photogenerated Carrier Mobility and Lifetime in PbSe Quantum Dot Thin Films. *Chem. Phys.* **2016**, *471*, 81−88.
(117) Anderson, N. C.; Hendricks, M. P.; Choi, J. J.; Owen, J. S. Ligand Exchange and the Stoichiometry of Metal Chalcogenide Nanocrystals: Spectroscopic Observation of Facile Metal-Carboxylate Displacement and Binding. *J. Am. Chem. Soc.* **2013**, *135*, 18536−18548.
(118) Hassinen, A.; Moreels, I.; De Nolf, K.; Smet, P. F.; Martins, J. C.; Hens, Z. Short-Chain Alcohols Strip X-Type Ligands and Quench the Luminescence of PbSe and CdSe Quantum Dots, Acetonitrile Does Not. *J. Am. Chem. Soc.* **2012**, *134*, 20705−20712.
(119) Shakeri, B.; Meulenberg, R. W. A Closer Look into the Traditional Purification Process of CdSe Semiconductor Quantum Dots. *Langmuir* **2015**, *31*, 13433−13440.
(120) Tan, R.; Shen, Y.; Roberts, S. K.; Gee, M. Y.; Blom, D. A.; Greytak, A. B. Reducing Competition by Coordinating Solvent Promotes Morphological Control in Alternating Layer Growth of CdSe/CdS Core/Shell Quantum Dots. *Chem. Mater.* **2015**, *27*, 7468−7480.
(121) Shen, Y.; Gee, M. Y.; Tan, R.; Pellechia, P. J.; Greytak, A. B. Purification of Quantum Dots by Gel Permeation Chromatography and the Effect of Excess Ligands on Shell Growth and Ligand Exchange. *Chem. Mater.* **2013**, *25*, 2838−2848.
(122) Tovstun, S. A.; Razumov, V. F. Theory of Size-Selective Precipitation. *J. Nanopart. Res.* **2017**, *19*, 8.
(123) Sarmphim, P.; Jantaratana, P.; Sirisathitkul, C. Size-Selective Precipitation and Aggregate Reduction of FePt-Based Nanoparticles. *J. Nanomater.* **2018**, *2018*, 1−5.
(124) Morris-Cohen, A. J.; Frederick, M. T.; Lilly, G. D.; McArthur, E. A.; Weiss, E. A. Organic Surfactant-Controlled Composition of the Surfaces of CdSe Quantum Dots. *J. Phys. Chem. Lett.* **2010**, *1*, 1078−1081.
(125) Morris-Cohen, A. J.; Donakowski, M. D.; Knowles, K. E.; Weiss, E. A. The Effect of a Common Purification Procedure on the Chemical Composition of the Surfaces of CdSe Quantum Dots Synthesized with Trioctylphosphine Oxide. *J. Phys. Chem. C* **2010**, *114*, 897−906.
(126) Virieux, H.; Le Troedec, M.; Cros-Gagneux, A.; Ojo, W.-S.; Delpech, F.; Nayral, C.; Martinez, H.; Chaudret, B. InP/ZnS Nanocrystals: Coupling NMR and XPS for Fine Surface and Interface Description. *J. Am. Chem. Soc.* **2012**, *134*, 19701−19708.

https://dx.doi.org/10.1021/acs.chemrev.0c00831
Chem. Rev. 2021, 121, 3186−3233

(127) Cros-Gagneux, A.; Delpech, F.; Nayral, C.; Cornejo, A.; Coppel, Y.; Chaudret, B. Surface Chemistry of InP Quantum Dots: A Comprehensive Study. *J. Am. Chem. Soc.* **2010**, *132*, 18147−18157.
(128) Anand, M.; Odom, L. A.; Roberts, C. B. Finely Controlled Size-Selective Precipitation and Separation of CdSe/ZnS Semiconductor Nanocrystals Using CO 2 -Gas-Expanded Liquids. *Langmuir* **2007**, *23*, 7338−7343.
(129) Anand, M.; You, S.-S.; Hurst, K. M.; Saunders, S. R.; Kitchens, C. L.; Ashurst, W. R.; Roberts, C. B. Thermodynamic Analysis of Nanoparticle Size Selective Fractionation Using Gas-Expanded Liquids. *Ind. Eng. Chem. Res.* **2008**, *47*, 553−559.
(130) Shah, P. S.; Holmes, J. D.; Johnston, K. P.; Korgel, B. A. Size-Selective Dispersion of Dodecanethiol-Coated Nanocrystals in Liquid and Supercritical Ethane by Density Tuning. *J. Phys. Chem. B* **2002**, *106*, 2545−2551.
(131) Smith, A. M.; Mohs, A. M.; Nie, S. Tuning the Optical and Electronic Properties of Colloidal Nanocrystals by Lattice Strain. *Nat. Nanotechnol.* **2009**, *4*, 56−63.
(132) Yu, W. W.; Qu, L.; Guo, W.; Peng, X. Experimental Determination of the Extinction Coefficient of CdTe, CdSe, and CdS Nanocrystals. *Chem. Mater.* **2003**, *15*, 2854−2860.
(133) Li, Z.; Ji, Y.; Xie, R.; Grisham, S. Y.; Peng, X. Correlation of CdS Nanocrystal Formation with Elemental Sulfur Activation and Its Implication in Synthetic Development. *J. Am. Chem. Soc.* **2011**, *133*, 17248−17256.
(134) Nan, W.; Niu, Y.; Qin, H.; Cui, F.; Yang, Y.; Lai, R.; Lin, W.; Peng, X. Crystal Structure Control of Zinc-Blende CdSe/CdS Core/Shell Nanocrystals: Synthesis and Structure-Dependent Optical Properties. *J. Am. Chem. Soc.* **2012**, *134*, 19685−19693.
(135) Yang, Y.; Li, J.; Lin, L.; Peng, X. An Efficient and Surface-Benign Purification Scheme for Colloidal Nanocrystals Based on Quantitative Assessment. *Nano Res.* **2015**, *8*, 3353−3364.
(136) Smith, A. M.; Nie, S. Minimizing the Hydrodynamic Size of Quantum Dots with Multifunctional Multidentate Polymer Ligands. *J. Am. Chem. Soc.* **2008**, *130*, 11278−11279.
(137) Pu, C.; Zhou, J.; Lai, R.; Niu, Y.; Nan, W.; Peng, X. Highly Reactive, Flexible yet Green Se Precursor for Metal Selenide Nanocrystals: Se-Octadecene Suspension (Se-SUS). *Nano Res.* **2013**, *6*, 652−670.
(138) Bai, L.; Ma, X.; Liu, J.; Sun, X.; Zhao, D.; Evans, D. G. Rapid Separation and Purification of Nanoparticles in Organic Density Gradients. *J. Am. Chem. Soc.* **2010**, *132*, 2333−2337.
(139) Sapsford, K. E.; Tyner, K. M.; Dair, B. J.; Deschamps, J. R.; Medintz, I. L. Analyzing Nanomaterial Bioconjugates: A Review of Current and Emerging Purification and Characterization Techniques. *Anal. Chem.* **2011**, *83*, 4453−4488.
(140) Prantner, A. M.; Chen, J.; Murray, C. B.; Scholler, N. Coating Evaluation and Purification of Monodisperse, Water-Soluble, Magnetic Nanoparticles Using Sucrose Density Gradient Ultracentrifugation. *Chem. Mater.* **2012**, *24*, 4008−4010.
(141) Carion, O.; Mahler, B.; Pons, T.; Dubertret, B. Synthesis, Encapsulation, Purification and Coupling of Single Quantum Dots in Phospholipid Micelles for Their Use in Cellular and in Vivo Imaging. *Nat. Protoc.* **2007**, *2*, 2383−2390.
(142) Li, P.; Huang, J.; Luo, L.; Kuang, Y.; Sun, X. Universal Parameter Optimization of Density Gradient Ultracentrifugation Using CdSe Nanoparticles as Tracing Agents. *Anal. Chem.* **2016**, *88*, 8495−8501.
(143) Akbulut, O.; Mace, C. R.; Martinez, R. V.; Kumar, A. A.; Nie, Z.; Patton, M. R.; Whitesides, G. M. Separation of Nanoparticles in Aqueous Multiphase Systems through Centrifugation. *Nano Lett.* **2012**, *12*, 4060−4064.
(144) Liu, R.; Zhou, J.-H.; Zhou, Z.-K.; Jiang, X.; Liu, J.; Liu, G.; Wang, X.-H. On-Demand Shape and Size Purification of Nanoparticle Based on Surface Area. *Nanoscale* **2014**, *6*, 13145−13153.
(145) Xiong, B.; Cheng, J.; Qiao, Y.; Zhou, R.; He, Y.; Yeung, E. S. Separation of Nanorods by Density Gradient Centrifugation. *J. Chromatogr. A* **2011**, *1218*, 3823−3829.
(146) Sharma, V.; Park, K.; Srinivasarao, M. Shape Separation of Gold Nanorods Using Centrifugation. *Proc. Natl. Acad. Sci. U. S. A.* **2009**, *106*, 4981−4985.
(147) Krieg, E.; Weissman, H.; Shirman, E.; Shimoni, E.; Rybtchinski, B. A Recyclable Supramolecular Membrane for Size-Selective Separation of Nanoparticles. *Nat. Nanotechnol.* **2011**, *6*, 141−146.
(148) Xing, Y.; Chaudry, Q.; Shen, C.; Kong, K. Y.; Zhau, H. E.; Chung, L. W.; Petros, J. A.; O'Regan, R. M.; Yezhelyev, M. V.; Simons, J. W.; Wang, M. D.; Nie, S. Bioconjugated Quantum Dots for Multiplexed and Quantitative Immunohistochemistry. *Nat. Protoc.* **2007**, *2*, 1152−1165.
(149) Zhang, X.; Shamirian, A.; Jawaid, A. M.; Tyrakowski, C. M.; Page, L. E.; Das, A.; Chen, O.; Isovic, A.; Hassan, A.; Snee, P. T. Monolayer Silane-Coated, Water-Soluble Quantum Dots. *Small* **2015**, *11*, 6091−6096.
(150) Dong, C.; Qian, H.; Fang, N.; Ren, J. Study of Fluorescence Quenching and Dialysis Process of CdTe Quantum Dots, Using Ensemble Techniques and Fluorescence Correlation Spectroscopy. *J. Phys. Chem. B* **2006**, *110*, 11069−11075.
(151) Alkilany, A. M.; Abulateefeh, S. R.; Mills, K. K.; Bani Yaseen, A. I.; Hamaly, M. A.; Alkhatib, H. S.; Aiedeh, K. M.; Stone, J. W. Colloidal Stability of Citrate and Mercaptoacetic Acid Capped Gold Nanoparticles upon Lyophilization: Effect of Capping Ligand Attachment and Type of Cryoprotectants. *Langmuir* **2014**, *30*, 13799−13808.
(152) El-Safty, S. A.; Mekawy, M.; Yamaguchi, A.; Shahat, A.; Ogawa, K.; Teramae, N. Organic-Inorganic Mesoporous Silica Nanostrands for Ultrafine Filtration of Spherical Nanoparticles. *Chem. Commun.* **2010**, *46*, 3917.
(153) Viswanath, A.; Shen, Y.; Green, A. N.; Tan, R.; Greytak, A. B.; Benicewicz, B. C. Copolymerization and Synthesis of Multiply Binding Histamine Ligands for the Robust Functionalization of Quantum Dots. *Macromolecules* **2014**, *47*, 8137−8144.
(154) Liu, W.; Choi, H. S.; Zimmer, J. P.; Tanaka, E.; Frangioni, J. V.; Bawendi, M. Compact Cysteine-Coated CdSe(ZnCdS) Quantum Dots for in Vivo Applications. *J. Am. Chem. Soc.* **2007**, *129*, 14530−14531.
(155) Wang, W.; Kapur, A.; Ji, X.; Zeng, B.; Mishra, D.; Mattoussi, H. Multifunctional and High Affinity Polymer Ligand That Provides Bio-Orthogonal Coating of Quantum Dots. *Bioconjugate Chem.* **2016**, *27*, 2024−2036.
(156) Gaborski, T. R.; Snyder, J. L.; Striemer, C. C.; Fang, D. Z.; Hoffman, M.; Fauchet, P. M.; McGrath, J. L. High-Performance Separation of Nanoparticles with Ultrathin Porous Nanocrystalline Silicon Membranes. *ACS Nano* **2010**, *4*, 6973−6981.
(157) Lee, H.; Segets, D.; Süß, S.; Peukert, W.; Chen, S.-C.; Pui, D. Y. H. Retention Mechanisms of 1.7 nm ZnS Quantum Dots and Sub-20 nm Au Nanoparticles in Ultrafiltration Membranes. *J. Membr. Sci.* **2018**, *567*, 58−67.
(158) Kim, D.; Park, H. K.; Choi, H.; Noh, J.; Kim, K.; Jeong, S. Continuous Flow Purification of Nanocrystal Quantum Dots. *Nanoscale* **2014**, *6*, 14467−14472.
(159) Sperling, R. A.; Pellegrino, T.; Li, J. K.; Chang, W. H.; Parak, W. J. Electrophoretic Separation of Nanoparticles with a Discrete Number of Functional Groups. *Adv. Funct. Mater.* **2006**, *16*, 943−948.
(160) Howarth, M.; Liu, W.; Puthenveetil, S.; Zheng, Y.; Marshall, L. F.; Schmidt, M. M.; Wittrup, K. D.; Bawendi, M. G.; Ting, A. Y. Monovalent, Reduced-Size Quantum Dots for Imaging Receptors on Living Cells. *Nat. Methods* **2008**, *5*, 397−399.
(161) Liu, W.; Greytak, A. B.; Lee, J.; Wong, C. R.; Park, J.; Marshall, L. F.; Jiang, W.; Curtin, P. N.; Ting, A. Y.; Nocera, D. G.; Fukumura, D.; Jain, R. K.; Bawendi, M. G. Compact Biocompatible Quantum Dots via RAFT-Mediated Synthesis of Imidazole-Based Random Copolymer Ligand. *J. Am. Chem. Soc.* **2010**, *132*, 472−483.
(162) Lim, H.; Woo, J. Y.; Lee, D. C.; Lee, J.; Jeong, S.; Kim, D. Continuous Purification of Colloidal Quantum Dots in Large-Scale Using Porous Electrodes in Flow Channel. *Sci. Rep.* **2017**, *7*, 43581.
(163) Ho, S.; Critchley, K.; Lilly, G. D.; Shim, B.; Kotov, N. A. Free Flow Electrophoresis for the Separation of CdTe Nanoparticles. *J. Mater. Chem.* **2009**, *19*, 1390.

https://dx.doi.org/10.1021/acs.chemrev.0c00831
Chem. Rev. 2021, 121, 3186−3233

(164) Bass, J. D.; Ai, X.; Bagabas, A.; Rice, P. M.; Topuria, T.; Scott, J. C.; Alharbi, F. H.; Kim, H.-C.; Song, Q.; Miller, R. D. An Efficient and Low-Cost Method for the Purification of Colloidal Nanoparticles. *Angew. Chem., Int. Ed.* **2011**, *50*, 6538−6542.
(165) Lhuillier, E.; Hease, P.; Ithurria, S.; Dubertret, B. Selective Electrophoretic Deposition of CdSe Nanoplatelets. *Chem. Mater.* **2014**, *26*, 4514−4520.
(166) Shen, Y.; Weeranoppanant, N.; Xie, L.; Chen, Y.; Lusardi, M. R.; Imbrogno, J.; Bawendi, M. G.; Jensen, K. F. Multistage Extraction Platform for Highly Efficient and Fully Continuous Purification of Nanoparticles. *Nanoscale* **2017**, *9*, 7703−7707.
(167) Lévy, R.; Wang, Z.; Duchesne, L.; Doty, R. C.; Cooper, A. I.; Brust, M.; Fernig, D. G. A Generic Approach to Monofunctionalized Protein-Like Gold Nanoparticles Based on Immobilized Metal Ion Affinity Chromatography. *ChemBioChem* **2006**, *7*, 592−594.
(168) Goldman, E. R.; Anderson, G. P.; Tran, P. T.; Mattoussi, H.; Charles, P. T.; Mauro, J. M. Conjugation of Luminescent Quantum Dots with Antibodies Using an Engineered Adaptor Protein To Provide New Reagents for Fluoroimmunoassays. *Anal. Chem.* **2002**, *74*, 841−847.
(169) Claridge, S. A.; Goh, S. L.; Fréchet, J. M. J.; Williams, S. C.; Micheel, C. M.; Alivisatos, A. P. Directed Assembly of Discrete Gold Nanoparticle Groupings Using Branched DNA Scaffolds. *Chem. Mater.* **2005**, *17*, 1628−1635.
(170) Reiss, P.; Carrière, M.; Lincheneau, C.; Vaure, L.; Tamang, S. Synthesis of Semiconductor Nanocrystals, Focusing on Nontoxic and Earth-Abundant Materials. *Chem. Rev.* **2016**, *116*, 10731−10819.
(171) Novak, J. P.; Nickerson, C.; Franzen, S.; Feldheim, D. L. Purification of Molecularly Bridged Metal Nanoparticle Arrays by Centrifugation and Size Exclusion Chromatography. *Anal. Chem.* **2001**, *73*, 5758−5761.
(172) Shen, Y.; Roberge, A.; Tan, R.; Gee, M. Y.; Gary, D. C.; Huang, Y.; Blom, D. A.; Benicewicz, B. C.; Cossairt, B. M.; Greytak, A. B. Gel Permeation Chromatography as a Multifunctional Processor for Nanocrystal Purification and On-Column Ligand Exchange Chemistry. *Chem. Sci.* **2016**, *7*, 5671−5679.
(173) Pitkänen, L.; Striegel, A. M. Size-Exclusion Chromatography of Metal Nanoparticles and Quantum Dots. *TrAC, Trends Anal. Chem.* **2016**, *80*, 311−320.
(174) Gary, D. C.; Terban, M. W.; Billinge, S. J. L.; Cossairt, B. M. Two-Step Nucleation and Growth of InP Quantum Dots via Magic-Sized Cluster Intermediates. *Chem. Mater.* **2015**, *27*, 1432−1441.
(175) Jadzinsky, P. D.; Calero, G.; Ackerson, C. J.; Bushnell, D. A.; Kornberg, R. D. Structure of a Thiol Monolayer-Protected Gold Nanoparticle at 1.1 Å Resolution. *Science (Washington, DC, U. S.)* **2007**, *318*, 430−433.
(176) Owen, J. S.; Park, J.; Trudeau, P.-E.; Alivisatos, A. P. Reaction Chemistry and Ligand Exchange at Cadmium-Selenide Nanocrystal Surfaces. *J. Am. Chem. Soc.* **2008**, *130*, 12279−12281.
(177) Fritzinger, B.; Capek, R. K.; Lambert, K.; Martins, J. C.; Hens, Z. Utilizing Self-Exchange To Address the Binding of Carboxylic Acid Ligands to CdSe Quantum Dots. *J. Am. Chem. Soc.* **2010**, *132*, 10195−10201.
(178) Piveteau, L.; Ong, T.-C.; Rossini, A. J.; Emsley, L.; Copéret, C.; Kovalenko, M. V. Structure of Colloidal Quantum Dots from Dynamic Nuclear Polarization Surface Enhanced NMR Spectroscopy. *J. Am. Chem. Soc.* **2015**, *137*, 13964−13971.
(179) Gary, D. C.; Cossairt, B. M. Role of Acid in Precursor Conversion During InP Quantum Dot Synthesis. *Chem. Mater.* **2013**, *25*, 2463−2469.
(180) De Roo, J.; Justo, Y.; De Keukeleere, K.; Van den Broeck, F.; Martins, J. C.; Van Driessche, I.; Hens, Z. Carboxylic-Acid-Passivated Metal Oxide Nanocrystals: Ligand Exchange Characteristics of a New Binding Motif. *Angew. Chem., Int. Ed.* **2015**, *54*, 6488−6491.
(181) Bullen, C.; Mulvaney, P. The Effects of Chemisorption on the Luminescence of CdSe Quantum Dots. *Langmuir* **2006**, *22*, 3007−3013.
(182) Wuister, S. F.; de Mello Donegá, C.; Meijerink, A. Influence of Thiol Capping on the Exciton Luminescence and Decay Kinetics of CdTe and CdSe Quantum Dots. *J. Phys. Chem. B* **2004**, *108*, 17393−17397.
(183) Munro, A. M.; Ginger, D. S. Photoluminescence Quenching of Single CdSe Nanocrystals by Ligand Adsorption. *Nano Lett.* **2008**, *8*, 2585−2590.
(184) Nepomnyashchii, A. B.; Harris, R. D.; Weiss, E. A. Composition and Permeability of Oleate Adlayers of CdS Quantum Dots upon Dilution to Photoluminescence-Relevant Concentrations. *Anal. Chem.* **2016**, *88*, 3310−3316.
(185) Munro, A. M.; Jen-La Plante, I.; Ng, M. S.; Ginger, D. S. Quantitative Study of the Effects of Surface Ligand Concentration on CdSe Nanocrystal Photoluminescence. *J. Phys. Chem. C* **2007**, *111*, 6220−6227.
(186) Kalyuzhny, G.; Murray, R. W. Ligand Effects on Optical Properties of CdSe Nanocrystals. *J. Phys. Chem. B* **2005**, *109*, 7012−7021.
(187) Shen, Y.; Tan, R.; Gee, M. Y.; Greytak, A. B. Quantum Yield Regeneration: Influence of Neutral Ligand Binding on Photophysical Properties in Colloidal Core/Shell Quantum Dots. *ACS Nano* **2015**, *9*, 3345−3359.
(188) Wuister, S. F.; van Houselt, A.; de Mello Donegá, C.; Vanmaekelbergh, D.; Meijerink, A. Temperature Antiquenching of the Luminescence from Capped CdSe Quantum Dots. *Angew. Chem.* **2004**, *116*, 3091−3095.
(189) Owen, J. The Coordination Chemistry of Nanocrystal Surfaces. *Science (Washington, DC, U. S.)* **2015**, *347*, 615−616.
(190) De Roo, J.; De Keukeleere, K.; Hens, Z.; Van Driessche, I. From Ligands to Binding Motifs and beyond; the Enhanced Versatility of Nanocrystal Surfaces. *Dalt. Trans.* **2016**, *45*, 13277−13283.
(191) Dierick, R.; Van den Broeck, F.; De Nolf, K.; Zhao, Q.; Vantomme, A.; Martins, J. C.; Hens, Z. Surface Chemistry of $CuInS_2$ Colloidal Nanocrystals, Tight Binding of L-Type Ligands. *Chem. Mater.* **2014**, *26*, 5950−5957.
(192) Goodwin, E. D. D.; Diroll, B. T.; Oh, S. J.; Paik, T.; Murray, C. B.; Kagan, C. R. Effects of Post-Synthesis Processing on CdSe Nanocrystals and Their Solids: Correlation between Surface Chemistry and Optoelectronic Properties. *J. Phys. Chem. C* **2014**, *118*, 27097−27105.
(193) Knittel, F.; Gravel, E.; Cassette, E.; Pons, T.; Pillon, F.; Dubertret, B.; Doris, E. On the Characterization of the Surface Chemistry of Quantum Dots. *Nano Lett.* **2013**, *13*, 5075−5078.
(194) Cirillo, M.; Strubbe, F.; Neyts, K.; Hens, Z. Thermal Charging of Colloidal Quantum Dots in Apolar Solvents: A Current Transient Analysis. *ACS Nano* **2011**, *5*, 1345−1352.
(195) Turo, M. J.; Shen, X.; Brandon, N. K.; Castillo, S.; Fall, A. M.; Pantelides, S. T.; Macdonald, J. E. Dual-Mode Crystal-Bound and X-Type Passivation of Quantum Dots. *Chem. Commun.* **2016**, *52*, 12214−12217.
(196) Turo, M. J.; Macdonald, J. E. Crystal-Bound *vs* Surface-Bound Thiols on Nanocrystals. *ACS Nano* **2014**, *8*, 10205−10213.
(197) Rivest, J. B.; Jain, P. K. Cation Exchange on the Nanoscale: An Emerging Technique for New Material Synthesis, Device Fabrication, and Chemical Sensing. *Chem. Soc. Rev.* **2013**, *42*, 89−96.
(198) Fayette, M.; Robinson, R. D. Chemical Transformations of Nanomaterials for Energy Applications. *J. Mater. Chem. A* **2014**, *2*, 5965−5978.
(199) Moon, G. D.; Ko, S.; Min, Y.; Zeng, J.; Xia, Y.; Jeong, U. Chemical Transformations of Nanostructured Materials. *Nano Today* **2011**, *6*, 186−203.
(200) Dawood, F.; Schaak, R. E. ZnO-Templated Synthesis of Wurtzite-Type ZnS and ZnSe Nanoparticles. *J. Am. Chem. Soc.* **2009**, *131*, 424−425.
(201) Chen, C.; Herhold, S. M.; Johnson, Y.; Alivisatos, A. P. Size Dependence of Structural Metastability in Semiconductor Nanocrystals. *Science (Washington, DC, U. S.)* **1997**, *276*, 398−401.
(202) Eychmüller, A.; Mews, A.; Weller, H. A Quantum Dot Quantum Well: CdS/HgS/CdS. *Chem. Phys. Lett.* **1993**, *208*, 59−62.
(203) De Trizio, L.; Manna, L. Forging Colloidal Nanostructures via Cation Exchange Reactions. *Chem. Rev.* **2016**, *116*, 10852−10887.

https://dx.doi.org/10.1021/acs.chemrev.0c00831
Chem. Rev. 2021, 121, 3186−3233

(204) Beberwyck, B. J.; Surendranath, Y.; Alivisatos, A. P. Cation Exchange: A Versatile Tool for Nanomaterials Synthesis. *J. Phys. Chem. C* **2013**, *117*, 19759−19770.
(205) Wang, H.; Butler, D. J.; Straus, D. B.; Oh, N.; Wu, F.; Guo, J.; Xue, K.; Lee, J. D.; Murray, C. B.; Kagan, C. R. Air-Stable CuInSe 2 Nanocrystal Transistors and Circuits via Post-Deposition Cation Exchange. *ACS Nano* **2019**, *13*, 2324−2333.
(206) Son, D. H.; Hughes, S. M.; Yin, Y.; Paul Alivisatos, A. Cation Exchange Reactions in Ionic Nanocrystals. *Science* **2004**, *306*, 1009−1012.
(207) Zhou, H. S.; Sasahara, H.; Honma, I.; Komiyama, H.; Haus, J. W. Coated Semiconductor Nanoparticles: The CdS/PbS System's Photoluminescence Properties. *Chem. Mater.* **1994**, *6*, 1534−1541.
(208) Sadtler, B.; Demchenko, D. O.; Zheng, H.; Hughes, S. M.; Merkle, M. G.; Dahmen, U.; Wang, L.-W.; Alivisatos, A. P. Selective Facet Reactivity during Cation Exchange in Cadmium Sulfide Nanorods. *J. Am. Chem. Soc.* **2009**, *131*, 5285−5293.
(209) Rivest, J. B.; Buonsanti, R.; Pick, T. E.; Zhu, L.; Lim, E.; Clavero, C.; Schaible, E.; Helms, B. A.; Milliron, D. J. Evolution of Ordered Metal Chalcogenide Architectures through Chemical Transformations. *J. Am. Chem. Soc.* **2013**, *135*, 7446−7449.
(210) Jain, P. K.; Beberwyck, B. J.; Fong, L.-K.; Polking, M. J.; Alivisatos, A. P. Highly Luminescent Nanocrystals from Removal of Impurity Atoms Residual from Ion-Exchange Synthesis. *Angew. Chem., Int. Ed.* **2012**, *51*, 2387−2390.
(211) Jain, P. K.; Amirav, L.; Aloni, S.; Alivisatos, A. P. Nano-heterostructure Cation Exchange: Anionic Framework Conservation. *J. Am. Chem. Soc.* **2010**, *132*, 9997−9999.
(212) Lubeck, C. R.; Han, T. Y.-J.; Gash, A. E.; Satcher, J. H.; Doyle, F. M. Synthesis of Mesostructured Copper Sulfide by Cation Exchange and Liquid-Crystal Templating. *Adv. Mater.* **2006**, *18*, 781−784.
(213) Li, J.; Zhang, T.; Ge, J.; Yin, Y.; Zhong, W. Fluorescence Signal Amplification by Cation Exchange in Ionic Nanocrystals. *Angew. Chem., Int. Ed.* **2009**, *48*, 1588−1591.
(214) Groeneveld, E.; Witteman, L.; Lefferts, M.; Ke, X.; Bals, S.; Van Tendeloo, G.; de Mello Donega, C. Tailoring ZnSe-CdSe Colloidal Quantum Dots *via* Cation Exchange: From Core/Shell to Alloy Nanocrystals. *ACS Nano* **2013**, *7*, 7913−7930.
(215) White, S. L.; Smith, J. G.; Behl, M.; Jain, P. K. Co-Operativity in a Nanocrystalline Solid-State Transition. *Nat. Commun.* **2013**, *4*, 2933.
(216) Routzahn, A. L.; Jain, P. K. Single-Nanocrystal Reaction Trajectories Reveal Sharp Cooperative Transitions. *Nano Lett.* **2014**, *14*, 987−992.
(217) Wark, S. E.; Hsia, C.-H.; Son, D. H. Effects of Ion Solvation and Volume Change of Reaction on the Equilibrium and Morphology in Cation-Exchange Reaction of Nanocrystals. *J. Am. Chem. Soc.* **2008**, *130*, 9550−9555.
(218) Mizusaki, J.; Arai, K.; Fueki, K. Ionic Conduction of the Perovskite-Type Halides. *Solid State Ionics* **1983**, *11*, 203−211.
(219) Stranks, S. D.; Snaith, H. J. Metal-Halide Perovskites for Photovoltaic and Light-Emitting Devices. *Nat. Nanotechnol.* **2015**, *10*, 391−402.
(220) Akkerman, Q. A.; D'Innocenzo, V.; Accornero, S.; Scarpellini, A.; Petrozza, A.; Prato, M.; Manna, L. Tuning the Optical Properties of Cesium Lead Halide Perovskite Nanocrystals by Anion Exchange Reactions. *J. Am. Chem. Soc.* **2015**, *137*, 10276−10281.
(221) Pellet, N.; Teuscher, J.; Maier, J.; Grätzel, M. Transforming Hybrid Organic Inorganic Perovskites by Rapid Halide Exchange. *Chem. Mater.* **2015**, *27*, 2181−2188.
(222) Koch, S. W.; Kira, M.; Khitrova, G.; Gibbs, H. M. Semiconductor Excitons in New Light. *Nat. Mater.* **2006**, *5*, 523−531.
(223) Woggon, U. *Optical Properties of Semiconductor Quantum Dots*; Springer: Berlin, 2013.
(224) Jasieniak, J.; Smith, L.; van Embden, J.; Mulvaney, P.; Califano, M. Re-Examination of the Size-Dependent Absorption Properties of CdSe Quantum Dots. *J. Phys. Chem. C* **2009**, *113*, 19468−19474.
(225) Leatherdale, C. A.; Woo, W.-K.; Mikulec, F. V.; Bawendi, M. G. On the Absorption Cross Section of CdSe Nanocrystal Quantum Dots. *J. Phys. Chem. B* **2002**, *106*, 7619−7622.
(226) Yu, P.; Beard, M. C.; Ellingson, R. J.; Ferrere, S.; Curtis, C.; Drexler, J.; Luiszer, F.; Nozik, A. J. Absorption Cross-Section and Related Optical Properties of Colloidal InAs Quantum Dots. *J. Phys. Chem. B* **2005**, *109*, 7084−7087.
(227) Efros, A. L.; Rosen, M.; Kuno, M.; Nirmal, M.; Norris, D. J.; Bawendi, M. Band-Edge Exciton in Quantum Dots of Semiconductors with a Degenerate Valence Band: Dark and Bright Exciton States. *Phys. Rev. B: Condens. Matter Mater. Phys.* **1996**, *54*, 4843−4856.
(228) Le Thomas, N.; Herz, E.; Schöps, O.; Woggon, U.; Artemyev, M. V. Exciton Fine Structure in Single CdSe Nanorods. *Phys. Rev. Lett.* **2005**, *94*, 016803.
(229) Isarov, M.; Tan, L. Z.; Bodnarchuk, M. I.; Kovalenko, M. V.; Rappe, A. M.; Lifshitz, E. Rashba Effect in a Single Colloidal $CsPbBr_3$ Perovskite Nanocrystal Detected by Magneto-Optical Measurements. *Nano Lett.* **2017**, *17*, 5020−5026.
(230) Becker, M. A.; Vaxenburg, R.; Nedelcu, G.; Sercel, P. C.; Shabaev, A.; Mehl, M. J.; Michopoulos, J. G.; Lambrakos, S. G.; Bernstein, N.; Lyons, J. L.; Stöferle, T.; Mahrt, R. F.; Kovalenko, M. V.; Norris, D. J.; Rainò, G.; Efros, A. L. Bright Triplet Excitons in Caesium Lead Halide Perovskites. *Nature* **2018**, *553*, 189−193.
(231) Tamarat, P.; Hou, L.; Trebbia, J.-B.; Swarnkar, A.; Biadala, L.; Louyer, Y.; Bodnarchuk, M. I.; Kovalenko, M. V.; Even, J.; Lounis, B. The Dark Exciton Ground State Promotes Photon-Pair Emission in Individual Perovskite Nanocrystals. *Nat. Commun.* **2020**, *11*, 6001.
(232) Rossi, D.; Liu, X.; Lee, Y.; Khurana, M.; Puthenpurayil, J.; Kim, K.; Akimov, A. V.; Cheon, J.; Son, D. H. Intense Dark Exciton Emission from Strongly Quantum-Confined CsPbBr3Nanocrystals. *Nano Lett.* **2020**, *20*, 7321−7326.
(233) Sercel, P. C.; Lyons, J. L.; Wickramaratne, D.; Vaxenburg, R.; Bernstein, N.; Efros, A. L. Exciton Fine Structure in Perovskite Nanocrystals. *Nano Lett.* **2019**, *19*, 4068−4077.
(234) Klimov, V. I. Spectral and Dynamical Properties of Multi-excitons in Semiconductor Nanocrystals. *Annu. Rev. Phys. Chem.* **2007**, *58*, 635−673.
(235) Oron, D.; Kazes, M.; Shweky, I.; Banin, U. Multiexciton Spectroscopy of Semiconductor Nanocrystals under Quasi-Continuous-Wave Optical Pumping. *Phys. Rev. B: Condens. Matter Mater. Phys.* **2006**, *74*, 115333.
(236) Osovsky, R.; Cheskis, D.; Kloper, V.; Sashchiuk, A.; Kroner, M.; Lifshitz, E. Continuous-Wave Pumping of Multiexciton Bands in the Photoluminescence Spectrum of a Single CdTe-CdSe Core-Shell Colloidal Quantum Dot. *Phys. Rev. Lett.* **2009**, *102*, 197401.
(237) Schaller, R. D.; Klimov, V. I. High Efficiency Carrier Multiplication in PbSe Nanocrystals: Implications for Solar Energy Conversion. *Phys. Rev. Lett.* **2004**, *92*, 186601.
(238) McGuire, J. A.; Joo, J.; Pietryga, J. M.; Schaller, R. D.; Klimov, V. I. New Aspects of Carrier Multiplication in Semiconductor Nanocrystals. *Acc. Chem. Res.* **2008**, *41*, 1810−1819.
(239) Beard, M. C. Multiple Exciton Generation in Semiconductor Quantum Dots. *J. Phys. Chem. Lett.* **2011**, *2*, 1282−1288.
(240) Semonin, O. E.; Luther, J. M.; Choi, S.; Chen, H.-Y.; Gao, J.; Nozik, A. J.; Beard, M. C. Peak External Photocurrent Quantum Efficiency Exceeding 100% via MEG in a Quantum Dot Solar Cell. *Science (Washington, DC, U. S.)* **2011**, *334*, 1530−1533.
(241) Bowers II, M. J.; McBride, J. R.; Garrett, M. D.; Sammons, J. A.; Dukes III, A. D.; Schreuder, M. A.; Watt, T. L.; Lupini, A. R.; Pennycook, S. J.; Rosenthal, S. J. Structure and Ultrafast Dynamics of White-Light-Emitting CdSe Nanocrystals. *J. Am. Chem. Soc.* **2009**, *131*, 5730−5731.
(242) Gao, Y.; Peng, X. Photogenerated Excitons in Plain Core CdSe Nanocrystals with Unity Radiative Decay in Single Channel: The Effects of Surface and Ligands. *J. Am. Chem. Soc.* **2015**, *137*, 4230−4235.
(243) Chen, O.; Zhao, J.; Chauhan, V. P.; Cui, J.; Wong, C.; Harris, D. K.; Wei, H.; Han, H.-S.; Fukumura, D.; Jain, R. K.; Bawendi, M. G. Compact High-Quality CdSe-CdS Core-Shell Nanocrystals with Narrow Emission Linewidths and Suppressed Blinking. *Nat. Mater.* **2013**, *12*, 445−451.

https://dx.doi.org/10.1021/acs.chemrev.0c00831
Chem. Rev. 2021, 121, 3186−3233

(244) Cui, J.; Beyler, A. P.; Bischof, T. S.; Wilson, M. W. B.; Bawendi, M. G. Deconstructing the Photon Stream from Single Nanocrystals: From Binning to Correlation. *Chem. Soc. Rev.* **2014**, *43*, 1287−1310.
(245) Empedocles, S.; Bawendi, M. Spectroscopy of Single CdSe Nanocrystallites. *Acc. Chem. Res.* **1999**, *32*, 389−396.
(246) Biadala, L.; Louyer, Y.; Tamarat, P.; Lounis, B. Direct Observation of the Two Lowest Exciton Zero-Phonon Lines in Single CdSe/ZnS Nanocrystals. *Phys. Rev. Lett.* **2009**, *103*, 037404.
(247) Brokmann, X.; Giacobino, E.; Dahan, M.; Hermier, J. P. Highly Efficient Triggered Emission of Single Photons by Colloidal CdSe/ZnS Nanocrystals. *Appl. Phys. Lett.* **2004**, *85*, 712−714.
(248) Rainò, G.; Nedelcu, G.; Protesescu, L.; Bodnarchuk, M. I.; Kovalenko, M. V.; Mahrt, R. F.; Stöferle, T. Single Cesium Lead Halide Perovskite Nanocrystals at Low Temperature: Fast Single-Photon Emission, Reduced Blinking, and Exciton Fine Structure. *ACS Nano* **2016**, *10*, 2485−2490.
(249) Utzat, H.; Sun, W.; Kaplan, A. E. K.; Krieg, F.; Ginterseder, M.; Spokoyny, B.; Klein, N. D.; Shulenberger, K. E.; Perkinson, C. F.; Kovalenko, M. V.; Bawendi, M. G. Coherent Single-Photon Emission from Colloidal Lead Halide Perovskite Quantum Dots. *Science* **2019**, *363*, 1068−1072.
(250) Nirmal, M.; Murray, C. B.; Bawendi, M. G. Fluorescence-Line Narrowing in CdSe Quantum Dots: Surface Localization of the Photogenerated Exciton. *Phys. Rev. B: Condens. Matter Mater. Phys.* **1994**, *50*, 2293−2300.
(251) Cui, J.; Beyler, A. P.; Marshall, L. F.; Chen, O.; Harris, D. K.; Wanger, D. D.; Brokmann, X.; Bawendi, M. G. Direct Probe of Spectral Inhomogeneity Reveals Synthetic Tunability of Single-Nanocrystal Spectral Linewidths. *Nat. Chem.* **2013**, *5*, 602−606.
(252) Cui, J.; Beyler, A. P.; Coropceanu, I.; Cleary, L.; Avila, T. R.; Chen, Y.; Cordero, J. M.; Heathcote, S. L.; Harris, D. K.; Chen, O.; Cao, J.; Bawendi, M. G. Evolution of the Single-Nanocrystal Photoluminescence Linewidth with Size and Shell: Implications for Exciton-Phonon Coupling and the Optimization of Spectral Linewidths. *Nano Lett.* **2016**, *16*, 289−296.
(253) Empedocles, S. A.; Norris, D. J.; Bawendi, M. G. Photoluminescence Spectroscopy of Single CdSe Nanocrystallite Quantum Dots. *Phys. Rev. Lett.* **1996**, *77*, 3873−3876.
(254) Biadala, L.; Siebers, B.; Beyazit, Y.; Tessier, M. D.; Dupont, D.; Hens, Z.; Yakovlev, D. R.; Bayer, M. Band-Edge Exciton Fine Structure and Recombination Dynamics in InP/ZnS Colloidal Nanocrystals. *ACS Nano* **2016**, *10*, 3356−3364.
(255) Hu, F.; Yin, C.; Zhang, H.; Sun, C.; Yu, W. W.; Zhang, C.; Wang, X.; Zhang, Y.; Xiao, M. Slow Auger Recombination of Charged Excitons in Nonblinking Perovskite Nanocrystals without Spectral Diffusion. *Nano Lett.* **2016**, *16*, 6425−6430.
(256) de Mello Donegá, C.; Bode, M.; Meijerink, A. Size- and Temperature-Dependence of Exciton Lifetimes in CdSe Quantum Dots. *Phys. Rev. B: Condens. Matter Mater. Phys.* **2006**, *74*, 085320.
(257) Nirmal, M.; Norris, D. J.; Kuno, M.; Bawendi, M. G.; Efros, A. L.; Rosen, M. Observation of the 'Dark Exciton' in CdSe Quantum Dots. *Phys. Rev. Lett.* **1995**, *75*, 3728−3731.
(258) Efros, A. L.; Rosen, M. Random Telegraph Signal in the Photoluminescence Intensity of a Single Quantum Dot. *Phys. Rev. Lett.* **1997**, *78*, 1110−1113.
(259) Nirmal, M.; Dabbousi, B. O.; Bawendi, M. G.; Macklin, J. J.; Trautman, J. K.; Harris, T. D.; Brus, L. E. Fluorescence Intermittency in Single Cadmium Selenide Nanocrystals. *Nature* **1996**, *383*, 802−804.
(260) Robel, I.; Gresback, R.; Kortshagen, U.; Schaller, R. D.; Klimov, V. I. Universal Size-Dependent Trend in Auger Recombination in Direct-Gap and Indirect-Gap Semiconductor Nanocrystals. *Phys. Rev. Lett.* **2009**, *102*, 177404.
(261) Yuan, G.; Gómez, D. E.; Kirkwood, N.; Boldt, K.; Mulvaney, P. Two Mechanisms Determine Quantum Dot Blinking. *ACS Nano* **2018**, *12*, 3397−3405.
(262) Klimov, V. I. Multicarrier Interactions in Semiconductor Nanocrystals in Relation to the Phenomena of Auger Recombination and Carrier Multiplication. *Annu. Rev. Condens. Matter Phys.* **2014**, *5*, 285−316.
(263) Klimov, V. I.; Mikhailovsky, A. A.; Xu, S.; Malko, A.; Hollingsworth, J. A.; Leatherdale, C. A.; Eisler, H.; Bawendi, M. G. Optical Gain and Stimulated Emission in Nanocrystal Quantum Dots. *Science (Washington, DC, U. S.)* **2000**, *290*, 314−317.
(264) Lim, J.; Park, Y.-S.; Wu, K.; Yun, H. J.; Klimov, V. I. Droop-Free Colloidal Quantum Dot Light-Emitting Diodes. *Nano Lett.* **2018**, *18*, 6645−6653.
(265) Nozik, A. Quantum Dot Solar Cells. *Phys. E* **2002**, *14*, 115−120.
(266) Chen, Y.; Vela, J.; Htoon, H.; Casson, J. L.; Werder, D. J.; Bussian, D. A.; Klimov, V. I.; Hollingsworth, J. A. Giant" Multishell CdSe Nanocrystal Quantum Dots with Suppressed Blinking. *J. Am. Chem. Soc.* **2008**, *130*, 5026−5027.
(267) Htoon, H.; Malko, A. V.; Bussian, D.; Vela, J.; Chen, Y.; Hollingsworth, J. A.; Klimov, V. I. Highly Emissive Multiexcitons in Steady-State Photoluminescence of Individual "Giant" CdSe/CdS Core/Shell Nanocrystals. *Nano Lett.* **2010**, *10*, 2401−2407.
(268) Mahler, B.; Spinicelli, P.; Buil, S.; Quelin, X.; Hermier, J.-P.; Dubertret, B. Towards Non-Blinking Colloidal Quantum Dots. *Nat. Mater.* **2008**, *7*, 659−664.
(269) Climente, J. I.; Movilla, J. L.; Planelles, J. Auger Recombination Suppression in Nanocrystals with Asymmetric Electron-Hole Confinement. *Small* **2012**, *8*, 754−759.
(270) Cragg, G. E.; Efros, A. L. Suppression of Auger Processes in Confined Structures. *Nano Lett.* **2010**, *10*, 313−317.
(271) Eperon, G. E.; Jedlicka, E.; Ginger, D. S. Biexciton Auger Recombination Differs in Hybrid and Inorganic Halide Perovskite Quantum Dots. *J. Phys. Chem. Lett.* **2018**, *9*, 104−109.
(272) Nasilowski, M.; Spinicelli, P.; Patriarche, G.; Dubertret, B. Gradient CdSe/CdS Quantum Dots with Room Temperature Biexciton Unity Quantum Yield. *Nano Lett.* **2015**, *15*, 3953−3958.
(273) Park, Y.-S.; Bae, W. K.; Padilha, L. A.; Pietryga, J. M.; Klimov, V. I. Effect of the Core/Shell Interface on Auger Recombination Evaluated by Single-Quantum-Dot Spectroscopy. *Nano Lett.* **2014**, *14*, 396−402.
(274) Ithurria, S.; Tessier, M. D.; Mahler, B.; Lobo, R. P. S. M.; Dubertret, B.; Efros, A. L. Colloidal Nanoplatelets with Two-Dimensional Electronic Structure. *Nat. Mater.* **2011**, *10*, 936−941.
(275) Rossinelli, A. A.; Rojo, H.; Mule, A. S.; Aellen, M.; Cocina, A.; De Leo, E.; Schäublin, R.; Norris, D. J. Compositional Grading for Efficient and Narrowband Emission in CdSe-Based Core/Shell Nanoplatelets. *Chem. Mater.* **2019**, *31*, 9567−9578.
(276) Tessier, M. D.; Mahler, B.; Nadal, B.; Heuclin, H.; Pedetti, S.; Dubertret, B. Spectroscopy of Colloidal Semiconductor Core/Shell Nanoplatelets with High Quantum Yield. *Nano Lett.* **2013**, *13*, 3321−3328.
(277) Santori, C.; Fattal, D.; Vučković, J.; Solomon, G. S.; Yamamoto, Y. Indistinguishable Photons from a Single-Photon Device. *Nature* **2002**, *419*, 594−597.
(278) Zwiller, V.; Blom, H.; Jonsson, P.; Panev, N.; Jeppesen, S.; Tsegaye, T.; Goobar, E.; Pistol, M.-E.; Samuelson, L.; Björk, G. Single Quantum Dots Emit Single Photons at a Time: Antibunching Experiments. *Appl. Phys. Lett.* **2001**, *78*, 2476−2478.
(279) Santori, C.; Pelton, M.; Solomon, G.; Dale, Y.; Yamamoto, Y. Triggered Single Photons from a Quantum Dot. *Phys. Rev. Lett.* **2001**, *86*, 1502−1505.
(280) Michler, P.; Kiraz, A.; Becher, C.; Schoenfeld, W. V.; Petroff, P. M.; Zhang, L.; Hu, E.; Imamoglu, A. A Quantum Dot Single-Photon Turnstile Device. *Science* **2000**, *290*, 2282−2285.
(281) Lounis, B.; Orrit, M. Single-Photon Sources. *Rep. Prog. Phys.* **2005**, *68*, 1129−1179.
(282) Michler, P.; Imamoğlu, A.; Mason, M. D.; Carson, P. J.; Strouse, G. F.; Buratto, S. K. Quantum Correlation among Photons from a Single Quantum Dot at Room Temperature. *Nature* **2000**, *406*, 968−970.
(283) Brown, R. H.; Twiss, R. Q. Correlation between Photons in Two Coherent Beams of Light. *Nature* **1956**, *177*, 27−29.
(284) Lounis, B.; Bechtel, H. A.; Gerion, D.; Alivisatos, P.; Moerner, W. E. Photon Antibunching in Single CdSe/ZnS Quantum Dot Fluorescence. *Chem. Phys. Lett.* **2000**, *329*, 399−404.

https://dx.doi.org/10.1021/acs.chemrev.0c00831
Chem. Rev. 2021, 121, 3186−3233

(285) Lin, X.; Dai, X.; Pu, C.; Deng, Y.; Niu, Y.; Tong, L.; Fang, W.; Jin, Y.; Peng, X. Electrically-Driven Single-Photon Sources Based on Colloidal Quantum Dots with near-Optimal Antibunching at Room Temperature. *Nat. Commun.* **2017**, *8*, 1132.
(286) Masia, F.; Accanto, N.; Langbein, W.; Borri, P. Spin-Flip Limited Exciton Dephasing in CdSe/ZnS Colloidal Quantum Dots. *Phys. Rev. Lett.* **2012**, *108*, 087401.
(287) Accanto, N.; Masia, F.; Moreels, I.; Hens, Z.; Langbein, W.; Borri, P. Engineering the Spin-Flip Limited Exciton Dephasing in Colloidal CdSe/CdS Quantum Dots. *ACS Nano* **2012**, *6*, 5227−5233.
(288) Nair, G.; Zhao, J.; Bawendi, M. G. Biexciton Quantum Yield of Single Semiconductor Nanocrystals from Photon Statistics. *Nano Lett.* **2011**, *11*, 1136−1140.
(289) Utzat, H.; Shulenberger, K. E.; Achorn, O. B.; Nasilowski, M.; Sinclair, T. S.; Bawendi, M. G. Probing Linewidths and Biexciton Quantum Yields of Single Cesium Lead Halide Nanocrystals in Solution. *Nano Lett.* **2017**, *17*, 6838−6846.
(290) Bischof, T. S.; Correa, R. E.; Rosenberg, D.; Dauler, E. A.; Bawendi, M. G. Measurement of Emission Lifetime Dynamics and Biexciton Emission Quantum Yield of Individual InAs Colloidal Nanocrystals. *Nano Lett.* **2014**, *14*, 6787−6791.
(291) Benson, O.; Santori, C.; Pelton, M.; Yamamoto, Y. Regulated and Entangled Photons from a Single Quantum Dot. *Phys. Rev. Lett.* **2000**, *84*, 2513−2516.
(292) Stevenson, R. M.; Young, R. J.; Atkinson, P.; Cooper, K.; Ritchie, D. A.; Shields, A. J. A Semiconductor Source of Triggered Entangled Photon Pairs. *Nature* **2006**, *439*, 179−182.
(293) Gupta, J. A.; Awschalom, D. D.; Peng, X.; Alivisatos, A. P. Spin Coherence in Semiconductor Quantum Dots. *Phys. Rev. B: Condens. Matter Mater. Phys.* **1999**, *59*, R10421−R10424.
(294) Gupta, J. A.; Awschalom, D. D.; Efros, A. L.; Rodina, A. V. Spin Dynamics in Semiconductor Nanocrystals. *Phys. Rev. B: Condens. Matter Mater. Phys.* **2002**, *66*, 125307.
(295) Kim, J.; Wong, C. Y.; Scholes, G. D. Exciton Fine Structure and Spin Relaxation in Semiconductor Colloidal Quantum Dots. *Acc. Chem. Res.* **2009**, *42*, 1037−1046.
(296) Fernée, M. J.; Sinito, C.; Tamarat, P.; Lounis, B. State Selective Pumping Reveals Spin-Relaxation Pathways in CdSe Quantum Dots. *Nano Lett.* **2014**, *14*, 4480−4485.
(297) Sze, S. M.; Ng, K. K. *Physics of Semiconductor Devices*, 3rd ed.; John Wiley & Sons: Hoboken, NJ, 2007.
(298) Kim, S.; Fisher, B.; Eisler, H.-J.; Bawendi, M. Type-II Quantum Dots: CdTe/CdSe(Core/Shell) and CdSe/ZnTe(Core/Shell) Heterostructures. *J. Am. Chem. Soc.* **2003**, *125*, 11466−11467.
(299) Wang, L.; Nonaka, K.; Okuhata, T.; Katayama, T.; Tamai, N. Quasi-Type II Carrier Distribution in CdSe/CdS Core/Shell Quantum Dots with Type I Band Alignment. *J. Phys. Chem. C* **2018**, *122*, 12038−12046.
(300) Danek, M.; Jensen, K. F.; Murray, C. B.; Bawendi, M. G. Preparation of II-VI Quantum Dot Composites by Electrospray Organometallic Chemical Vapor Deposition. *J. Cryst. Growth* **1994**, *145*, 714−720.
(301) Danek, M.; Jensen, K. F.; Murray, C. B.; Bawendi, M. G. Electrospray Organometallic Chemical Vapor Deposition—A Novel Technique for Preparation of II-VI Quantum Dot Composites. *Appl. Phys. Lett.* **1994**, *65*, 2795−2797.
(302) Dabbousi, B. O.; Rodriguez-Viejo, J.; Mikulec, F. V.; Heine, J. R.; Mattoussi, H.; Ober, R.; Jensen, K. F.; Bawendi, M. G. (CdSe)ZnS Core-Shell Quantum Dots: Synthesis and Characterization of a Size Series of Highly Luminescent Nanocrystallites. *J. Phys. Chem. B* **1997**, *101*, 9463−9475.
(303) Peng, X.; Schlamp, M. C.; Kadavanich, A. V.; Alivisatos, A. P. Epitaxial Growth of Highly Luminescent CdSe/CdS Core/Shell Nanocrystals with Photostability and Electronic Accessibility. *J. Am. Chem. Soc.* **1997**, *119*, 7019−7029.
(304) Shu, Y.; Lin, X.; Qin, H.; Hu, Z.; Jin, Y.; Peng, X. Quantum Dots for Display Applications. *Angew. Chem., Int. Ed.* **2020**, *59*, 22312−22323.
(305) Wood, V.; Bulović, V. Colloidal Quantum Dot Light-Emitting Devices. *Nano Rev.* **2010**, *1*, 5202.
(306) Adam, S.; Talapin, D. V.; Borchert, H.; Lobo, A.; McGinley, C.; de Castro, A. R. B.; Haase, M.; Weller, H.; Möller, T. The Effect of Nanocrystal Surface Structure on the Luminescence Properties: Photoemission Study of HF-Etched InP Nanocrystals. *J. Chem. Phys.* **2005**, *123*, 084706.
(307) Li, J. J.; Wang, Y. A.; Guo, W.; Keay, J. C.; Mishima, T. D.; Johnson, M. B.; Peng, X. Large-Scale Synthesis of Nearly Monodisperse CdSe/CdS Core/Shell Nanocrystals Using Air-Stable Reagents via Successive Ion Layer Adsorption and Reaction. *J. Am. Chem. Soc.* **2003**, *125*, 12567−12575.
(308) Lambert, K.; Geyter, B.; De Moreels, I.; Hens, Z.; De Geyter, B.; Moreels, I.; Hens, Z. PbTe|CdTe Core|Shell Particles by Cation Exchange, a HR-TEM Study. *Chem. Mater.* **2009**, *21*, 778−780.
(309) Fenton, J. L.; Steimle, B. C.; Schaak, R. E. Exploiting Crystallographic Regioselectivity To Engineer Asymmetric Three-Component Colloidal Nanoparticle Isomers Using Partial Cation Exchange Reactions. *J. Am. Chem. Soc.* **2018**, *140*, 6771−6775.
(310) Casavola, M.; Van Huis, M. A.; Bals, S.; Lambert, K.; Hens, Z.; Vanmaekelbergh, D. Anisotropic Cation Exchange in PbSe/CdSe Core/Shell Nanocrystals of Different Geometry. *Chem. Mater.* **2012**, *24*, 294−302.
(311) Grodzińska, D.; Pietra, F.; Van Huis, M. A.; Vanmaekelbergh, D.; De Mello Donegá, C. Thermally Induced Atomic Reconstruction of PbSe/CdSe Core/Shell Quantum Dots into PbSe/CdSe Bi-Hemisphere Hetero-Nanocrystals. *J. Mater. Chem.* **2011**, *21*, 11556−11565.
(312) Raidongia, K.; Nag, A.; Sundaresan, A.; Rao, C. N. R. Multiferroic and Magnetoelectric Properties of Core-Shell CoFe2O4@BaTiO3 Nanocomposites. *Appl. Phys. Lett.* **2010**, *97*, 062904.
(313) Choi, C. L.; Alivisatos, A. P. From Artificial Atoms to Nanocrystal Molecules: Preparation and Properties of More Complex Nanostructures. *Annu. Rev. Phys. Chem.* **2010**, *61*, 369−389.
(314) Shevchenko, E. V.; Talapin, D. V.; Kotov, N. A.; O'Brien, S.; Murray, C. B. Structural Diversity in Binary Nanoparticle Superlattices. *Nature* **2006**, *439*, 55−59.
(315) Jishkariani, D.; Wu, Y.; Wang, D.; Liu, Y.; van Blaaderen, A.; Murray, C. B. Preparation and Self-Assembly of Dendronized Janus Fe_3O_4-Pt and Fe_3O_4-Au Heterodimers. *ACS Nano* **2017**, *11*, 7958−7966.
(316) Zhu, H.; Fan, Z.; Yuan, Y.; Wilson, M. A.; Hills-Kimball, K.; Wei, Z.; He, J.; Li, R.; Grünwald, M.; Chen, O. Self-Assembly of Quantum Dot-Gold Heterodimer Nanocrystals with Orientational Order. *Nano Lett.* **2018**, *18*, 5049−5056.
(317) Pileni, M. P. Nanocrystal Self-Assemblies: Fabrication and Collective Properties. *J. Phys. Chem. B* **2001**, *105*, 3358−3371.
(318) Buck, M. R.; Schaak, R. E. Emerging Strategies for the Total Synthesis of Inorganic Nanostructures. *Angew. Chem., Int. Ed.* **2013**, *52*, 6154−6178.
(319) Teitelboim, A.; Meir, N.; Kazes, M.; Oron, D. Colloidal Double Quantum Dots. *Acc. Chem. Res.* **2016**, *49*, 902−910.
(320) Hughes, B. K.; Blackburn, J. L.; Kroupa, D.; Shabaev, A.; Erwin, S. C.; Efros, A. L.; Nozik, A. J.; Luther, J. M.; Beard, M. C. Synthesis and Spectroscopy of Pbse Fused Quantum-Dot Dimers. *J. Am. Chem. Soc.* **2014**, *136*, 4670−4679.
(321) Sengupta, S.; Ganguli, N.; Dasgupta, I.; Sarma, D. D.; Acharya, S. Long-Range Visible Fluorescence Tunability Using Component-Modulated Coupled Quantum Dots. *Adv. Mater.* **2011**, *23*, 1998−2003.
(322) Lavieville, R.; Zhang, Y.; Casu, A.; Genovese, A.; Manna, L.; Di Fabrizio, E.; Krahne, R. Charge Transport in Nanoscale "All-Inorganic" Networks of Semiconductor Nanorods Linked by Metal Domains. *ACS Nano* **2012**, *6*, 2940−2947.
(323) Figuerola, A.; Franchini, I. R.; Fiore, A.; Mastria, R.; Falqui, A.; Bertoni, G.; Bals, S.; Van Tendeloo, G.; Kudera, S.; Cingolani, R.; Manna, L. End-to-End Assembly of Shape-Controlled Nanocrystals via a Nanowelding Approach Mediated by Gold Domains. *Adv. Mater.* **2009**, *21*, 550−554.

https://dx.doi.org/10.1021/acs.chemrev.0c00831
Chem. Rev. 2021, 121, 3186−3233

(324) Saruyama, M.; Kanehara, M.; Teranishi, T. CdPd Sulfide Heterostructured Nanoparticles with Metal Sulfide Seed-Dependent Morphologies. *Chem. Commun.* **2009**, No. 19, 2724.
(325) Gupta, S.; Kershaw, S. V.; Rogach, A. L. 25th Anniversary Article: Ion Exchange in Colloidal Nanocrystals. *Adv. Mater.* **2013**, *25*, 6923−6944.
(326) Zhang, J.; Chernomordik, B. D.; Crisp, R. W.; Kroupa, D. M.; Luther, J. M.; Miller, E. M.; Gao, J.; Beard, M. C. Preparation of Cd/Pb Chalcogenide Heterostructured Janus Particles via Controllable Cation Exchange. *ACS Nano* **2015**, *9*, 7151−7163.
(327) Jain, P. K.; Amirav, L.; Aloni, S.; Alivisatos, A. P. Nanoheterostructure Cation Exchange: Anionic Framework Conservation. *J. Am. Chem. Soc.* **2010**, *132*, 9997−9999.
(328) Li, H.; Brescia, R.; Krahne, R.; Bertoni, G.; Alcocer, M. J. P.; D'Andrea, C.; Scotognella, F.; Tassone, F.; Zanella, M.; De Giorgi, M.; Manna, L. Blue-UV-Emitting ZnSe(Dot)/ZnS(Rod) Core/Shell Nanocrystals Prepared from CdSe/CdS Nanocrystals by Sequential Cation Exchange. *ACS Nano* **2012**, *6*, 1637−1647.
(329) Li, M.; Yu, X.-F.; Liang, S.; Peng, X.-N.; Yang, Z.-J.; Wang, Y.-L.; Wang, Q.-Q. Synthesis of Au-CdS Core-Shell Hetero-Nanorods with Efficient Exciton-Plasmon Interactions. *Adv. Funct. Mater.* **2011**, *21*, 1788−1794.
(330) Saruyama, M.; So, Y.-G.; Kimoto, K.; Taguchi, S.; Kanemitsu, Y.; Teranishi, T. Spontaneous Formation of Wurzite-CdS/Zinc Blende-CdTe Heterodimers through a Partial Anion Exchange Reaction. *J. Am. Chem. Soc.* **2011**, *133*, 17598−17601.
(331) Xie, Y.; Qian, Y.; Zhang, S.; Xie, Y.; Yan, P.; Lu, J. CdS/CdSe Core/Sheath Nanostructures Obtained from CdS Nanowires. *Chem. Commun.* **1999**, No. 19, 1969−1970.
(332) Koktysh, D. S.; McBride, J. R.; Dixit, S. K.; Feldman, L. C.; Rosenthal, S. J. PbS/PbSe Structures with Core-Shell Type Morphology Synthesized from PbS Nanocrystals. *Nanotechnology* **2007**, *18*, 495607.
(333) Crooker, S. A.; Barrick, T.; Hollingsworth, J. A.; Klimov, V. I. Multiple Temperature Regimes of Radiative Decay in CdSe Nanocrystal Quantum Dots: Intrinsic Limits to the Dark-Exciton Lifetime. *Appl. Phys. Lett.* **2003**, *82*, 2793−2795.
(334) Brovelli, S.; Schaller, R. D.; Crooker, S. A.; García-Santamaría, F.; Chen, Y.; Viswanatha, R.; Hollingsworth, J. A.; Htoon, H.; Klimov, V. I. Nano-Engineered Electron-Hole Exchange Interaction Controls Exciton Dynamics in Core-Shell Semiconductor Nanocrystals. *Nat. Commun.* **2011**, *2*, 280.
(335) Ochsenbein, S. T.; Gamelin, D. R. Quantum Oscillations in Magnetically Doped Colloidal Nanocrystals. *Nat. Nanotechnol.* **2011**, *6*, 112−115.
(336) Nandan, Y.; Mehata, M. S. Wavefunction Engineering of Type-I/Type-II Excitons of CdSe/CdS Core-Shell Quantum Dots. *Sci. Rep.* **2019**, *9*, 2.
(337) Kroupa, D. M.; Pach, G. F.; Vörös, M.; Giberti, F.; Chernomordik, B. D.; Crisp, R. W.; Nozik, A. J.; Johnson, J. C.; Singh, R.; Klimov, V. I.; Galli, G.; Beard, M. C. Enhanced Multiple Exciton Generation in PbS|CdS Janus-like Heterostructured Nanocrystals. *ACS Nano* **2018**, *12*, 10084−10094.
(338) Cirloganu, C. M.; Padilha, L. A.; Lin, Q.; Makarov, N. S.; Velizhanin, K. A.; Luo, H.; Robel, I.; Pietryga, J. M.; Klimov, V. I. Enhanced Carrier Multiplication in Engineered Quasi-Type-II Quantum Dots. *Nat. Commun.* **2014**, *5*, 4148.
(339) Cui, J.; Panfil, Y. E.; Koley, S.; Shamalia, D.; Waiskopf, N.; Remennik, S.; Popov, I.; Oded, M.; Banin, U. Colloidal Quantum Dot Molecules Manifesting Quantum Coupling at Room Temperature. *Nat. Commun.* **2019**, *10*, 5401.
(340) Van Schooten, K. J.; Huang, J.; Baker, W. J.; Talapin, D. V.; Boehme, C.; Lupton, J. M. Spin-Dependent Exciton Quenching and Spin Coherence in CdSe/CdS Nanocrystals. *Nano Lett.* **2013**, *13*, 65−71.
(341) Fowler, W. B. *Physics of Color Centers*; Academic Press: New York, 1968.
(342) Henderson, B.; Imbusch, G. F. *Optical Spectroscopy of Inorganic Solids*; Clarendon Press: 1989.
(343) Zaitsev, A.; Alexandr, M. *Optical Properties of Diamond: A Data Handbook*; Springer: Berlin, Heidelberg, 2001.
(344) Yen, W. M.; William, M.; Shionoya, S.; Yamamoto, H. *Phosphor Handbook*; CRC Press/Taylor and Francis: 2007.
(345) Vij, D. R. *Handbook of Electroluminescent Materials*; Institute of Physics: Great Britain, 2004.
(346) Stoneham, A. M. *Theory of Defects in Solids: Electronic Structure of Defects in Insulators and Semiconductors*; Clarendon Press: 2001.
(347) Doherty, M. W.; Manson, N. B.; Delaney, P.; Jelezko, F.; Wrachtrup, J.; Hollenberg, L. C. L. The Nitrogen-Vacancy Colour Centre in Diamond. *Phys. Rep.* **2013**, *528*, 1−45.
(348) Tanabe, Y.; Sugano, S. On the Absorption Spectra of Complex Ions II. *J. Phys. Soc. Jpn.* **1954**, *9*, 766−779.
(349) Coulson, A.; Kearsley, M. J. Colour Centres in Irradiated Diamonds. I. *Proc. R. Soc. London. Ser. A: Math. Phys. Sci.* **1957**, *241*, 433−454.
(350) Maze, J. R.; Gali, A.; Togan, E.; Chu, Y.; Trifonov, A.; Kaxiras, E.; Lukin, M. D. Properties of Nitrogen-Vacancy Centers in Diamond: The Group Theoretic Approach. *New J. Phys.* **2011**, *13*, 025025.
(351) Doherty, M. W.; Manson, N. B.; Delaney, P.; Hollenberg, L. C. L. The Negatively Charged Nitrogen-Vacancy Centre in Diamond: The Electronic Solution. *New J. Phys.* **2011**, *13*, 025019.
(352) Manson, N. B.; Harrison, J. P.; Sellars, M. J. Nitrogen-Vacancy Center in Diamond: Model of the Electronic Structure and Associated Dynamics. *Phys. Rev. B: Condens. Matter Mater. Phys.* **2006**, *74*, 104303.
(353) Acosta, V. M.; Jarmola, A.; Bauch, E.; Budker, D. Optical Properties of the Nitrogen-Vacancy Singlet Levels in Diamond. *Phys. Rev. B: Condens. Matter Mater. Phys.* **2010**, *82*, 201202.
(354) Kushida, T.; Tanaka, Y.; Oka, Y. Excited-State Absorption Spectra of ZnS: Mn. *Solid State Commun.* **1974**, *14*, 617−620.
(355) Tanaka, M.; Qi, J.; Masumoto, Y. Comparison of Energy Levels of Mn2+ in Nanosized- and Bulk-ZnS Crystals. *J. Lumin.* **2000**, *87*−*89*, 472−474.
(356) Tuan, N. T.; Trung, D. Q.; Quang, N. V.; Hung, N. D.; Khoi, N. T.; Huy, P. T.; Smet, P. F.; Meert, K. W.; Poelman, D. Excitation Energy Dependence of the Life Time of Orange Emission from Mn-Doped ZnS Nanocrystals. *J. Lumin.* **2018**, *199*, 39−44.
(357) Bryan, J. D.; Gamelin, D. R. Doped Semiconductor Nanocrystals: Synthesis, Characterization, Physical Properties, and Applications. *Prog. Inorg. Chem.* **2005**, *54*, 47−126.
(358) Norman, T. J.; Magana, D.; Wilson, T.; Burns, C.; Zhang, J. Z.; Cao, D.; Bridges, F. Optical and Surface Structural Properties of Mn 2+ -Doped ZnSe Nanoparticles. *J. Phys. Chem. B* **2003**, *107*, 6309−6317.
(359) Pearton, S. Doped Nanostructures. *Nanoscale* **2010**, *2*, 1057.
(360) Sooklal, K.; Cullum, B. S.; Angel, S. M.; Murphy, C. J. Photophysical Properties of ZnS Nanoclusters with Spatially Localized Mn $^{2+}$. *J. Phys. Chem.* **1996**, *100*, 4551−4555.
(361) Norris, D. J.; Efros, A. L.; Erwin, S. C. Doped Nanocrystals. *Science* **2008**, *319*, 1776−1779.
(362) Kagan, C. R.; Lifshitz, E.; Sargent, E. H.; Talapin, D. V. Building Devices from Colloidal Quantum Dots. *Science* **2016**, *353*, No. aac5523.
(363) Kramer, N. J.; Schramke, K. S.; Kortshagen, U. R. Plasmonic Properties of Silicon Nanocrystals Doped with Boron and Phosphorus. *Nano Lett.* **2015**, *15*, 5597−5603.
(364) Pradhan, N.; Das Adhikari, S.; Nag, A.; Sarma, D. D. Luminescence, Plasmonic, and Magnetic Properties of Doped Semiconductor Nanocrystals. *Angew. Chem., Int. Ed.* **2017**, *56*, 7038−7054.
(365) Nag, A.; Chakraborty, S.; Sarma, D. D. To Dope Mn $^{2+}$ in a Semiconducting Nanocrystal. *J. Am. Chem. Soc.* **2008**, *130*, 10605−10611.
(366) Norris, D. J.; Yao, N.; Charnock, F. T.; Kennedy, T. A. High-Quality Manganese-Doped ZnSe Nanocrystals. *Nano Lett.* **2001**, *1*, 3−7.
(367) Pradhan, N.; Sarma, D. D. Advances in Light-Emitting Doped Semiconductor Nanocrystals. *J. Phys. Chem. Lett.* **2011**, *2*, 2818−2826.
(368) Corrado, C.; Hawker, M.; Livingston, G.; Medling, S.; Bridges, F.; Zhang, J. Z. Enhanced Cu Emission in ZnS: Cu,Cl/ZnS Core-Shell Nanocrystals. *Nanoscale* **2010**, *2*, 1213.

https://dx.doi.org/10.1021/acs.chemrev.0c00831
Chem. Rev. 2021, 121, 3186−3233

(369) Erwin, S. C.; Zu, L.; Haftel, M. I.; Efros, A. L.; Kennedy, T. A.; Norris, D. J. Doping Semiconductor Nanocrystals. *Nature* **2005**, *436*, 91−94.
(370) Srivastava, B. B.; Jana, S.; Pradhan, N. Doping Cu in Semiconductor Nanocrystals: Some Old and Some New Physical Insights. *J. Am. Chem. Soc.* **2011**, *133*, 1007−1015.
(371) Yang, Y.; Chen, O.; Angerhofer, A.; Cao, Y. C. Radial-Position-Controlled Doping in CdS/ZnS Core/Shell Nanocrystals. *J. Am. Chem. Soc.* **2006**, *128*, 12428−12429.
(372) Pradhan, N.; Goorskey, D.; Thessing, J.; Peng, X. An Alternative of CdSe Nanocrystal Emitters: Pure and Tunable Impurity Emissions in ZnSe Nanocrystals. *J. Am. Chem. Soc.* **2005**, *127*, 17586−17587.
(373) Yuhas, B. D.; Zitoun, D. O.; Pauzauskie, P. J.; He, R.; Yang, P. Transition-Metal Doped Zinc Oxide Nanowires. *Angew. Chem., Int. Ed.* **2006**, *45*, 420−423.
(374) Pk, J.; K, M.; Jh, E.; Sl, W.; Ja, F.; Ap, A. Doped Nanocrystals as Plasmonic Probes of Redox Chemistry. *Angew. Chem., Int. Ed. Engl.* **2013**, *52*, 13671−13675.
(375) Lu, C.-H.; Biesold-McGee, G. V.; Liu, Y.; Kang, Z.; Lin, Z. Doping and Ion Substitution in Colloidal Metal Halide Perovskite Nanocrystals. *Chem. Soc. Rev.* **2020**, *49*, 4953−5007.
(376) Creutz, S. E.; Fainblat, R.; Kim, Y.; De Siena, M. C.; Gamelin, D. R. A Selective Cation Exchange Strategy for the Synthesis of Colloidal Yb^{3+} -Doped Chalcogenide Nanocrystals with Strong Broadband Visible Absorption and Long-Lived Near-Infrared Emission. *J. Am. Chem. Soc.* **2017**, *139*, 11814−11824.
(377) Schimpf, A. M.; Knowles, K. E.; Carroll, G. M.; Gamelin, D. R. Electronic Doping and Redox-Potential Tuning in Colloidal Semiconductor Nanocrystals. *Acc. Chem. Res.* **2015**, *48*, 1929−1937.
(378) Hanif, K. M.; Meulenberg, R. W.; Strouse, G. F. Magnetic Ordering in Doped Cd 1 - x Co x Se Diluted Magnetic Quantum Dots. *J. Am. Chem. Soc.* **2002**, *124*, 11495−11502.
(379) Grandhi, G. K.; Tomar, R.; Viswanatha, R. Study of Surface and Bulk Electronic Structure of II-VI Semiconductor Nanocrystals Using Cu as a Nanosensor. *ACS Nano* **2012**, *6*, 9751−9763.
(380) Chen, D.; Viswanatha, R.; Ong, G. L.; Xie, R.; Balasubramaninan, M.; Peng, X. Temperature Dependence of 'Elementary Processes' in Doping Semiconductor Nanocrystals. *J. Am. Chem. Soc.* **2009**, *131*, 9333−9339.
(381) Santiago-González, B.; Monguzzi, A.; Pinchetti, V.; Casu, A.; Prato, M.; Lorenzi, R.; Campione, M.; Chiodini, N.; Santambrogio, C.; Meinardi, F.; Manna, L.; Brovelli, S. Quantized" Doping of Individual Colloidal Nanocrystals Using Size-Focused Metal Quantum Clusters. *ACS Nano* **2017**, *11*, 6233−6242.
(382) Kennedy, T. A.; Glaser, E. R.; Klein, P. B.; Bhargava, R. N. Symmetry and Electronic Structure of the Mn Impurity in ZnS Nanocrystals. *Phys. Rev. B: Condens. Matter Mater. Phys.* **1995**, *52*, R14356−R14359.
(383) Radovanovic, P. V.; Gamelin, D. R. Electronic Absorption Spectroscopy of Cobalt Ions in Diluted Magnetic Semiconductor Quantum Dots: Demonstration of an Isocrystalline Core/Shell Synthetic Method. *J. Am. Chem. Soc.* **2001**, *123*, 12207−12214.
(384) Hoffman, D. M.; Meyer, B. K.; Ekimov, A. I.; Merkulov, I. A.; Efros, A. L.; Rosen, M.; Couino, G.; Gacoin, T.; Boilot, J. P. Giant Internal Magnetic Fields in Mn Doped Nanocrystal Quantum Dots. *Solid State Commun.* **2000**, *114*, 547−550.
(385) Shao, H.; Wang, C.; Xu, S.; Jiang, Y.; Shao, Y.; Bo, F.; Wang, Z.; Cui, Y. Hydrazine-Promoted Sequential Cation Exchange: A Novel Synthesis Method for Doped Ternary Semiconductor Nanocrystals with Tunable Emission. *Nanotechnology* **2014**, *25*, 025603.
(386) Sun, X.; Huang, X.; Guo, J.; Zhu, W.; Ding, Y.; Niu, G.; Wang, A.; Kiesewetter, D. O.; Wang, Z. L.; Sun, S.; Chen, X. Self-Illuminating ^{64}Cu-Doped CdSe/ZnS Nanocrystals for in Vivo Tumor Imaging. *J. Am. Chem. Soc.* **2014**, *136*, 1706−1709.
(387) Eilers, J.; Groeneveld, E.; de Mello Donegá, C.; Meijerink, A. Optical Properties of Mn-Doped ZnTe Magic Size Nanocrystals. *J. Phys. Chem. Lett.* **2012**, *3*, 1663−1667.
(388) Oh, S. J.; Kim, D. K.; Kagan, C. R. Remote Doping and Schottky Barrier Formation in Strongly Quantum Confined Single PbSe Nanowire Field-Effect Transistors. *ACS Nano* **2012**, *6*, 4328−4334.
(389) Kagan, C. R.; Murray, C. B. Charge Transport in Strongly Coupled Quantum Dot Solids. *Nat. Nanotechnol.* **2015**, *10*, 1013−1026.
(390) Kagan, C. R. Flexible Colloidal Nanocrystal Electronics. *Chem. Soc. Rev.* **2019**, *48*, 1626−1641.
(391) Koleilat, G. I.; Levina, L.; Shukla, H.; Myrskog, S. H.; Hinds, S.; Pattantyus-Abraham, A. G.; Sargent, E. H. Efficient, Stable Infrared Photovoltaics Based on Solution-Cast Colloidal Quantum Dots. *ACS Nano* **2008**, *2*, 833−840.
(392) Ihly, R.; Tolentino, J.; Liu, Y.; Gibbs, M.; Law, M. The Photothermal Stability of PbS Quantum Dot Solids. *ACS Nano* **2011**, *5*, 8175−8186.
(393) Tang, J.; Brzozowski, L.; Barkhouse, D. A. R.; Wang, X.; Debnath, R.; Wolowiec, R.; Palmiano, E.; Levina, L.; Pattantyus-Abraham, A. G.; Jamakosmanovic, D.; Sargent, E. H. Quantum Dot Photovoltaics in the Extreme Quantum Confinement Regime: The Surface-Chemical Origins of Exceptional Air- and Light-Stability. *ACS Nano* **2010**, *4*, 869−878.
(394) Talapin, D. V.; Murray, C. B. PbSe Nanocrystal Solids for N- and p-Channel Thin Film Field-Effect Transistors. *Science* **2005**, *310*, 86−89.
(395) Kim, D. K.; Vemulkar, T. R.; Oh, S. J.; Koh, W.-K.; Murray, C. B.; Kagan, C. R. Ambipolar and Unipolar PbSe Nanowire Field-Effect Transistors. *ACS Nano* **2011**, *5*, 3230−3236.
(396) Choi, J.-H.; Oh, S. J. S. J.; Lai, Y.; Kim, D. K. D. K.; Zhao, T.; Fafarman, A. T. A. T.; Diroll, B. T. B. T.; Murray, C. B. C. B.; Kagan, C. R. C. R. In Situ Repair of High-Performance, Flexible Nanocrystal Electronics for Large-Area Fabrication and Operation in Air. *ACS Nano* **2013**, *7*, 8275−8283.
(397) Leschkies, K. S.; Kang, M. S.; Aydil, E. S.; Norris, D. J. Influence of Atmospheric Gases on the Electrical Properties of PbSe Quantum-Dot Films. *J. Phys. Chem. C* **2010**, *114*, 9988−9996.
(398) Oh, S. J. S. J.; Berry, N. E. N. E.; Choi, J.-H. H.; Gaulding, E. A. A.; Paik, T.; Hong, S.-H. H. S.-H.; Murray, C. B. C. B.; Kagan, C. R. C. R. Stoichiometric Control of Lead Chalcogenide Nanocrystal Solids to Enhance Their Electronic and Optoelectronic Device Performance. *ACS Nano* **2013**, *7*, 2413−2421.
(399) Luther, J. M.; Pietryga, J. M. Stoichiometry Control in Quantum Dots: A Viable Analog to Impurity Doping of Bulk Materials. *ACS Nano* **2013**, *7*, 1845−1849.
(400) Kim, D.; Kim, D.-H.; Lee, J.-H.; Grossman, J. C. Impact of Stoichiometry on the Electronic Structure of PbS Quantum Dots. *Phys. Rev. Lett.* **2013**, *110*, 196802.
(401) Oh, S. J. S. J.; Berry, N. E. N. E.; Choi, J.-H.; Gaulding, E. A. A.; Lin, H.; Paik, T.; Diroll, B. T. B. T.; Muramoto, S.; Murray, C. B. C. B.; Kagan, C. R. C. R. Designing High-Performance PbS and PbSe Nanocrystal Electronic Devices through Stepwise, Post-Synthesis, Colloidal Atomic Layer Deposition. *Nano Lett.* **2014**, *14*, 1559−1566.
(402) Kim, D. K.; Fafarman, A. T.; Diroll, B. T.; Chan, S. H.; Gordon, T. R.; Murray, C. B.; Kagan, C. R. Solution-Based Stoichiometric Control over Charge Transport in Nanocrystalline CdSe Devices. *ACS Nano* **2013**, *7*, 8760−8770.
(403) Bekenstein, Y.; Vinokurov, K.; Keren-Zur, S.; Hadar, I.; Schilt, Y.; Raviv, U.; Millo, O.; Banin, U. Thermal Doping by Vacancy Formation in Copper Sulfide Nanocrystal Arrays. *Nano Lett.* **2014**, *14*, 1349−1353.
(404) Scotognella, F.; Della Valle, G.; Srimath Kandada, A. R.; Dorfs, D.; Zavelani-Rossi, M.; Conforti, M.; Miszta, K.; Comin, A.; Korobchevskaya, K.; Lanzani, G.; Manna, L.; Tassone, F. Plasmon Dynamics in Colloidal Cu_2-XSe Nanocrystals. *Nano Lett.* **2011**, *11*, 4711−4717.
(405) Luther, J. M.; Jain, P. K.; Ewers, T.; Alivisatos, A. P. Localized Surface Plasmon Resonances Arising from Free Carriers in Doped Quantum Dots. *Nat. Mater.* **2011**, *10*, 361−366.
(406) Yu, D.; Wang, C.; Guyot-Sionnest, P. N-Type Conducting CdSe Nanocrystal Solids. *Science* **2003**, *300*, 1277−1280.

https://dx.doi.org/10.1021/acs.chemrev.0c00831
Chem. Rev. 2021, 121, 3186−3233

(407) Wang, C.; Shim, M.; Guyot-Sionnest, P. Electrochromic Nanocrystal Quantum Dots. *Science* **2001**, *291*, 2390−2392.
(408) Wehrenberg, B. L.; Guyot-Sionnest, P. Electron and Hole Injection in PbSe Quantum Dot Films. *J. Am. Chem. Soc.* **2003**, *125*, 7806−7807.
(409) Koh, W.; Koposov, A. Y.; Stewart, J. T.; Pal, B. N.; Robel, I.; Pietryga, J. M.; Klimov, V. I. Heavily Doped N-Type PbSe and PbS Nanocrystals Using Ground-State Charge Transfer from Cobaltocene. *Sci. Rep.* **2013**, *3*, 2004.
(410) Choi, J.-H. H.; Fafarman, A. T.; Oh, S. J.; Ko, D.-K. K.; Kim, D. K.; Diroll, B. T.; Muramoto, S.; Gillen, G.; Murray, C. B.; Kagan, C. R.; Gillen, J. G.; Murray, C. B.; Kagan, C. R. Band-like Transport in Strongly-Coupled and Doped Quantum Dot Solids: A Route to High-Performance Thin-Film Electronics. *Nano Lett.* **2012**, *12*, 2631−2638.
(411) Choi, J.-H.; Wang, H.; Oh, S. J.; Paik, T.; Jo, P. S.; Sung, J.; Ye, X.; Zhao, T.; Diroll, B. T.; Murray, C. B.; Kagan, C. R. Exploiting the Colloidal Nanocrystal Library to Construct Electronic Devices. *Science* **2016**, *352*, 205−208.
(412) Lee, W. S.; Kang, Y. G.; Woo, H. K.; Ahn, J.; Kim, H.; Kim, D.; Jeon, S.; Han, M. J.; Choi, J.-H.; Oh, S. J. Designing High-Performance CdSe Nanocrystal Thin-Film Transistors Based on Solution Process of Simultaneous Ligand Exchange, Trap Passivation, and Doping. *Chem. Mater.* **2019**, *31*, 9389−9399.
(413) Urban, J. J.; Talapin, D. V.; Shevchenko, E. V.; Kagan, C. R.; Murray, C. B. Synergism in Binary Nanocrystal Superlattices Leads to Enhanced P-Type Conductivity in Self-Assembled PbTe/Ag_2 Te Thin Films. *Nat. Mater.* **2007**, *6*, 115−121.
(414) Bube, R. H. *Photoelectronic Properties of Semiconductors*; Cambridge University Press: 1992.
(415) Samarth, N.; Furdyna, J. K. Diluted Magnetic Semiconductors. *MRS Bull.* **1988**, *13*, 32−36.
(416) Raha, M.; Chen, S.; Phenicie, C. M.; Ourari, S.; Dibos, A. M.; Thompson, J. D. Optical Quantum Nondemolition Measurement of a Single Rare Earth Ion Qubit. *Nat. Commun.* **2020**, *11*, 1605.
(417) Haase, M.; Schäfer, H. Upconverting Nanoparticles. *Angew. Chem., Int. Ed.* **2011**, *50*, 5808−5829.
(418) Godlewski, M.; Yatsunenko, S.; Khachapuridze, A.; Ivanov, V. Y.; Gołacki, Z.; Karczewski, G.; Bergman, P. J.; Klar, P. J.; Heimbrodt, W.; Phillips, M. R. Mechanism of Intra-Shell Recombination of Transition Metal and Rare Earth Ions in Nanostructures of II-VI Compounds. *J. Alloys Compd.* **2004**, *380*, 45−49.
(419) Bacher, G.; Schömig, H.; Scheibner, M.; Forchel, A.; Maksimov, A. A.; Chernenko, A. V.; Dorozhkin, P. S.; Kulakovskii, V. D.; Kennedy, T.; Reinecke, T. L. Spin-Spin Interaction in Magnetic Semiconductor Quantum Dots. *Phys. E* **2005**, *26*, 37−44.
(420) Bol, A. A.; Meijerink, A. Long-Lived Mn2+ Emission in Nanocrystalline ZnS:Mn2+. *Phys. Rev. B: Condens. Matter Mater. Phys.* **1998**, *58*, R15997−R16000.
(421) Bhargava, R. N.; Gallagher, D.; Hong, X.; Nurmikko, A. Optical Properties of Manganese-Doped Nanocrystals of ZnS. *Phys. Rev. Lett.* **1994**, *72*, 416−419.
(422) Hu, H.; Zhang, W. Synthesis and Properties of Transition Metals and Rare-Earth Metals Doped ZnS Nanoparticles. *Opt. Mater. (Amsterdam, Neth.)* **2006**, *28*, 536−550.
(423) Wu, P.; Yan, X.-P. Doped Quantum Dots for Chemo/Biosensing and Bioimaging. *Chem. Soc. Rev.* **2013**, *42*, 5489.
(424) Vlaskin, V. A.; Janssen, N.; van Rijssel, J.; Beaulac, R.; Gamelin, D. R. Tunable Dual Emission in Doped Semiconductor Nanocrystals. *Nano Lett.* **2010**, *10*, 3670−3674.
(425) Bowers, M. J. I.; McBride, J. R.; Rosenthal, S. J. White-Light Emission from Magic-Sized Cadmium Selenide Nanocrystals. *J. Am. Chem. Soc.* **2005**, *127*, 15378−15379.
(426) Panda, S. K.; Hickey, S. G.; Demir, H. V.; Eychmüller, A. Bright White-Light Emitting Manganese and Copper Co-Doped ZnSe Quantum Dots. *Angew. Chem., Int. Ed.* **2011**, *50*, 4432−4436.
(427) Pramanik, S.; Bhandari, S.; Roy, S.; Chattopadhyay, A. Synchronous Tricolor Emission-Based White Light from Quantum Dot Complex. *J. Phys. Chem. Lett.* **2015**, *6*, 1270−1274.
(428) Knowles, K. E.; Hartstein, K. H.; Kilburn, T. B.; Marchioro, A.; Nelson, H. D.; Whitham, P. J.; Gamelin, D. R. Luminescent Colloidal Semiconductor Nanocrystals Containing Copper: Synthesis, Photophysics, and Applications. *Chem. Rev.* **2016**, *116*, 10820−10851.
(429) Tanaka, M. Photoluminescence Properties of Mn2+-Doped II-VI Semiconductor Nanocrystals. *J. Lumin.* **2002**, *100*, 163−173.
(430) Li, Y.; Li, Y.; Wang, R.; Xu, Y.; Zheng, W. Enhancing Upconversion Luminescence by Annealing Processes and the High-Temperature Sensing of ZnO:Yb/Tm Nanoparticles. *New J. Chem.* **2017**, *41*, 7116−7122.
(431) Chen, W.; Joly, A. G.; Malm, J.-O.; Bovin, J.-O. Upconversion Luminescence of Eu3+ and Mn2+ in ZnS:Mn2+, Eu3+ Codoped Nanoparticles. *J. Appl. Phys.* **2004**, *95*, 667−672.
(432) Robledo, L.; Childress, L.; Bernien, H.; Hensen, B.; Alkemade, P. F. A.; Hanson, R. High-Fidelity Projective Read-out of a Solid-State Spin Quantum Register. *Nature* **2011**, *477*, 574−578.
(433) Sukachev, D. D.; Sipahigil, A.; Nguyen, C. T.; Bhaskar, M. K.; Evans, R. E.; Jelezko, F.; Lukin, M. D. Silicon-Vacancy Spin Qubit in Diamond: A Quantum Memory Exceeding 10 Ms with Single-Shot State Readout. *Phys. Rev. Lett.* **2017**, *119*, 223602.
(434) Koehl, W. F.; Buckley, B. B.; Heremans, F. J.; Calusine, G.; Awschalom, D. D. Room Temperature Coherent Control of Defect Spin Qubits in Silicon Carbide. *Nature* **2011**, *479*, 84−87.
(435) Widmann, M.; Lee, S.-Y.; Rendler, T.; Son, N. T.; Fedder, H.; Paik, S.; Yang, L.-P.; Zhao, N.; Yang, S.; Booker, I.; Denisenko, A.; Jamali, M.; Momenzadeh, S. A.; Gerhardt, I.; Ohshima, T.; Gali, A.; Janzén, E.; Wrachtrup, J. Coherent Control of Single Spins in Silicon Carbide at Room Temperature. *Nat. Mater.* **2015**, *14*, 164−168.
(436) Christle, D. J.; Falk, A. L.; Andrich, P.; Klimov, P. V.; Hassan, J. U.; Son, N. T.; Janzén, E.; Ohshima, T.; Awschalom, D. D. Isolated Electron Spins in Silicon Carbide with Millisecond Coherence Times. *Nat. Mater.* **2015**, *14*, 160−163.
(437) Zhong, T.; Goldner, P. Emerging Rare-Earth Doped Material Platforms for Quantum Nanophotonics. *Nanophotonics* **2019**, *8*, 2003−2015.
(438) Robledo, L.; Bernien, H.; van Weperen, I.; Hanson, R. Control and Coherence of the Optical Transition of Single Nitrogen Vacancy Centers in Diamond. *Phys. Rev. Lett.* **2010**, *105*, 177403.
(439) Fu, K.-M. C.; Santori, C.; Barclay, P. E.; Rogers, L. J.; Manson, N. B.; Beausoleil, R. G. Observation of the Dynamic Jahn-Teller Effect in the Excited States of Nitrogen-Vacancy Centers in Diamond. *Phys. Rev. Lett.* **2009**, *103*, 256404.
(440) Alkauskas, A.; Buckley, B. B.; Awschalom, D. D.; Van de Walle, C. G. First-Principles Theory of the Luminescence Lineshape for the Triplet Transition in Diamond NV Centres. *New J. Phys.* **2014**, *16*, 073026.
(441) Bassett, L. C.; Heremans, F. J.; Yale, C. G.; Buckley, B. B.; Awschalom, D. D. Electrical Tuning of Single Nitrogen-Vacancy Center Optical Transitions Enhanced by Photoinduced Fields. *Phys. Rev. Lett.* **2011**, *107*, 266403.
(442) Batalov, A.; Jacques, V.; Kaiser, F.; Siyushev, P.; Neumann, P.; Rogers, L. J.; McMurtrie, R. L.; Manson, N. B.; Jelezko, F.; Wrachtrup, J. Low Temperature Studies of the Excited-State Structure of Negatively Charged Nitrogen-Vacancy Color Centers in Diamond. *Phys. Rev. Lett.* **2009**, *102*, 195506.
(443) Bergquist, J. C.; Hulet, R. G.; Itano, W. M.; Wineland, D. J. Observation of Quantum Jumps in a Single Atom. *Phys. Rev. Lett.* **1986**, *57*, 1699−1702.
(444) Sauter, T.; Neuhauser, W.; Blatt, R.; Toschek, P. E. Observation of Quantum Jumps. *Phys. Rev. Lett.* **1986**, *57*, 1696−1698.
(445) Nagourney, W.; Sandberg, J.; Dehmelt, H. Shelved Optical Electron Amplifier: Observation of Quantum Jumps. *Phys. Rev. Lett.* **1986**, *56*, 2797−2799.
(446) Nagy, R.; Niethammer, M.; Widmann, M.; Chen, Y.-C.; Udvarhelyi, P.; Bonato, C.; Hassan, J. U.; Karhu, R.; Ivanov, I. G.; Son, N. T.; Maze, J. R.; Ohshima, T.; Soykal, Ö. O.; Gali, Á.; Lee, S.-Y.; Kaiser, F.; Wrachtrup, J. High-Fidelity Spin and Optical Control of Single Silicon-Vacancy Centres in Silicon Carbide. *Nat. Commun.* **2019**, *10*, 1954.

https://dx.doi.org/10.1021/acs.chemrev.0c00831
Chem. Rev. 2021, 121, 3186−3233

(447) Marian, C. M. Spin-Orbit Coupling and Intersystem Crossing in Molecules. *Wiley Interdiscip. Rev. Comput. Mol. Sci.* **2012**, *2*, 187−203.
(448) Thiering, G.; Gali, A. Theory of the Optical Spin-Polarization Loop of the Nitrogen-Vacancy Center in Diamond. *Phys. Rev. B: Condens. Matter Mater. Phys.* **2018**, *98*, 085207.
(449) Goldman, M. L. L.; Sipahigil, A.; Doherty, M. W. W.; Yao, N. Y. Y.; Bennett, S. D. D.; Markham, M.; Twitchen, D. J. J.; Manson, N. B. B.; Kubanek, A.; Lukin, M. D. D. Phonon-Induced Population Dynamics and Intersystem Crossing in Nitrogen-Vacancy Centers. *Phys. Rev. Lett.* **2015**, *114*, 145502.
(450) Hopper, D.; Shulevitz, H.; Bassett, L. Spin Readout Techniques of the Nitrogen-Vacancy Center in Diamond. *Micromachines* **2018**, *9*, 437.
(451) Exarhos, A. L.; Hopper, D. A.; Patel, R. N.; Doherty, M. W.; Bassett, L. C. Magnetic-Field-Dependent Quantum Emission in Hexagonal Boron Nitride at Room Temperature. *Nat. Commun.* **2019**, *10*, 222.
(452) Gottscholl, A.; Kianinia, M.; Soltamov, V.; Orlinskii, S.; Mamin, G.; Bradac, C.; Kasper, C.; Krambrock, K.; Sperlich, A.; Toth, M.; Aharonovich, I.; Dyakonov, V. Initialization and Read-out of Intrinsic Spin Defects in a van Der Waals Crystal at Room Temperature. *Nat. Mater.* **2020**, *19*, 540−545.
(453) Morfa, A. J.; Gibson, B. C.; Karg, M.; Karle, T. J.; Greentree, A. D.; Mulvaney, P.; Tomljenovic-Hanic, S. Single-Photon Emission and Quantum Characterization of Zinc Oxide Defects. *Nano Lett.* **2012**, *12*, 949−954.
(454) Stewart, C.; Kianinia, M.; Previdi, R.; Tran, T. T.; Aharonovich, I.; Bradac, C.; Bradac, C. Quantum Emission from Localized Defects in Zinc Sulfide. *Opt. Lett.* **2019**, *44*, 4873.
(455) Berhane, A. M.; Jeong, K.-Y.; Bodrog, Z.; Fiedler, S.; Schröder, T.; Triviño, N. V.; Palacios, T.; Gali, A.; Toth, M.; Englund, D.; Aharonovich, I. Bright Room-Temperature Single-Photon Emission from Defects in Gallium Nitride. *Adv. Mater.* **2017**, *29*, 1605092.
(456) Chakraborty, C.; Vamivakas, N.; Englund, D. *Nanophotonics* **2019**, *8*, 2017−2032.
(457) Toth, M.; Aharonovich, I. Single Photon Sources in Atomically Thin Materials. *Annu. Rev. Phys. Chem.* **2019**, *70*, 123−142.
(458) Thiel, C. W.; Böttger, T.; Cone, R. L. Rare-Earth-Doped Materials for Applications in Quantum Information Storage and Signal Processing. *J. Lumin.* **2011**, *131*, 353−361.
(459) Nakamura, I.; Yoshihiro, T.; Inagawa, H.; Fujiyoshi, S.; Matsushita, M. Spectroscopy of Single Pr3+ Ion in LaF3 Crystal at 1.5 K. *Sci. Rep.* **2015**, *4*, 7364.
(460) Utikal, T.; Eichhammer, E.; Petersen, L.; Renn, A.; Götzinger, S.; Sandoghdar, V. Spectroscopic Detection and State Preparation of a Single Praseodymium Ion in a Crystal. *Nat. Commun.* **2014**, *5*, 3627.
(461) Kolesov, R.; Xia, K.; Reuter, R.; Stöhr, R.; Zappe, A.; Meijer, J.; Hemmer, P. R.; Wrachtrup, J. Optical Detection of a Single Rare-Earth Ion in a Crystal. *Nat. Commun.* **2012**, *3*, 1029.
(462) Xia, K.; Kolesov, R.; Wang, Y.; Siyushev, P.; Reuter, R.; Kornher, T.; Kukharchyk, N.; Wieck, A. D.; Villa, B.; Yang, S.; Wrachtrup, J. All-Optical Preparation of Coherent Dark States of a Single Rare Earth Ion Spin in a Crystal. *Phys. Rev. Lett.* **2015**, *115*, 093602.
(463) Siyushev, P.; Xia, K.; Reuter, R.; Jamali, M.; Zhao, N.; Yang, N.; Duan, C.; Kukharchyk, N.; Wieck, A. D.; Kolesov, R.; Wrachtrup, J. Coherent Properties of Single Rare-Earth Spin Qubits. *Nat. Commun.* **2014**, *5*, 3895.
(464) Kolesov, R.; Xia, K.; Reuter, R.; Jamali, M.; Stöhr, R.; Inal, T.; Siyushev, P.; Wrachtrup, J. Mapping Spin Coherence of a Single Rare-Earth Ion in a Crystal onto a Single Photon Polarization State. *Phys. Rev. Lett.* **2013**, *111*, 120502.
(465) Zhong, T.; Kindem, J. M.; Bartholomew, J. G.; Rochman, J.; Craiciu, I.; Verma, V.; Nam, S. W.; Marsili, F.; Shaw, M. D.; Beyer, A. D.; Faraon, A. Optically Addressing Single Rare-Earth Ions in a Nanophotonic Cavity. *Phys. Rev. Lett.* **2018**, *121*, 183603.
(466) Yin, C.; Rancic, M.; de Boo, G. G.; Stavrias, N.; McCallum, J. C.; Sellars, M. J.; Rogge, S. Optical Addressing of an Individual Erbium Ion in Silicon. *Nature* **2013**, *497*, 91−94.
(467) Dibos, A. M.; Raha, M.; Phenicie, C. M.; Thompson, J. D. Atomic Source of Single Photons in the Telecom Band. *Phys. Rev. Lett.* **2018**, *120*, 243601.
(468) Tribollet, J.; Behrends, J.; Lips, K. Ultra Long Spin Coherence Time for Fe^{3+} in ZnO: A New Spin Qubit. *EPL (Europhysics Lett.* **2008**, *84*, 20009.
(469) Diler, B.; Whiteley, S. J.; Anderson, C. P.; Wolfowicz, G.; Wesson, M. E.; Bielejec, E. S.; Joseph Heremans, F.; Awschalom, D. D. Coherent Control and High-Fidelity Readout of Chromium Ions in Commercial Silicon Carbide. *npj Quantum Inf.* **2020**, *6*, 11.
(470) von Bardeleben, H. J.; Zargaleh, S. A.; Cantin, J. L.; Gao, W. B.; Biktagirov, T.; Gerstmann, U. Transition Metal Qubits in 4 H -Silicon Carbide: A Correlated EPR and DFT Study of the Spin S = 1 Vanadium V 3 + Center. *Phys. Rev. Mater.* **2019**, *3*, 124605.
(471) Wolfowicz, G.; Anderson, C. P.; Diler, B.; Poluektov, O. G.; Heremans, F. J.; Awschalom, D. D. Vanadium Spin Qubits as Telecom Quantum Emitters in Silicon Carbide. *Sci. Adv.* **2020**, *6*, No. eaaz1192.
(472) Spindlberger, L.; Csóré, A.; Thiering, G.; Putz, S.; Karhu, R.; Hassan, J. U.; Son, N. T.; Fromherz, T.; Gali, A.; Trupke, M. Optical Properties of Vanadium in 4 *H* Silicon Carbide for Quantum Technology. *Phys. Rev. Appl.* **2019**, *12*, 014015.
(473) Smith, J. M.; Meynell, S. A.; Bleszynski Jayich, A. C.; Meijer, J. Colour Centre Generation in Diamond for Quantum Technologies. *Nanophotonics* **2019**, *8*, 1889−1906.
(474) Weber, J. R.; Koehl, W. F.; Varley, J. B.; Janotti, A.; Buckley, B. B.; Van de Walle, C. G.; Awschalom, D. D. Quantum Computing with Defects. *Proc. Natl. Acad. Sci. U. S. A.* **2010**, *107*, 8513−8518.
(475) Davies, J. J. *Optically-Detected Magnetic Resonance of II-VI Compounds*; Springer: Boston, MA, 1989; pp 311−320.
(476) Ye, M.; Seo, H.; Galli, G. Spin Coherence in Two-Dimensional Materials. *npj Comput. Mater.* **2019**, *5*, 44.
(477) Sahu, A.; Kang, M. S.; Kompch, A.; Notthoff, C.; Wills, A. W.; Deng, D.; Winterer, M.; Frisbie, C. D.; Norris, D. J. Electronic Impurity Doping in CdSe Nanocrystals. *Nano Lett.* **2012**, *12*, 2587−2594.
(478) Muckel, F.; Yang, J.; Lorenz, S.; Baek, W.; Chang, H.; Hyeon, T.; Bacher, G.; Fainblat, R. Digital Doping in Magic-Sized CdSe Clusters. *ACS Nano* **2016**, *10*, 7135−7141.
(479) Yang, J.; Muckel, F.; Baek, W.; Fainblat, R.; Chang, H.; Bacher, G.; Hyeon, T. Chemical Synthesis, Doping, and Transformation of Magic-Sized Semiconductor Alloy Nanoclusters. *J. Am. Chem. Soc.* **2017**, *139*, 6761−6770.
(480) Fainblat, R.; Barrows, C. J.; Gamelin, D. R. Single Magnetic Impurities in Colloidal Quantum Dots and Magic-Size Clusters. *Chem. Mater.* **2017**, *29*, 8023−8036.
(481) Togan, E.; Chu, Y.; Trifonov, A. S.; Jiang, L.; Maze, J.; Childress, L.; Dutt, M. V. G.; Sørensen, A. S.; Hemmer, P. R.; Zibrov, A. S.; Lukin, M. D. Quantum Entanglement between an Optical Photon and a Solid-State Spin Qubit. *Nature* **2010**, *466*, 730−734.
(482) Buckley, B. B.; Fuchs, G. D.; Bassett, L. C.; Awschalom, D. D. Spin-Light Coherence for Single-Spin Measurement and Control in Diamond. *Science (Washington, DC, U. S.)* **2010**, *330*, 1212−1215.
(483) Yale, C. G.; Buckley, B. B.; Christle, D. J.; Burkard, G.; Heremans, F. J.; Bassett, L. C.; Awschalom, D. D. All-Optical Control of a Solid-State Spin Using Coherent Dark States. *Proc. Natl. Acad. Sci. U. S. A.* **2013**, *110*, 7595−7600.
(484) Bassett, L. C.; Heremans, F. J.; Christle, D. J.; Yale, C. G.; Burkard, G.; Buckley, B. B.; Awschalom, D. D. Ultrafast Optical Control of Orbital and Spin Dynamics in a Solid-State Defect. *Science* **2014**, *345*, 1333−1337.
(485) Becker, J. N.; Görlitz, J.; Arend, C.; Markham, M.; Becher, C. Ultrafast All-Optical Coherent Control of Single Silicon Vacancy Colour Centres in Diamond. *Nat. Commun.* **2016**, *7*, 13512.
(486) Becker, J. N.; Pingault, B.; Groß, D.; Gündoğan, M.; Kukharchyk, N.; Markham, M.; Edmonds, A.; Atatüre, M.; Bushev, P.; Becher, C. All-Optical Control of the Silicon-Vacancy Spin in Diamond at Millikelvin Temperatures. *Phys. Rev. Lett.* **2018**, *120*, 053603.
(487) Rogers, L. J.; Jahnke, K. D.; Metsch, M. H.; Sipahigil, A.; Binder, J. M.; Teraji, T.; Sumiya, H.; Isoya, J.; Lukin, M. D.; Hemmer, P.;

https://dx.doi.org/10.1021/acs.chemrev.0c00831
Chem. Rev. 2021, 121, 3186−3233

Jelezko, F. All-Optical Initialization, Readout, and Coherent Preparation of Single Silicon-Vacancy Spins in Diamond. *Phys. Rev. Lett.* **2014**, *113*, 263602.
(488) Pingault, B.; Becker, J. N.; Schulte, C. H. H.; Arend, C.; Hepp, C.; Godde, T.; Tartakovskii, A. I.; Markham, M.; Becher, C.; Atatüre, M. All-Optical Formation of Coherent Dark States of Silicon-Vacancy Spins in Diamond. *Phys. Rev. Lett.* **2014**, *113*, 263601.
(489) Sipahigil, A.; Evans, R. E.; Sukachev, D. D.; Burek, M. J.; Borregaard, J.; Bhaskar, M. K.; Nguyen, C. T.; Pacheco, J. L.; Atikian, H. A.; Meuwly, C.; Camacho, R. M.; Jelezko, F.; Bielejec, E.; Park, H.; Lončar, M.; Lukin, M. D. An Integrated Diamond Nanophotonics Platform for Quantum-Optical Networks. *Science* **2016**, *354*, 847−850.
(490) Evans, R. E.; Bhaskar, M. K.; Sukachev, D. D.; Nguyen, C. T.; Sipahigil, A.; Burek, M. J.; Machielse, B.; Zhang, G. H.; Zibrov, A. S.; Bielejec, E.; Park, H.; Lončar, M.; Lukin, M. D. Photon-Mediated Interactions between Quantum Emitters in a Diamond Nanocavity. *Science* **2018**, *362*, 662−665.
(491) Ladd, T. D.; Sanaka, K.; Yamamoto, Y.; Pawlis, A.; Lischka, K. Fluorine-Doped ZnSe for Applications in Quantum Information Processing. *Phys. Status Solidi B* **2010**, *247*, 1543−1546.
(492) Heisterkamp, F.; Zhukov, E. A.; Greilich, A.; Yakovlev, D. R.; Korenev, V. L.; Pawlis, A.; Bayer, M. Longitudinal and Transverse Spin Dynamics of Donor-Bound Electrons in Fluorine-Doped ZnSe: Spin Inertia versus Hanle Effect. *Phys. Rev. B: Condens. Matter Mater. Phys.* **2015**, *91*, 235432.
(493) Kim, Y. M.; Sleiter, D.; Sanaka, K.; Reuter, D.; Lischka, K.; Yamamoto, Y.; Pawlis, A. Optically Controlled Initialization and Readout of an Electron Spin Bound to a Fluorine Donor in ZnSe. *Curr. Appl. Phys.* **2014**, *14*, 1234−1239.
(494) Linpeng, X.; Viitaniemi, M. L. K.; Vishnuradhan, A.; Kozuka, Y.; Johnson, C.; Kawasaki, M.; Fu, K.-M. C. Coherence Properties of Shallow Donor Qubits in ZnO. *Phys. Rev. Appl.* **2018**, *10*, 064061.
(495) Choi, S.; Phillips, M. R.; Aharonovich, I.; Pornsuwan, S.; Cowie, B. C. C.; Ton-That, C. Photophysics of Point Defects in ZnO Nanoparticles. *Adv. Opt. Mater.* **2015**, *3*, 821−827.
(496) Jungwirth, N. R.; Chang, H.-S.; Jiang, M.; Fuchs, G. D. Polarization Spectroscopy of Defect-Based Single Photon Sources in ZnO. *ACS Nano* **2016**, *10*, 1210−1215.
(497) Le Gall, C.; Besombes, L.; Boukari, H.; Kolodka, R.; Cibert, J.; Mariette, H. Optical Spin Orientation of a Single Manganese Atom in a Semiconductor Quantum Dot Using Quasiresonant Photoexcitation. *Phys. Rev. Lett.* **2009**, *102*, 127402.
(498) Goryca, M.; Kazimierczuk, T.; Nawrocki, M.; Golnik, A.; Gaj, J. A.; Kossacki, P.; Wojnar, P.; Karczewski, G. Optical Manipulation of a Single Mn Spin in a CdTe-Based Quantum Dot. *Phys. Rev. Lett.* **2009**, *103*, 087401.
(499) Le Gall, C.; Kolodka, R. S.; Cao, C. L.; Boukari, H.; Mariette, H.; Fernández-Rossier, J.; Besombes, L. Optical Initialization, Readout, and Dynamics of a Mn Spin in a Quantum Dot. *Phys. Rev. B: Condens. Matter Mater. Phys.* **2010**, *81*, 245315.
(500) Goryca, M.; Koperski, M.; Wojnar, P.; Smoleński, T.; Kazimierczuk, T.; Golnik, A.; Kossacki, P. Coherent Precession of an Individual 5/2 Spin. *Phys. Rev. Lett.* **2014**, *113*, 227202.
(501) Besombes, L.; Léger, Y.; Maingault, L.; Ferrand, D.; Mariette, H.; Cibert, J. Probing the Spin State of a Single Magnetic Ion in an Individual Quantum Dot. *Phys. Rev. Lett.* **2004**, *93*, 207403.
(502) Goryca, M.; Kazimierczuk, T.; Nawrocki, M.; Golnik, A.; Gaj, J. A.; Wojnar, P.; Karczewski, G.; Kossacki, P. Optical Manipulation of a Single Mn Spin in a CdTe Quantum Dot. *Phys. E* **2010**, *42*, 2690−2693.
(503) Childress, L.; Gurudev Dutt, M. V.; Taylor, J. M.; Zibrov, A. S.; Jelezko, F.; Wrachtrup, J.; Hemmer, P. R.; Lukin, M. D. Coherent Dynamics of Coupled Electron and Nuclear Spin Qubits in Diamond. *Science* **2006**, *314*, 281−285.
(504) Dutt, M. V. G.; Childress, L.; Jiang, L.; Togan, E.; Maze, J.; Jelezko, F.; Zibrov, A. S.; Hemmer, P. R.; Lukin, M. D. Quantum Register Based on Individual Electronic and Nuclear Spin Qubits in Diamond. *Science* **2007**, *316*, 1312−1316.
(505) Maurer, P. C.; Kucsko, G.; Latta, C.; Jiang, L.; Yao, N. Y.; Bennett, S. D.; Pastawski, F.; Hunger, D.; Chisholm, N.; Markham, M.; Twitchen, D. J.; Cirac, J. I.; Lukin, M. D. Room-Temperature Quantum Bit Memory Exceeding One Second. *Science* **2012**, *336*, 1283−1286.
(506) Reiserer, A.; Kalb, N.; Blok, M. S.; van Bemmelen, K. J. M.; Taminiau, T. H.; Hanson, R.; Twitchen, D. J.; Markham, M. Robust Quantum-Network Memory Using Decoherence-Protected Subspaces of Nuclear Spins. *Phys. Rev. X* **2016**, *6*, 021040.
(507) Giovannetti, V.; Lloyd, S.; Maccone, L.; Hemmer, P.; Watanabe, H.; Yamasaki, S.; Jacques, V.; Gaebel, T.; Jelezko, F.; Wrachtrup, J. Quantum-Enhanced Measurements: Beating the Standard Quantum Limit. *Science (Washington, DC, U. S.)* **2004**, *306*, 1330−1336.
(508) Cramer, J.; Kalb, N.; Rol, M. A.; Hensen, B.; Blok, M. S.; Markham, M.; Twitchen, D. J.; Hanson, R.; Taminiau, T. H. Repeated Quantum Error Correction on a Continuously Encoded Qubit by Real-Time Feedback. *Nat. Commun.* **2016**, *7*, 11526.
(509) Bradley, C. E.; Randall, J.; Abobeih, M. H.; Berrevoets, R. C.; Degen, M. J.; Bakker, M. A.; Markham, M.; Twitchen, D. J.; Taminiau, T. H. A Ten-Qubit Solid-State Spin Register with Quantum Memory up to One Minute. *Phys. Rev. X* **2019**, *9*, 031045.
(510) Holzgrafe, J.; Beitner, J.; Kara, D.; Knowles, H. S.; Atatüre, M. Error Corrected Spin-State Readout in a Nanodiamond. *npj Quantum Inf.* **2019**, *5*, 13.
(511) Lovchinsky, I.; Sushkov, A. O.; Urbach, E.; de Leon, N. P.; Choi, S.; De Greve, K.; Evans, R.; Gertner, R.; Bersin, E.; Müller, C.; McGuinness, L.; Jelezko, F.; Walsworth, R. L.; Park, H.; Lukin, M. D. Nuclear Magnetic Resonance Detection and Spectroscopy of Single Proteins Using Quantum Logic. *Science* **2016**, *351*, 836−841.
(512) Unden, T.; Balasubramanian, P.; Louzon, D.; Vinkler, Y.; Plenio, M. B.; Markham, M.; Twitchen, D.; Stacey, A.; Lovchinsky, I.; Sushkov, A. O.; Lukin, M. D.; Retzker, A.; Naydenov, B.; McGuinness, L. P.; Jelezko, F. Quantum Metrology Enhanced by Repetitive Quantum Error Correction. *Phys. Rev. Lett.* **2016**, *116*, 230502.
(513) Bhaskar, M. K.; Riedinger, R.; Machielse, B.; Levonian, D. S.; Nguyen, C. T.; Knall, E. N.; Park, H.; Englund, D.; Lončar, M.; Sukachev, D. D.; Lukin, M. D. Experimental Demonstration of Memory-Enhanced Quantum Communication. *Nature* **2020**, *580*, 60−64.
(514) Degen, C. L. L.; Reinhard, F.; Cappellaro, P. Quantum Sensing. *Rev. Mod. Phys.* **2017**, *89*, 035002.
(515) Sangtawesin, S.; Dwyer, B. L.; Srinivasan, S.; Allred, J. J.; Rodgers, L. V. H.; De Greve, K.; Stacey, A.; Dontschuk, N.; O'Donnell, K. M.; Hu, D.; Evans, D. A.; Jaye, C.; Fischer, D. A.; Markham, M. L.; Twitchen, D. J.; Park, H.; Lukin, M. D.; de Leon, N. P. Origins of Diamond Surface Noise Probed by Correlating Single-Spin Measurements with Surface Spectroscopy. *Phys. Rev. X* **2019**, *9*, 031052.
(516) Reineck, P.; Trindade, L. F.; Havlik, J.; Stursa, J.; Heffernan, A.; Elbourne, A.; Orth, A.; Capelli, M.; Cigler, P.; Simpson, D. A.; Gibson, B. C. Not All Fluorescent Nanodiamonds Are Created Equal: A Comparative Study. *Part. Part. Syst. Charact.* **2019**, *36*, 1900009.
(517) Heisterkamp, F.; Kirstein, E.; Greilich, A.; Zhukov, E. A.; Kazimierczuk, T.; Yakovlev, D. R.; Pawlis, A.; Bayer, M. Dynamics of Nuclear Spin Polarization Induced and Detected by Coherently Precessing Electron Spins in Fluorine-Doped ZnSe. *Phys. Rev. B: Condens. Matter Mater. Phys.* **2016**, *93*, 081409.
(518) Yang, J.; Choi, M. K.; Kim, D.-H.; Hyeon, T. Designed Assembly and Integration of Colloidal Nanocrystals for Device Applications. *Adv. Mater.* **2016**, *28*, 1176−1207.
(519) Wang, Y.; Fedin, I.; Zhang, H.; Talapin, D. V. Direct Optical Lithography of Functional Inorganic Nanomaterials. *Science* **2017**, *357*, 385−388.
(520) Kahl, M.; Thomay, T.; Kohnle, V.; Beha, K.; Merlein, J.; Hagner, M.; Halm, A.; Ziegler, J.; Nann, T.; Fedutik, Y.; Woggon, U.; Artemyev, M.; Pérez-Willard, F.; Leitenstorfer, A.; Bratschitsch, R. Colloidal Quantum Dots in All-Dielectric High- Q Pillar Microcavities. *Nano Lett.* **2007**, *7*, 2897−2900.
(521) Hoang, T. B.; Akselrod, G. M.; Mikkelsen, M. H. Ultrafast Room-Temperature Single Photon Emission from Quantum Dots Coupled to Plasmonic Nanocavities. *Nano Lett.* **2016**, *16*, 270−275.

https://dx.doi.org/10.1021/acs.chemrev.0c00831
Chem. Rev. 2021, 121, 3186−3233

(522) Requicha, A. Nanomanipulation with the Atomic Force Microscope. *Nanotechnology*; Wiley-VCH Verlag GmbH & Co. KGaA: Weinheim, Germany, 2010; pp 239−2731.
(523) Barth, M.; Schietinger, S.; Fischer, S.; Becker, J.; Nüsse, N.; Aichele, T.; Löchel, B.; Sönnichsen, C.; Benson, O. Nanoassembled Plasmonic-Photonic Hybrid Cavity for Tailored Light-Matter Coupling. *Nano Lett.* **2010**, *10*, 891−895.
(524) Schell, A. W.; Kewes, G.; Schröder, T.; Wolters, J.; Aichele, T.; Benson, O. A Scanning Probe-Based Pick-and-Place Procedure for Assembly of Integrated Quantum Optical Hybrid Devices. *Rev. Sci. Instrum.* **2011**, *82*, 073709.
(525) Kolchin, P.; Pholchai, N.; Mikkelsen, M. H.; Oh, J.; Ota, S.; Islam, M. S.; Yin, X.; Zhang, X. High Purcell Factor Due To Coupling of a Single Emitter to a Dielectric Slot Waveguide. *Nano Lett.* **2015**, *15*, 464−468.
(526) Ratchford, D.; Shafiei, F.; Kim, S.; Gray, S. K.; Li, X. Manipulating Coupling between a Single Semiconductor Quantum Dot and Single Gold Nanoparticle. *Nano Lett.* **2011**, *11*, 1049−1054.
(527) Liu, C. Parallel Scanning Probe Arrays: Their Applications. *Mater. Today* **2008**, *11*, 22−29.
(528) Abudayyeh, H.; Lubotzky, B.; Blake, A.; Wan, J.; Majumder, S.; Hu, Z.; Kim, Y.; Htoon, H.; Bose, R.; Malko, A. V.; Hollingsworth, J. A.; Rapaport, R. High Purity Single Photon Sources with Near Unity Collection Efficiencies by Deterministic Placement of Quantum Dots in Nanoantennas; *arXiv:2005.11548*, 2020; pp 1−19.
(529) Piner, R. D.; Zhu, J.; Xu, F.; Hong, S.; Mirkin, C. A. Dip-Pen" Nanolithography. *Science (Washington, DC, U. S.)* **1999**, *283*, 661−663.
(530) Brown, K. A.; Eichelsdoerfer, D. J.; Liao, X.; He, S.; Mirkin, C. A. Material Transport in Dip-Pen Nanolithography. *Front. Phys.* **2014**, *9*, 385−397.
(531) Xu, X.; Yang, Q.; Cheung, K. M.; Zhao, C.; Wattanatorn, N.; Belling, J. N.; Abendroth, J. M.; Slaughter, L. S.; Mirkin, C. A.; Andrews, A. M.; Weiss, P. S. Polymer-Pen Chemical Lift-Off Lithography. *Nano Lett.* **2017**, *17*, 3302−3311.
(532) Ni, S.; Leemann, J.; Buttinoni, I.; Isa, L.; Wolf, H. Programmable Colloidal Molecules from Sequential Capillarity-Assisted Particle Assembly. *Sci. Adv.* **2016**, *2*, e1501779.
(533) Ni, S.; Isa, L.; Wolf, H. Capillary Assembly as a Tool for the Heterogeneous Integration of Micro- and Nanoscale Objects. *Soft Matter* **2018**, *14*, 2978−2995.
(534) Kuemin, C.; Stutz, R.; Spencer, N. D.; Wolf, H. Precise Placement of Gold Nanorods by Capillary Assembly. *Langmuir* **2011**, *27*, 6305−6310.
(535) Greybush, N. J.; Pacheco-Peña, V.; Engheta, N.; Murray, C. B.; Kagan, C. R. Plasmonic Optical and Chiroptical Response of Self-Assembled Au Nanorod Equilateral Trimers. *ACS Nano* **2019**, *13*, 1617−1624.
(536) Greybush, N. J.; Liberal, I.; Malassis, L.; Kikkawa, J. M.; Engheta, N.; Murray, C. B.; Kagan, C. R. Plasmon Resonances in Self-Assembled Two-Dimensional Au Nanocrystal Metamolecules. *ACS Nano* **2017**, *11*, 2917−2927.
(537) Flauraud, V.; Mastrangeli, M.; Bernasconi, G. D.; Butet, J.; Alexander, D. T. L.; Shahrabi, E.; Martin, O. J. F.; Brugger, J. Nanoscale Topographical Control of Capillary Assembly of Nanoparticles. *Nat. Nanotechnol.* **2017**, *12*, 73−80.
(538) Malaquin, L.; Kraus, T.; Schmid, H.; Delamarche, E.; Wolf, H. Controlled Particle Placement through Convective and Capillary Assembly. *Langmuir* **2007**, *23*, 11513−11521.
(539) Greybush, N. J.; Saboktakin, M.; Ye, X.; Della Giovampaola, C.; Oh, S. J.; Berry, N. E.; Engheta, N.; Murray, C. B.; Kagan, C. R. Plasmon-Enhanced Upconversion Luminescence in Single Nanophosphor-Nanorod Heterodimers Formed through Template-Assisted Self-Assembly. *ACS Nano* **2014**, *8*, 9482−9491.
(540) Saboktakin, M.; Ye, X.; Chettiar, U. K.; Engheta, N.; Murray, C. B.; Kagan, C. R. Plasmonic Enhancement of Nanophosphor Upconversion Luminescence in Au Nanohole Arrays. *ACS Nano* **2013**, *7*, 7186−7192.
(541) Black, C. T.; Murray, C. B.; Sandstrom, R. L. Embedded nanoparticle films and method for their formation in selective areas on a surface; 2012, US Patent 7,682,591.
(542) Greybush, N. J.; Saboktakin, M.; Ye, X.; Della Giovampaola, C.; Oh, S. J.; Berry, N. E.; Engheta, N.; Murray, C. B.; Kagan, C. R. Plasmon-Enhanced Upconversion Luminescence in Single Nanophosphor-Nanorod Heterodimers Formed through Template-Assisted Self-Assembly. *ACS Nano* **2014**, *8*, 9482−9491.
(543) Asbahi, M.; Mehraeen, S.; Wang, F.; Yakovlev, N.; Chong, K. S. L.; Cao, J.; Tan, M. C.; Yang, J. K. W. Large Area Directed Self-Assembly of Sub-10 Nm Particles with Single Particle Positioning Resolution. *Nano Lett.* **2015**, *15*, 6066−6070.
(544) Li, J.; Hill, E. H.; Lin, L.; Zheng, Y. Optical Nanoprinting of Colloidal Particles and Functional Structures. *ACS Nano* **2019**, *13*, 3783−3795.
(545) Gargiulo, J.; Violi, I. L.; Cerrota, S.; Chvátal, L.; Cortés, E.; Perassi, E. M.; Diaz, F.; Zemánek, P.; Stefani, F. D. Accuracy and Mechanistic Details of Optical Printing of Single Au and Ag Nanoparticles. *ACS Nano* **2017**, *11*, 9678−9688.
(546) Zaza, C.; Violi, I. L.; Gargiulo, J.; Chiarelli, G.; Schumacher, L.; Jakobi, J.; Olmos-Trigo, J.; Cortes, E.; König, M.; Barcikowski, S.; Schlücker, S.; Sáenz, J. J.; Maier, S. A.; Stefani, F. D. Size-Selective Optical Printing of Silicon Nanoparticles through Their Dipolar Magnetic Resonance. *ACS Photonics* **2019**, *6*, 815−822.
(547) Nedev, S.; Urban, A. S.; Lutich, A. A.; Feldmann, J. Optical Force Stamping Lithography. *Nano Lett.* **2011**, *11*, 5066−5070.
(548) Jiang, M.; Kurvits, J. A.; Lu, Y.; Nurmikko, A. V.; Zia, R. Reusable Inorganic Templates for Electrostatic Self-Assembly of Individual Quantum Dots, Nanodiamonds, and Lanthanide-Doped Nanoparticles. *Nano Lett.* **2015**, *15*, 5010−5016.
(549) Ropp, C.; Cummins, Z.; Probst, R.; Qin, S.; Fourkas, J. T.; Shapiro, B.; Waks, E. Positioning and Immobilization of Individual Quantum Dots with Nanoscale Precision. *Nano Lett.* **2010**, *10*, 4673−4679.
(550) Marlow, F.; Muldarisnur Sharifi, P.; Brinkmann, R.; Mendive, C. Opals: Status and Prospects. *Angew. Chem., Int. Ed.* **2009**, *48*, 6212−6233.
(551) Cong, H.; Yu, B.; Tang, J.; Li, Z.; Liu, X. Current Status and Future Developments in Preparation and Application of Colloidal Crystals. *Chem. Soc. Rev.* **2013**, *42*, 7774.
(552) Murray, C. B.; Kagan, C. R.; Bawendi, M. G. Self-Organization of CdSe Nanocrystallites into Three-Dimensional Quantum Dot Superlattices. *Science (Washington, DC, U. S.)* **1995**, *270*, 1335−1338.
(553) Hanrath, T. Colloidal Nanocrystal Quantum Dot Assemblies as Artificial Solids. *J. Vac. Sci. Technol., A* **2012**, *30*, 030802.
(554) Wang, C.; Siu, C.; Zhang, J.; Fang, J. Understanding the Forces Acting in Self-Assembly and the Implications for Constructing Three-Dimensional (3D) Supercrystals. *Nano Res.* **2015**, *8*, 2445−2466.
(555) Li, P.; Peng, Q.; Li, Y. Controlled Synthesis and Self-Assembly of Highly Monodisperse Ag and Ag_2S Nanocrystals. *Chem. - Eur. J.* **2011**, *17*, 941−946.
(556) Wang, T.; LaMontagne, D.; Lynch, J.; Zhuang, J.; Cao, Y. C. Colloidal Superparticles from Nanoparticle Assembly. *Chem. Soc. Rev.* **2013**, *42*, 2804−2823.
(557) Cölfen, H.; Antonietti, M. Mesocrystals: Inorganic Superstructures Made by Highly Parallel Crystallization and Controlled Alignment. *Angew. Chem., Int. Ed.* **2005**, *44*, 5576−5591.
(558) Boles, M. A.; Engel, M.; Talapin, D. V. Self-Assembly of Colloidal Nanocrystals: From Intricate Structures to Functional Materials. *Chem. Rev.* **2016**, *116*, 11220−11289.
(559) Diroll, B. T.; Weigandt, K. M.; Jishkariani, D.; Cargnello, M.; Murphy, R. J.; Hough, L. A.; Murray, C. B.; Donnio, B. Quantifying "Softness" of Organic Coatings on Gold Nanoparticles Using Correlated Small-Angle X-Ray and Neutron Scattering. *Nano Lett.* **2015**, *15*, 8008−8012.
(560) Si, K. J.; Chen, Y.; Shi, Q.; Cheng, W. Nanoparticle Superlattices: The Roles of Soft Ligands. *Adv. Sci.* **2018**, *5*, 1700179.

https://dx.doi.org/10.1021/acs.chemrev.0c00831
Chem. Rev. 2021, 121, 3186−3233

(561) Bishop, K. J. M.; Wilmer, C. E.; Soh, S.; Grzybowski, B. A. Nanoscale Forces and Their Uses in Self-Assembly. *Small* **2009**, *5*, 1600−1630.
(562) Vanmaekelbergh, D. Self-Assembly of Colloidal Nanocrystals as Route to Novel Classes of Nanostructured Materials. *Nano Today* **2011**, *6*, 419−437.
(563) Rogach, A. L.; Talapin, D. V.; Shevchenko, E. V.; Kornowski, A.; Haase, M.; Weller, H. Organization of Matter on Different Size Scales: Monodisperse Nanocrystals and Their Superstructures. *Adv. Funct. Mater.* **2002**, *12*, 653−664.
(564) Claridge, S. A.; Castleman, A. W.; Khanna, S. N.; Murray, C. B.; Sen, A.; Weiss, P. S. Cluster-Assembled Materials. *ACS Nano* **2009**, *3*, 244−255.
(565) Li, F.; Josephson, D. P.; Stein, A. Colloidal Assembly: The Road from Particles to Colloidal Molecules and Crystals. *Angew. Chem., Int. Ed.* **2011**, *50*, 360−388.
(566) Ambrosetti, A.; Ferri, N.; DiStasio, R. A.; Tkatchenko, A. Wavelike Charge Density Fluctuations and van Der Waals Interactions at the Nanoscale. *Science* **2016**, *351*, 1171−1176.
(567) Lu, P. J.; Zaccarelli, E.; Ciulla, F.; Schofield, A. B.; Sciortino, F.; Weitz, D. A. Gelation of Particles with Short-Range Attraction. *Nature* **2008**, *453*, 499−503.
(568) Bodnarchuk, M. I.; Kovalenko, M. V.; Heiss, W.; Talapin, D. V. Energetic and Entropic Contributions to Self-Assembly of Binary Nanocrystal Superlattices: Temperature as the Structure-Directing Factor. *J. Am. Chem. Soc.* **2010**, *132*, 11967−11977.
(569) Bodnarchuk, M. I.; Kovalenko, M. V.; Pichler, S.; Fritz-Popovski, G.; Hesser, G. G.; Heiss, W. Large-Area Ordered Superlattices from Magnetic Wustite/Cobalt Ferrite Core/Shell Nanocrystals by Doctor Blade Casting. *ACS Nano* **2010**, *4*, 423−431.
(570) Gole, A.; Jana, N. R.; Selvan, S. T.; Ying, J. Y. Langmuir-Blodgett Thin Films of Quantum Dots: Synthesis, Surface Modification, and Fluorescence Resonance Energy Transfer (FRET) Studies. *Langmuir* **2008**, *24*, 8181−8186.
(571) Dabbousi, B. O.; Murray, C. B.; Rubner, M. F.; Bawendi, M. G. Langmuir-Blodgett Manipulation of Size-Selected CdSe Nanocrystallites. *Chem. Mater.* **1994**, *6*, 216−219.
(572) Rupich, S. M.; Shevchenko, E. V.; Bodnarchuk, M. I.; Lee, B.; Talapin, D. V. Size-Dependent Multiple Twinning in Nanocrystal Superlattices. *J. Am. Chem. Soc.* **2010**, *132*, 289−296.
(573) Talapin, D. V.; Shevchenko, E. V.; Kornowski, A.; Gaponik, N.; Haase, M.; Rogach, A. L.; Weller, H. A New Approach to Crystallization of CdSe Nanoparticles into Ordered Three-Dimensional Superlattices. *Adv. Mater.* **2001**, *13*, 1868.
(574) Chayen, N. E. Turning Protein Crystallisation from an Art into a Science. *Curr. Opin. Struct. Biol.* **2004**, *14*, 577−583.
(575) Yang, Y.; Qin, H.; Jiang, M.; Lin, L.; Fu, T.; Dai, X.; Zhang, Z.; Niu, Y.; Cao, H.; Jin, Y.; Zhao, F.; Peng, X. Entropic Ligands for Nanocrystals: From Unexpected Solution Properties to Outstanding Processability. *Nano Lett.* **2016**, *16*, 2133−2138.
(576) Yang, Y.; Qin, H.; Peng, X. Intramolecular Entropy and Size-Dependent Solution Properties of Nanocrystal-Ligands Complexes. *Nano Lett.* **2016**, *16*, 2127−2132.
(577) Mattoussi, H.; Cumming, A. W.; Murray, C. B.; Bawendi, M. G.; Ober, R. Properties of CdSe Nanocrystal Dispersions in the Dilute Regime: Structure and Interparticle Interactions. *Phys. Rev. B: Condens. Matter Mater. Phys.* **1998**, *58*, 7850−7863.
(578) Boles, M. A.; Talapin, D. V. Self-Assembly of Tetrahedral CdSe Nanocrystals: Effective "Patchiness" via Anisotropic Steric Interaction. *J. Am. Chem. Soc.* **2014**, *136*, 5868−5871.
(579) Lee, B.; Podsiadlo, P.; Rupich, S.; Talapin, D. V.; Rajh, T.; Shevchenko, E. V. Comparison of Structural Behavior of Nanocrystals in Randomly Packed Films and Long-Range Ordered Superlattices by Time-Resolved Small Angle X-Ray Scattering. *J. Am. Chem. Soc.* **2009**, *131*, 16386−16388.
(580) Wu, L.; Willis, J. J.; McKay, I. S.; Diroll, B. T.; Qin, J.; Cargnello, M.; Tassone, C. J. High-Temperature Crystallization of Nanocrystals into Three-Dimensional Superlattices. *Nature* **2017**, *548*, 197−201.
(581) Evers, W. H.; Friedrich, H.; Filion, L.; Dijkstra, M.; Vanmaekelbergh, D. Observation of a Ternary Nanocrystal Superlattice and Its Structural Characterization by Electron Tomography. *Angew. Chem., Int. Ed.* **2009**, *48*, 9655−9657.
(582) Friedrich, H.; Gommes, C. J.; Overgaag, K.; Meeldijk, J. D.; Evers, W. H.; Nijs, B.; de Boneschanscher, M. P.; de Jongh, P. E.; Verkleij, A. J.; de Jong, K. P.; van Blaaderen, A.; Vanmaekelbergh, D. Quantitative Structural Analysis of Binary Nanocrystal Superlattices by Electron Tomography. *Nano Lett.* **2009**, *9*, 2719−2724.
(583) Chen, Z.; O'Brien, S. Structure Direction of II-VI Semiconductor Quantum Dot Binary Nanoparticle Superlattices by Tuning Radius Ratio. *ACS Nano* **2008**, *2*, 1219−1229.
(584) Hopkins, A. B.; Stillinger, F. H.; Torquato, S. Densest Binary Sphere Packings. *Phys. Rev. E* **2012**, *85*, 021130.
(585) O'Toole, P. I.; Hudson, T. S. New High-Density Packings of Similarly Sized Binary Spheres. *J. Phys. Chem. C* **2011**, *115*, 19037−19040.
(586) Filion, L.; Dijkstra, M. Prediction of Binary Hard-Sphere Crystal Structures. *Phys. Rev. E* **2009**, *79*, 046714.
(587) Overgaag, K.; Evers, W.; de Nijs, B.; Koole, R.; Meeldijk, J.; Vanmaekelbergh, D. Binary Superlattices of PbSe and CdSe Nanocrystals. *J. Am. Chem. Soc.* **2008**, *130*, 7833−7835.
(588) Kummerfeld, J. K.; Hudson, T. S.; Harrowell, P. The Densest Packing of AB Binary Hard-Sphere Homogeneous Compounds across All Size Ratios. *J. Phys. Chem. B* **2008**, *112*, 10773−10776.
(589) Diroll, B. T.; Greybush, N. J.; Kagan, C. R.; Murray, C. B. Smectic Nanorod Superlattices Assembled on Liquid Subphases: Structure, Orientation, Defects, and Optical Polarization. *Chem. Mater.* **2015**, *27*, 2998−3008.
(590) Li, L.-S.; Alivisatos, A. P. Semiconductor Nanorod Liquid Crystals and Their Assembly on a Substrate. *Adv. Mater.* **2003**, *15*, 408−411.
(591) Li, L.; Walda, J.; Manna, L.; Alivisatos, A. P. Semiconductor Nanorod Liquid Crystals. *Nano Lett.* **2002**, *2*, 557−560.
(592) Gryn, I.; Lacaze, E.; Carbone, L.; Giocondo, M.; Zappone, B. Electric-Field-Controlled Alignment of Rod-Shaped Fluorescent Nanocrystals in Smectic Liquid Crystal Defect Arrays. *Adv. Funct. Mater.* **2016**, *26*, 7122−7131.
(593) Zhong, H.; Ye, M.; Zhou, Y.; Yang, C.; Li, Y. Synthesis of In_2S_3 Nanoplates and Their Self-Assembly into Superlattices. *J. Nanosci. Nanotechnol.* **2007**, *7*, 4346−4352.
(594) Momper, R.; Zhang, H.; Chen, S.; Halim, H.; Johannes, E.; Yordanov, S.; Braga, D.; Blülle, B.; Doblas, D.; Kraus, T.; Bonn, M.; Wang, H. I.; Riedinger, A. Kinetic Control over Self-Assembly of Semiconductor Nanoplatelets. *Nano Lett.* **2020**, *20*, 4102−4110.
(595) Zhang, H.-T.; Wu, G.; Chen, X.-H. Large-Scale Synthesis and Self-Assembly of Monodisperse Hexagon Cu 2 S Nanoplates. *Langmuir* **2005**, *21*, 4281−4282.
(596) Saunders, A. E.; Ghezelbash, A.; Smilgies, D.-M.; Sigman, M. B.; Korgel, B. A. Columnar Self-Assembly of Colloidal Nanodisks. *Nano Lett.* **2006**, *6*, 2959−2963.
(597) Boles, M. A.; Talapin, D. V. Many-Body Effects in Nanocrystal Superlattices: Departure from Sphere Packing Explains Stability of Binary Phases. *J. Am. Chem. Soc.* **2015**, *137*, 4494−4502.
(598) Goubet, N.; Richardi, J.; Albouy, P. A.; Pileni, M. P. How to Predict the Growth Mechanism of Supracrystals from Gold Nanocrystals. *J. Phys. Chem. Lett.* **2011**, *2*, 417−422.
(599) Reichhelm, A.; Haubold, D.; Eychmüller, A. Ligand Versatility in Supercrystal Formation. *Adv. Funct. Mater.* **2017**, *27*, 1700361.
(600) Goodfellow, B. W.; Yu, Y.; Bosoy, C. A.; Smilgies, D.-M.; Korgel, B. A. The Role of Ligand Packing Frustration in Body-Centered Cubic (Bcc) Superlattices of Colloidal Nanocrystals. *J. Phys. Chem. Lett.* **2015**, *6*, 2406−2412.
(601) Diroll, B. T.; Jishkariani, D.; Cargnello, M.; Murray, C. B.; Donnio, B. Polycatenar Ligand Control of the Synthesis and Self-Assembly of Colloidal Nanocrystals. *J. Am. Chem. Soc.* **2016**, *138*, 10508−10515.
(602) Giansante, C. Library Design of Ligands at the Surface of Colloidal Nanocrystals. *Acc. Chem. Res.* **2020**, *53*, 1458−1467.

https://dx.doi.org/10.1021/acs.chemrev.0c00831
Chem. Rev. 2021, 121, 3186−3233

(603) Macfarlane, R. J.; Lee, B.; Jones, M. R.; Harris, N.; Schatz, G. C.; Mirkin, C. A. Nanoparticle Superlattice Engineering with DNA. *Science (Washington, DC, U. S.)* **2011**, *334*, 204−208.
(604) Jishkariani, D.; Elbert, K. C.; Wu, Y.; Lee, J. D.; Hermes, M.; Wang, D.; van Blaaderen, A.; Murray, C. B. Nanocrystal Core Size and Shape Substitutional Doping and Underlying Crystalline Order in Nanocrystal Superlattices. *ACS Nano* **2019**, *13*, 5712−5719.
(605) Chuang, C.-H. M.; Brown, P. R.; Bulović, V.; Bawendi, M. G. Improved Performance and Stability in Quantum Dot Solar Cells through Band Alignment Engineering. *Nat. Mater.* **2014**, *13*, 796−801.
(606) Chandrasekaran, V.; Tessier, M. D.; Dupont, D.; Geiregat, P.; Hens, Z.; Brainis, E. Nearly Blinking-Free, High-Purity Single-Photon Emission by Colloidal InP/ZnSe Quantum Dots. *Nano Lett.* **2017**, *17*, 6104−6109.
(607) Bruchez, M.; Moronne, M.; Gin, P.; Weiss, S.; Alivisatos, A. P. Semiconductor Nanocrystals as Fluorescent Biological Labels. *Science* **1998**, *281*, 2013−2016.
(608) Chan, W. C.; Nie, S. Quantum Dot Bioconjugates for Ultrasensitive Nonisotopic Detection. *Science* **1998**, *281*, 2016−2018.
(609) Shim, M.; Guyot-Sionnest, P. Permanent Dipole Moment and Charges in Colloidal Semiconductor Quantum Dots. *J. Chem. Phys.* **1999**, *111*, 6955−6964.

https://dx.doi.org/10.1021/acs.chemrev.0c00831
Chem. Rev. 2021, 121, 3186−3233